Lecture Notes on The Planetary Boundary Layer

Chin-Hoh Moeng

NCAR TECHNICAL NOTES
http://library.ucar.edu/research/publish-technote

The Technical Notes series provides an outlet for a variety of NCAR Manuscripts that contribute in specialized ways to the body of scientific knowledge but that are not yet at a point of a formal journal, monograph or book publication. Reports in this series are issued by the NCAR scientific divisions, serviced by OpenSky and operated through the NCAR Library. Designation symbols for the series include:

EDD – Engineering, Design, or Development Reports
Equipment descriptions, test results, instrumentation, and operating and maintenance manuals.

IA – Instructional Aids
Instruction manuals, bibliographies, film supplements, and other research or instructional aids.

PPR – Program Progress Reports
Field program reports, interim and working reports, survey reports, and plans for experiments.

PROC – Proceedings
Documentation or symposia, colloquia, conferences, workshops, and lectures. (Distribution maybe limited to attendees).

STR – Scientific and Technical Reports
Data compilations, theoretical and numerical investigations, and experimental results.

Lecture Notes On The Planetary Boundary Layer

Chin-Hoh Moeng
Mesoscale & Microscale Meteorology Lab, National Center for
Atmospheric Research, Boulder, CO

This set of lecture notes introduces the dynamics, statistics, clouds, and models of the planetary boundary layer (PBL). The author prepared the notes for graduate classes while on sabbatical leave at the Department of Atmospheric Science at Colorado State University in 1994 and 1998 and the Department of Atmospheric and Oceanic Sciences, University of California, Los Angeles, in 2006. The notes evolved over those years. These lecture notes cover the basic concepts of PBL turbulence and describe different PBL types including clear convective, neutral and stable regimes, as well as boundary-layer clouds. The last chapter introduces various PBL parameterization schemes developed for weather and climate models.

LECTURE NOTES ON THE Planetary Boundary Layer

Chin-Hoh Moeng

prepared for lectures given at the Department of Atmospheric Science, CSU in 1994 & 1998
and at the Department of Atmospheric and Oceanic Sciences, UCLA in 2006

1. INTRODUCTION

1.1 The nature of turbulence (see Appendix)

1.2 Averaging: statistics vs. instantaneous flow field

1.3 Governing equations

      1.3.1 Navier-Stokes equation

      1.3.2 Reynolds equation (or ensemble-mean equation)

1.4 Commonly-used terminology

      1.4.1 Energy-containing eddies and Kolmogorov microscale

      1.4.2 Reynolds number and Reynolds-number-independent regime

      1.4.3 Homogeneous and isotropic turbulence

      1.4.4 Quasi-steady state; large-eddy turnover time

      1.4.5 Inertial subrange and Kolmogorov theory

1.5 Research tools: field measurements, lab, LES, PBL modeling

      1.5.1 Understanding turbulent motions

      1.5.2 Modeling ensemble-mean statistics

2. THE SURFACE LAYER

2.1 Eddy structures

2.2 Monin-Obukhov similarity theory

1 INTRODUCTION

1.1 The nature of turbulence

No one describes the nature of turbulence better than Tennekes and Lumley. In their classic book (A First Course in Turbulence, 1972), Tennekes and J. L. Lumley list seven important characteristics of turbulent flows: *irregularity, diffusivity, large Reynolds number, three-dimensional vorticity fluctuations, dissipation, continuum, and turbulent flows are flows.* An excerpt that describes these characteristics from their pages 1-4 is given in the Appendix for your reference.

1.2 Averaging: statistics vs. instantaneous flow field

Because the details of the randomly-distributed turbulent field don't mean much, turbulence is often described by its averaged properties. Averaged properties are called statistics, including mean (expected) values (1st moments), fluxes and variances (2nd moments), skewness (3rd moment), probability density distribution, power spectrum, etc. To derive these statistics, we decompose a turbulent quantity to mean and fluctuating parts as $u = \bar{u} + u'$ where $\bar{u}$ is defined by an averaging procedure (filtering procedure). Statistics, such as variance, are then computed as $\overline{u'u'}$. Every time you look at a statistical measure, it is useful to know the type of averaging behind the measure.

The most traditional description of turbulence uses "ensemble averaging"—over a large samples of flow realizations—such that *all* random turbulent motions can be removed by the average. Ensemble mean represents the expected outcome (or value) of the event. However, true ensemble average of geophysical turbulence is difficult to obtain because a turbulent event never repeats itself. In practice, we approximate ensemble averaging with spatial averaging (of, e.g., aircraft measurements) or time averaging (of, e.g., tower data). A time averaging of the turbulent plume of a smokestack downstream of a point source in a wind tunnel can be viewed from a long-time exposure camera, shown in Fig. 1.1. The top figure is the random instantaneous flow field of the event and the bottom is an time-averaged (or filtered) field.

TIME/SPACE FILTERING

Smoke visualization downstream of a point source in a wind tunnel

Instantaneous plume
(short time exposure)

a)

b)

Ensemble average plume
(long time exposure)

2-18
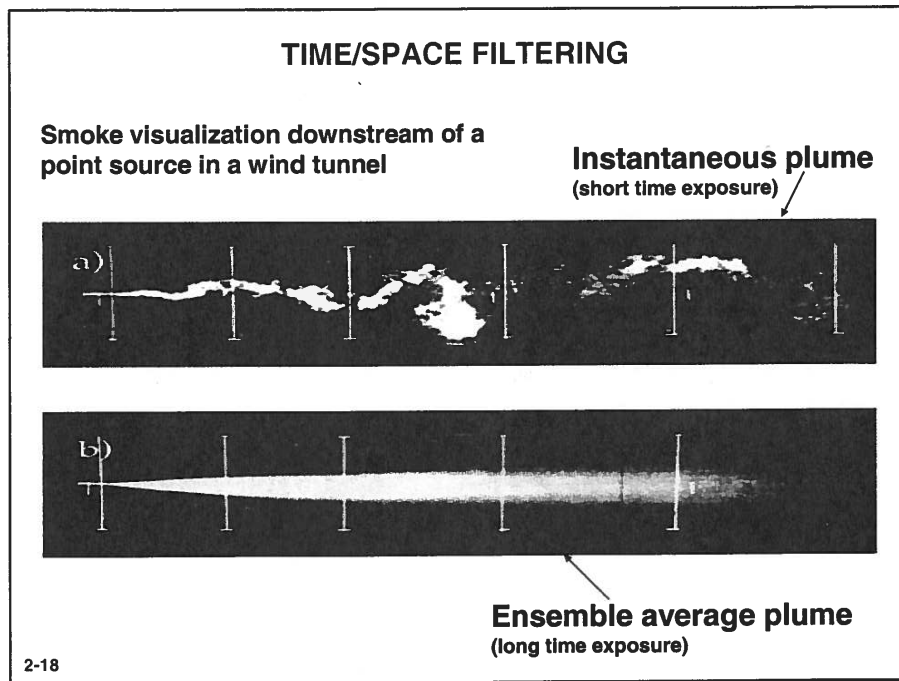
Figure 1.1 (SOURCE: EPA Fluid Modeling Facility)

If a turbulent flow field is horizontally homogeneous and quasi-steady, as we often assume for the PBL over uniform surface, then a horizontal averaging over a long distance or a large horizontal domain may represent an ensemble average. How time and spatial averages converge to ensemble average is a sampling problem. The flight length of an aircraft dataset or the time record of tower data has to be long enough so the statistics using a line (or time) averaging can approach ensemble-mean statistics. But the sample length cannot be too long to violate the horizontally homogeneous (or quasi-steady) assumption. As discussed in *"Lectures on the Planetary Boundary Layer"* by John Wyngaard in the book *Mesoscale Meteorology–Theories, Observations and Models*, edited by Lilly and Gal-Chen, NATO ASI Series, the averaging time period (or length) is proportional to the integral scale and the intensity of the turbulent flow field.

1.3 Governing equations

The before and after averaging of a turbulent flow field mentioned above can be described by its corresponding governing equations: Navier-Stokes equation and the Reynolds equation, as described below.

1.3.1 Navier-Stokes equation—governing the whole turbulent motion

The Navier-Stokes equation is the most fundamental dynamical equation of a viscous incompressible fluid. The flow field of a fluid at any time, t, and space, x_i, is governed by

$$\frac{\partial u_i}{\partial t} + u_j \frac{\partial u_i}{\partial x_j} = X_i - \frac{1}{\rho}\frac{\partial p}{\partial x_i} + \nu \frac{\partial^2 u_i}{\partial x_j^2}, \tag{1}$$

where X_i is the i-component of external forces, p pressure fluctuations, and ν the kinematic viscosity of the fluid. Along with the continuity eq.,

$$\frac{\partial u_i}{\partial x_i} = 0, \tag{2}$$

the set of equation is complete; there are four equations for four unknowns u, v, w and p. Notice the molecular term appears in the Navier-Stokes equation and the solution $u_i(x, y, z, t)$ includes all scales of motions, down to dissipation scales.

When the non-linear interaction term (i.e., $u_j \partial u_i / \partial x_j$) is much larger than the molecular viscous term (i.e., $\nu \frac{\partial^2 u_i}{\partial x_j^2}$), the solution of (1) is a fully developed turbulent motion. The ratio of these two terms is called Reynolds number, which will be described in next section. The non-linear term includes vortex stretching and scrambling and energy cascading in 3D turbulence.

1.3.2 Reynolds equation (or ensemble-mean equation)

Reynolds equation is the ensemble average of the Navier-Stokes equation. Reynolds equation is what we solve in GCMs or mesoscale models, not the Navier-Stokes equation. The solution of Reynolds equation does not explicitly contain turbulent motions because the chaotic turbulent component of the flow is filtered out, as you can see from the following derivation of the Reynolds equation.

To derive the Reynolds equation, we decompose a variable, s, into a Reynolds (or ensemble) mean component (denoted by overbar), $\bar{s}$, and its fluctuation (or random turbulent) component (by prime), s', i.e.,

$$s = \bar{s} + s'. \tag{3}$$

The Reynolds averaging obeys the following rules:

$$\overline{s'} = 0, \qquad \overline{ws} = \bar{w}\,\bar{s} + \overline{w's'}, \qquad \overline{w+s} = \bar{w} + \bar{s}, \qquad \overline{as} = a\bar{s}, \tag{4}$$

where a is a constant, and w is another variable. With this averaging, the cross terms $\overline{\bar{w}s'}$ and $\overline{w'\bar{s}}$ are exactly zero. These rules imply that there is a spectral gap between the mean motion and the filtered out turbulent motions.

By expanding Eq. (1) over a reference atmosphere state (denoted by the subscript 0) and decomposing it into the Reynolds mean and fluctuations, we have

$$\left(\frac{\partial \overline{u_i}}{\partial t}+\frac{\partial u_i'}{\partial t}\right)+\left(\overline{u_j}\frac{\partial \overline{u_i}}{\partial x_j}+\overline{u_j}\frac{\partial u_i'}{\partial x_j}+u_j'\frac{\partial \overline{u_i}}{\partial x_j}+u_j'\frac{\partial u_i'}{\partial x_j}\right) = \frac{g_i}{T_0}(\bar{\theta}+\theta')-\frac{1}{\rho_0}\frac{\partial \overline{p}}{\partial x_i}-\frac{1}{\rho_0}\frac{\partial p'}{\partial x_i}+\nu\frac{\partial^2 \overline{u_i}}{\partial x_j^2}+\nu\frac{\partial^2 u_i'}{\partial x_j^2}. \tag{5}$$

The only external force we consider here is the buoyancy force, i.e., $X_i = g_i/T_0\theta$. Using the averaging rules (4) in (5) yields

$$\frac{\partial \overline{u_i}}{\partial t} + \overline{u_j}\frac{\partial \overline{u_i}}{\partial x_j} = +\frac{g_i}{T_0}\bar{\theta} - \frac{1}{\rho_0}\frac{\partial \overline{p}}{\partial x_i} - \frac{\partial \overline{u_i'u_j'}}{\partial x_j} + \nu\frac{\partial^2 \overline{u_i}}{\partial x_j^2}, \tag{6}$$

where the $\overline{u_i'u_j'}$ term is the so-called "Reynolds stress" term. For geophysical flows, the molecular term in (6) is several orders of magnitude smaller than the Reynolds stress term and can be neglected. Geophysical turbulence is often referred to as high Reynolds number flow. Thus, the Reynolds equation we solve in GCM or mesoscale models is

$$\frac{\partial \overline{u_i}}{\partial t} + \overline{u_j}\frac{\partial \overline{u_i}}{\partial x_j} = +\frac{g_i}{T_0}\bar{\theta} - \frac{1}{\rho_0}\frac{\partial \overline{p}}{\partial x_i} - \frac{\partial \overline{u_i'u_j'}}{\partial x_j}, \tag{7}$$

where the Reynolds stress term represents the net effect of all filtered-out turbulent motions; none of the turbulent motion is explicitly included in the resolved field $\overline{u_i}$. The solution of (7) (i.e., $\overline{u_i}$) is the ensemble mean of that of (1) (i.e., u_i).

To solve (7) the Reynolds stress term needs to be parameterized, i.e., the stress term needs to be expressed in terms of the solvable variables. This is a closure problem, to close

the system of the governing equation. The simplest way to handle the closure problem is to assume that turbulent motions behave like molecular motions. This yields the constant eddy viscosity assumption where the stress term

$$-\frac{\partial \overline{u_i' u_j'}}{\partial x_j} = K \frac{\partial^2 \overline{u_i}}{\partial x_j^2}, \tag{8}$$

and then (7) would look just like (1, with $X = \frac{g_i}{T_0}\theta$) except that turbulent eddy viscosity K now replaces the molecular viscosity ν. But of course turbulence does not behave like molecular motions and that's why constant eddy viscosity cannot work.

Some turbulence models close the (7) system by carrying yet more prognostic equations for the Reynolds stress, an approach referred to as higher-order closure modeling approach. We will learn about various types of PBL models in Section 6. For now, it is useful to know how the governing equations (or budgets) of higher-moment statistics (such as Reynolds stress or turbulent kinetic energy) look like. Equations for higher-moment statistics can be formally derived based on the eqs. of velocity (and of course temperature and moisture) fluctuations [see ref.: C. du. P. Donaldson, 1973: *Construction of a Dynamic Model of the Production of Atmospheric Turbulence and the Dispersal of Atmospheric Pollutions, Workshop on Micrometeorology, published by the AMS*], which are obtained by subtracting the mean, (6), from the total, (5),

$$\frac{\partial u_i'}{\partial t} + \overline{u_j}\frac{\partial u_i'}{\partial x_j} + u_j'\frac{\partial \overline{u_i}}{\partial x_j} + u_j'\frac{\partial u_i'}{\partial x_j} - \overline{u_j'\frac{\partial u_i'}{\partial x_j}} = +\frac{g_i}{T_0}\theta' - \frac{1}{\rho_0}\frac{\partial p'}{\partial x_i} + \nu\frac{\partial^2 u_i'}{\partial x_j^2}. \tag{9}$$

For example, the equations for the Reynolds stress $\overline{u_i' u_j'}$ can be obtained by (a) multiplying (9) by u_j', (b) multiplying (9) for u_j' by u_i', (c) summing them up, and (d) applying Reynolds averaging. This yields a set of equations for $\overline{u_i' u_j'}$.

The ensemble-mean and fluctuating equations for scalars can be derived the same way.

In deriving these equations, we further assume horizontal homogeneity, i.e., $\partial\overline{\Phi}/\partial x = \partial\overline{\Phi}/\partial y = 0$, where $\overline{\Phi}$ is a statistical quantity. This assumption is referred to as the "PBL assumption". Under this assumption, none of the horizontal fluxes shows up in the moment equations; there are only vertical derivatives of the vertical turbulent fluxes. But be cautious: This doesn't mean that the horizontal turbulence fluxes are zero; the horizontal fluxes can be as large as the vertical fluxes in the PBL. Because of the horizontal homogeneous assumption

(more in next section), horizontal convergence/divergence of the horizontal fluxes is assumed to be zero.

Homework 1:

A. Normalize the Navier-Stokes equation (assuming no external forcing) using a velocity scale U and a length scale L and show that the dimensionless equation contains only one dimensionless parameter. What is it?

B. Derive the Poisson's equation for pressure from (1) and (2) and describe each term based on where it comes from.

C. Derive the Reynolds-averaged turbulent-kinetic-energy (TKE) equation from (9), using the PBL assumption, and the describe the physics of each terms.

1.4   Commonly-used terminology

1.4.1   Energy-containing eddies and Kolmogorov microscale

The largest eddies in a turbulent flow are generated directly from shear or buoyancy instability of the mean field. They contain most of the turbulent kinetic energy and thus are called *"energy-containing eddies"*. Their turbulence dynamics depend on their environmental conditions such as flow geometry and driving force and their sizes are limited by flow geometry or other environmental conditions. In a convective daytime PBL, for example, the capping inversion limits the largest turbulent eddies to be on the order of 1 kilometer.

The smallest eddies in turbulence are called *"Kolmogorov microscale"* η, which are the largest viscous eddies responsible for dissipating energy. Their characteristics thus depend on the dissipation rate ϵ (which has a dimension of L^2/T^3) and the viscosity of that particular fluid ν (which has a dimension of L^2/T). From dimensional arguments this means their length scale is on the order of $(\nu^3/\epsilon)^{1/4}$. Since the amount of turbulent energy that dissipates in small scales must equal the amount of energy inputs from energy-containing scales, the dissipation rate can be expressed in terms of the characteristics of energy-containing eddies, i.e., $\epsilon \sim U^3/L$, where U and L are velocity and length scales of energy-containing eddies. In

convective PBL, $U \sim w_* \sim 1$ m/s and $L \sim z_i \sim 10^3$m, thus $\epsilon \sim 10^{-3}$ m^2/s^3. For air, $\nu = 1.5 \times 10^{-5}$ m^2/s, thus the smallest turbulent eddies are on the order of $\eta \sim 10^{-3}$m.

In between the energy-containing eddies and dissipative eddies, there is an inertial sub-range, which will be described in section 1.4.5.

1.4.2   Reynolds number and Reynolds-number-independent regime

Reynolds number R_e is defined as the ratio of the inertia force [i.e., nonlinear scrambling, the second term on the left-hand side of (1), which is on the order of $\sim U^2/L$] to the viscous force [i.e., the third term on the right-hand side of (1), which is on the order of $\sim \nu U/L^2$]. Here again U and L are velocity and length scales of energy-containing eddies. Thus, $R_e = UL/\nu$. When the nonlinear scrambling effect dominates the viscous effect, i.e., the Reynolds number is large enough, the flow becomes turbulent. The critical R_e for transition to turbulence in a pipe flow is about 2000. For a convection water tank, the critical R_e is about 100.

Higher R_e implies a broader scale range of turbulent eddies. The convection turbulence in the Deardorff-Willis water tank [Deardorff and Willis, 1985; Bound-Layer Meteorol., 32, 205–236] has $L \sim z_i \sim 20$ cm, $U \sim w_* \equiv [\frac{g}{T_0}\overline{wT_0}z_i]^{1/3} \sim 0.8$ cm/s, and $\nu_{\text{water}} \sim 1.5 \times 10^{-6}$ m^2/s, thus it has $R_e \sim 10^3$, so turbulent eddies range from millimeters (Kolmogorov scale) to few tens centimeters (the size of the tank). In a typical convective PBL, $U \sim w_* \sim 1$ m/s, $L \sim 1$ km, and $\nu_{\text{air}} \sim 1.5 \times 10^{-5}$ m^2/s, thus $R_e \sim 10^8$ (w_* and z_i defined later), so eddies range from millimeters (again the Kolmogorov scale) to a few kilometers (the height of the capping inversion). With such a high R_e, PBL turbulence is considered *"fully developed turbulence"*, way beyond the transition-to-turbulence regime. Turbulence in the PBL is usually well maintained by vertical wind shear at night and buoyancy in the day time, except in windless nights.

If two different fluids with the same geometry have the same Reynolds number, i.e., $U_a L_a/\nu_a = U_b L_b/\nu_b$, their turbulent motions are "dynamically similar". It is easier to understand this similarity property from the Navier-Stokes equations. Normalizing (1) using a velocity scale U, a length scale L, a time scale L/U, and a pressure scale $\rho_0 U^2$ (for incompressible flows) leads to the dimensionless Navier-Stokes equations that contain only one parameter, $R_e = UL/\nu$. Thus, for a given geometry of the flow and initial condition, the solutions of (1) depend only on R_e.

Most statistical properties of turbulence and large-eddy structure become independent of the Reynolds number when R_e is sufficiently large. This is called the *"Reynolds-number-independent regime"*. Deardorff-Willis' water-tank turbulence is probably well within this range, so turbulence properties we learn from their tank experiments can apply to the clear convective PBL even though the latter has a much larger R_e. However, fine-scale structure may be quite different in two Reynolds-number-similar flow fields even though their large eddy structure is similar. Thus we should be cautious when applying laboratory results to PBL phenomena that depend strongly on fine-scale structure.

1.4.3 Homogeneous and isotropic turbulence

"Homogeneous turbulence" doesn't mean the spatial structure of the flow is uniform in the horizontal plane; it means its statistical properties are independent of position. Likewise, *"isotropic turbulence"* means its statistical properties do not change by a coordinate rotation or translation. Thus, in homogeneous turbulence, spatial derivatives of all turbulent statistics are zero, and in isotropic turbulence, $\overline{u^2} = \overline{v^2} = \overline{w^2}$ and all fluxes are zero since it does not have any prefer direction.

PBL turbulence is often treated as horizontally homogeneous because the scale of horizontal variations of large-scale environments is typically much larger than the PBL scale, i.e., $\gg$1 km. Thus, the horizontal derivatives of PBL turbulent statistics are assumed to be zero (i.e., the 'PBL assumption' mentioned in section 1.3.2). However, PBL turbulence cannot be isotropic; otherwise, all of the fluxes of momentum, heat and other scalars would vanish. Those turbulent fluxes are crucial to weather and climate.

Nevertheless, smaller eddies within the inertial subrange (see section 1.4.5) may be close to homogeneity and isotropy because they are generated through energy cascade (i.e., non-linear scrambling) from larger eddies and are not significantly influenced by anisotropy and inhomogeneity of the mean field or flow geometry. These small eddies are assumed to be *"locally homogeneous and isotropic"*. This assumption is used to derive the well-known Kolmogorov theory (1.4.5). But in the PBL even small eddies within the inertial subrange carry some amount of fluxes, albeit small.

1.4.4 Quasi-steady state and large-eddy turnover time

PBL turbulence is often in a state of local equilibrium with its large-scale environment—
"quasi-steady state", because synoptic or mesoscale motions often vary much slower than the
turbulent large-eddy turnover time. *Large-eddy turnover time* is defined as the ratio of the
length to velocity scales of energy-containing eddies, $\tau = L/U$, which is few tens minutes
in a typical convective PBL (CBL). In quasi-steady state, the statistical properties (such as
fluxes and variances) remain unchanged—if they are properly scaled (I will explain scaling
laws later). A quasi-steady state is not an exactly steady state; the mean wind can vary due
to Coriolis inertial oscillation and the mean temperature can change due to surface heating
or cooling. A quasi-steady state implies that the vertical shapes of the mean fields remain
unchanged.

The PBL can quickly adjust to its slowly changing environments (such as diurnal vari-
ations) to reach individual quasi-steady states. This property provides the basis for pa-
rameterizing the PBL turbulence in large-scale meteorological models. In parameterizations
the net turbulent effect is assumed to be functions of a given mean state. We cannot pa-
rameterize the PBL statistics if they keep changing in a given mean state. Also, because
of the existence of quasi-steady states, we can categorize PBLs into different regimes (i.e.,
different quasi-steady states) and study them separately. For example, the clear convective
PBL regime is a quasi-steady regime that is driven by surface heating, while the stable PBL
is another regime that is driven by vertical wind shear in a stably stratified environment.
In this course, we will first study the clear convective PBL regime, i.e., daytime PBL over
heated surface. It is the simplest and most understood regime. In section 4, we will study
the stable PBL (nighttime PBL over land) in which shear and buoyancy act against each
other. In section 5, we will study more complicated PBL regimes that involve clouds: PBLs
with stratocumulus and shallow cumulus.

1.4.5 Inertial subrange and Kolmogorov theory

In a sufficiently high R_e turbulent flow, there exists a wide range of energy spectrum that
has a –5/3 spectral slope (Fig. 1.2); they lie in between energy-containing eddies and viscous
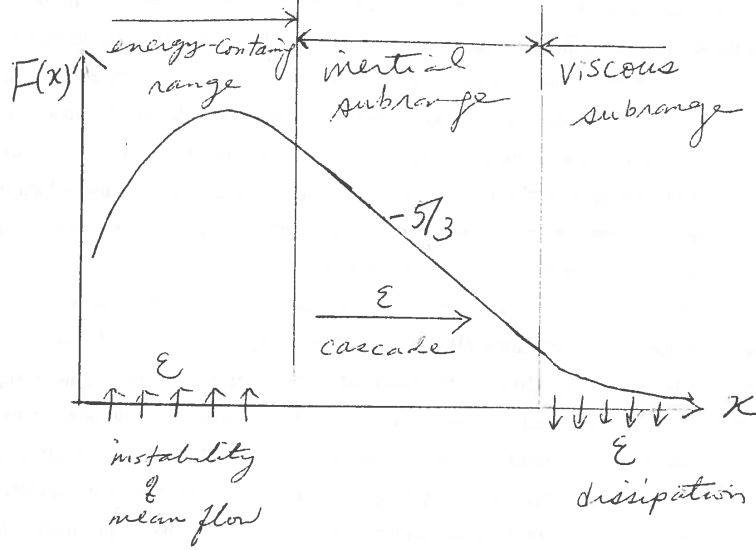eddies. This intermediate range is called the *"inertial subrange"*.

Figure 1.2

Eddies in this subrange are generated from nonlinear interactions of energy-containing eddies. They are smaller than the energy-containing eddies, but much larger than the viscous eddies. Eddies in this subrange are not generated from the mean field and also they are not dissipative. They merely pass along the energy from energy-containing scale to viscous scale at an equilibrium rate ϵ. *Kolmogorov theory* was derived in 1941 based on the following dimensional argument: Assuming that the characteristics of inertial-subrange turbulence depend only on one dimensional parameter, the energy dissipation rate ϵ, which has a dimension of L^2/T^3, where $T \sim L/U$ is the time scale. The energy spectrum $F(\kappa)$ has a dimension of $dE/d\kappa \sim [L^2/T^2]/L^{-1} = L^3/T^2$, where κ is the wave number. If the energy spectrum depends only on ϵ, it can be written as $F(\kappa) \propto \epsilon^m \kappa^n$. From dimensional arguments, we have $m = 2/3$ and $n = -5/3$, i.e., $F(\kappa) = \alpha \epsilon^{2/3} \kappa^{-5/3}$, where α is the proportionality constant. This is the well-known *"Kolmogorov theory"* and α is the *"Kolmogorov constant"*.

1.5   Research tools

1.5.1   Understanding turbulent motions

Data from field measurements (e.g., aircrafts or radars) and laboratory experiments (e.g., tank experiments), as well as numerical simulation solutions (e.g., DNS and LES), consist of detailed turbulent motions, not just the ensemble-averaged quantities. They can be used as

database to gain better understanding of the PBL turbulent motions—their flow structure and evolution.

The advantages of field measurements are that the data are "real", and some of them (like aircraft) can measure very fine-scale turbulent motion. However, field data are often contaminated with mesoscale variations, which are hard to analyze for studies of just turbulence. Also, in-situ aircraft measurements provide data only in one direction along the flight path, so these data are difficult to use to construct multi-dimensional views of turbulent coherent structure. (Sometimes we want to know how turbulence transports heat or moisture by looking at its coherent structure. Also, to better understand entrainment mechanisms, it would be helpful to be able to visualize how large eddies impinge onto the capping inversion and 'bring' inversion air into the PBL.) Doppler radar or lidar may provide a better alternative in observing flow structure. Some important turbulent quantities, such as pressure fluctuations, are also difficult to measure in the field.

Laboratory experiments also provide "real" turbulent flow fields, but those flows are low R_e. Many existing laboratory flows (Wyngaard called them "tea cup" turbulence) may not have a R_e that is large enough to be in the Reynolds-number-independent regime to represent PBL turbulence. Pressure fluctuations are also difficult to measure in the laboratory.

With the increasing computer power, numerical simulations are becoming a popular research tool for studying turbulence and generating database. Since the fundamental equations that govern turbulent motions are known (i.e., the Navier-Stokes equations), their numerical representation could in principle provide us with a full turbulence solution. Today's computers are able to perform up to $\sim (1000)^3$ grid-point simulations. Thus, a medium R_e turbulent flow, which has eddies ranging from millimeters (Kolmogorov scale) to few centimeters (e.g., Deardorff-Willis tank turbulence), can be "exactly" simulated; this exact simulation of full range of turbulence is called "*direct numerical simulation* (DNS)".

For high R_e, such as PBL turbulence which covers eddies from millimeters to kilometers, we need $\sim 10^{18}$ grid points to resolve all eddies. This is clearly impossible. But the following properties of the PBL turbulence make it possible for an alternative approach called "Large Eddy Simulation (LES)". First, the energy-containing eddies are the ones that carry most of the turbulent fluxes (and variances), which are the most important PBL parameters for meteorological applications. Second, we know the properties of the inertial-subrange eddies

14

from Kolmogorov's theory. So, if we have a three-dimensional computer code that has a grid size much smaller than the energy-containing eddies (i.e., within the inertial subrange), we can numerically integrate the governing equations to solve for the spatial and time evolution of energy-containing eddies while the net effect of small subgrid eddies can be quite reasonably parameterized based on Kolmogorov theory (ref. Moeng and Wyngaard 1988, JAS, 23, 3573–3587). Such simulation solutions could in principle be used as a surrogate for the PBL turbulence. The LES approach was first proposed by Deardorff in the early 1970s, and is now widely used in the PBL community (summarized in Moeng and Sullivan, 2015, Large-Eddy Simulation. Editors: G.R. North, J.Pyle and F. Zhang. Encyclopedia of Atmospheric Sciences, 2nd edition, ISBN: 9780123822253). But numerical solutions are not real flows. Some of the simulated flow properties may depend significantly on numerics or subgrid-scale models. Therefore, LES should be used with great caution. It should be used only to study phenomena or statistics that depend mainly on the energy-containing (i.e., well resolved) eddies.

1.5.2 Modeling ensemble-mean statistics

In meteorological forecast models, the grid mesh is typically much larger than the energy-containing eddies of the PBL. Therefore, it is necessary to model (i.e., parameterize) the net effect of *all* turbulent motions within the PBL. This type of models is called PBL modeling in which the ensemble-averaged statistics are parameterized as functions of the mean field. In conventional PBL models, all turbulent eddies are parameterized; none explicitly resolved.

Over the years many different types of ensemble-mean turbulence models were developed specifically for PBL applications. We will learn these models in Section 6—after we have learned some important aspects of the PBL turbulence and its structure. This way we would learn better how each PBL model was built and know how to interpret results from each PBL model. As you will learn, all PBL models require first setting up a framework (or a theory) to express turbulent fluxes in terms of mean fields, and then provide some sort of closure assumptions to complete the set of equations (i.e., closure problems). How to make proper closure assumptions is the most essential issue for PBL modeling. Many of the existing closure assumptions were made based on laboratory data, field data, or large eddy simulation results.

2 THE SURFACE LAYER

Figure 2.1 is a sketch showing the diurnal cycle of the PBL over land under clear skies. The lowest layer that are strongly affected by surface properties is the surface layer. The depth of the surface layer in a typical convective PBL is about 10% of the depth of the whole PBL, and hence about 100 m for a daytime PBL of about 1 km deep. The surface layer is sometimes called "inertial sublayer" because it lies between the viscous layer (which is a few millimeters above the surface) and the energy-containing layer (i.e., the mixed layer).
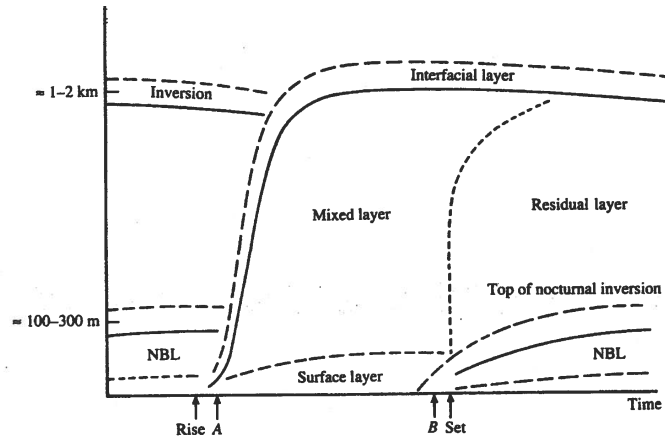

Figure 2.1 (SOURCE: Stull's 1998 textbook)

The surface layer is usually referred to as the *constant flux layer*. However, you should know that fluxes within the surface layer are not more "constant" than those above this layer. The reason we call it the "constant flux" layer is described below: Within the boundary layer, there is an approximate balance among the three major forces in the horizontal components of the Reynolds equations: the pressure gradient force, the Coriolis force, and the Reynolds stress term (i.e., friction force). This so-called *Ekman balance* is written as:

$$f\vec{k} \times (\vec{V}_H - \vec{V}_g) = \frac{1}{\rho_0} \frac{\partial \vec{\tau}_H}{\partial z}, \tag{10}$$

where f is the Coriolis parameter, $\vec{V}_H$ the vector of horizontal wind speed, $\vec{V}_g$ the vector of geostrophic wind, and $\vec{\tau}_H \equiv < \overline{u'w'}, \overline{v'w'} >$ is the vector of Reynolds stresses. Here we assume that $\partial/\partial x = \partial/\partial y = 0$ for horizontally homogeneous PBL. Vertically integrating (10) over a thin layer from the surface to the top of the surface layer, δz, we get

$$\rho_0 f \vec{k} \times (\vec{V}_H - \vec{V}_g)\delta z = \vec{\tau}_H(\delta z) - \vec{\tau}_H(0). \qquad (11)$$

If the surface layer is thin, $\delta z \to 0$, $\vec{\tau}_H(\delta z) \sim \vec{\tau}_H(0)$, so the stress can be considered approximately 'constant' across this thin layer. But remember that $\partial \vec{\tau}_H/\partial z$ within the surface layer is usually as large as that above the surface layer.

2.1 Eddy structures

Before we get into the statistical description of the surface layer, let's see what eddies look like within the surface layer.

Data from in-situ measurements are typically one dimensional in space or time, and therefore are difficult to extrapolate to a planform pattern. Wilczak and Tillman (1980, JAS, 37, 2424–2443) set up an array of 16 temperature sensors, covering a 100 m x 40 m area at a height of 4 m, next to the BAO (Boulder Atmospheric Observatory) tower, and was able to provide us with a "look" of observed three-dimensional structure of eddies within the surface layer. In a near-neutral surface layer, they observed plume structures that are mostly elongated along the mean wind direction (Fig. 2.2a); typical dimensions are several hundreds of meters along the wind and several tens of meters across the wind. In a strongly convective surface layer, they found that the plumes tend to elongate in the crosswind direction (Fig. 2.2b), with a typical alongwind length of about 10 to 75 m. Wilczak (1984, JAS, 41, 3537–3550) also constructed ensemble vertical cross sections of velocity and temperature fields associated with large eddies (Fig. 2.2c) in the convective surface layer.

In purely buoyancy-driven turbulence (i.e., free convection), convection tank experiments (e.g., Willis and Deardorff 1979, JGR, 84, 295–302) showed that near the wall, convergence takes place "along irregular lines which intersect in a pattern suggestive of cellular structures having ascending motions at their peripheries and descending motions in their interior." These irregular cellular patterns are also observed from fine-resolution LES (e.g., Schmidt and Schumann 1989, JFM, 200, 511–562) as shown in Fig. 2.3. The horizontal dimension of this near-wall pattern is about the depth of the whole PBL. Vigorous updrafts that extend all the way up to the mixed-layer top are found to originate at the intersections of the near-surface convergence lines. Those features are consistent with the parallel-plate

17

(a)

2 -2.5°C

1.5 - 2°C

1 - 1.5
5 - 1
0 - .5

(b)

2-2.5

1.5-2

1-1.5

5-1

0-.5°C

2 - 2.5°C

(c)

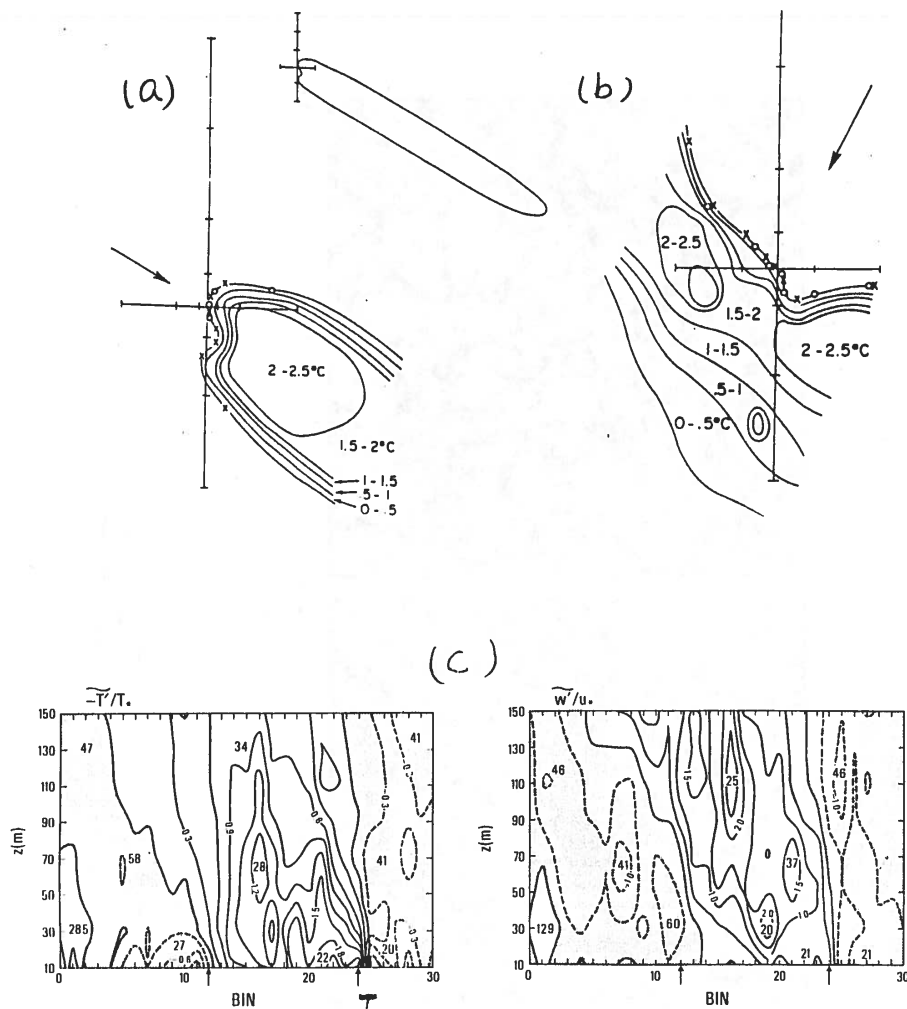$\widetilde{-T'}/T_*$

$\widetilde{w'}/u_*$

FIG. 2a. Vertical cross section of the ensemble LSE temperature field. Regions of cold temperature deviations are shaded. Contour intervals correspond to $0.3T_*$, or $\approx 0.1°C$. Weighted standard deviations of the mean, expressed as a percentage of the mean value, are given at selected locations.

FIG. 2b. As in Fig. 2a but for the vertical velocity field. Downdraft regions are shaded. Contour intervals correspond to $0.5u_*$, or ≈ 0.3 m s^{-1}.

Figure 2.2 (SOURCES: Wilczak and Tillman, 1980; Wilczak 1984)

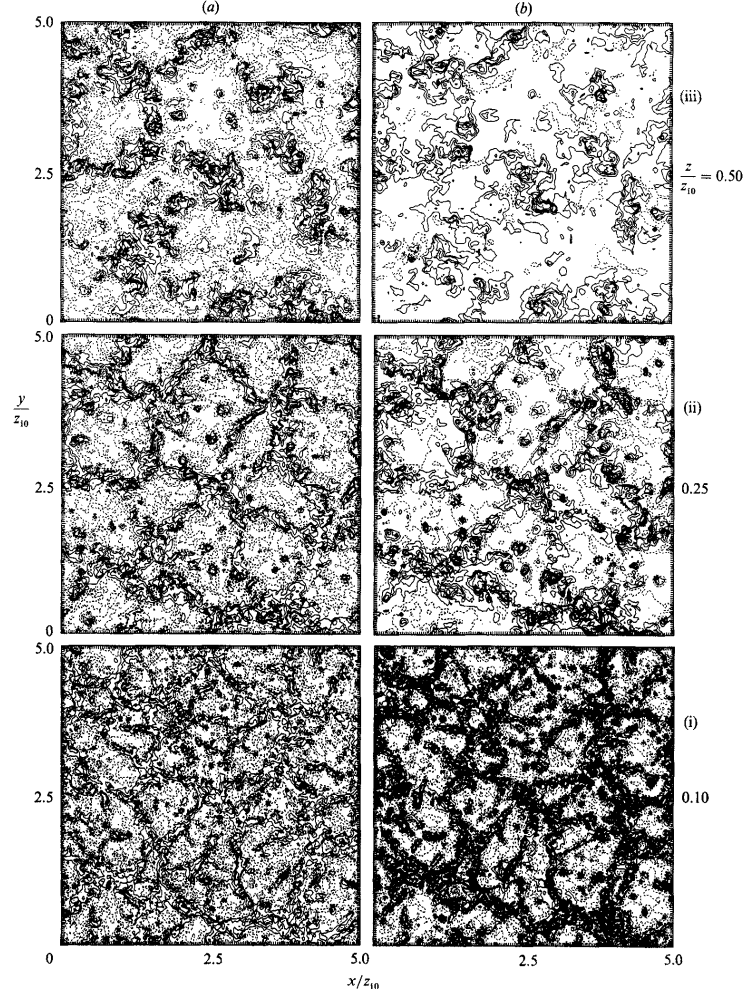Rayleigh-Bernard convection in a lower R_e number regime.

Figure 2.3 (SOURCE: Schmidt and Schumann 1989)

The above described large-eddy features are often called *coherent structure*; they are long lasting (on the order of a large-eddy-turnover time, i.e., few minutes) compared to the small random eddies. These coherent eddies are responsible for most of the turbulent transport of momentum, heat and other scalars (e.g., Wilczak 1984, JAS, 41, 3537–3550; Mahrt and Gibson 1992, JAS, 60, 143–168). It is easy to see from Fig. 2.2c and Fig. 2.3, where most updraft eddies ($w'' > 0$) are well correlated with warmer parcels (i.e., thermals, which have $\theta'' > 0$). This positive correlation results in net upward transport of heat (through convective turbulence) in the convective PBL.

There are ongoing research trying to characterize these coherent structures, to determine

how much of the total fluxes is carried by these structures, and to find relationships between structure and flux. In some complicated PBL regimes (e.g., over complex terrain) where ensemble statistics are difficult to define, one may need to rely on the characteristics of their coherent structure to determine their turbulent statistics.

2.2 Monin-Obukhov similarity theory

The most commonly-used statistical method in describing the surface-layer turbulence is Monin-Obukhov *similarity theory.* It is an extension of the well known logarithmic 'law of the wall' in engineering term, to include the temperature stratification effect.

Let me first describe *similarity theory* (or *similarity hypothesis*) using a pure shear-driven turbulent surface layer as an example. Within a neutrally stratified surface layer, no buoyancy force is involved. And since the molecular viscosity is negligible, the only relevant velocity parameter is the surface friction velocity $u_* = (\overline{u'w'}_0^2 + \overline{v'w'}_0^2)^{1/4}$, which can be considered "constant" within the "thin" surface layer. The only length scale is z, the distance from the wall. Thus, it is hypothesized that the vertical shear of the mean wind $\partial U / \partial z$ depends only on u_* and z. The only combination of these two parameters that gives the dimension of wind shear is u_*/z. Therefore,

$$\frac{\partial U}{\partial z} = \frac{1}{\kappa} \frac{u_*}{z},\tag{12}$$

where κ is the proportionality constant, which is called *von Karman constant* because von Karman derived (12) in 1930. This constant is not given by theory, but can be measured in laboratories or the field. Laboratory results gave $\kappa \sim 0.4$. Field measurements showed a great scatter (Table 2.1, taken from Cai's Ph.D. thesis, 1993). In general, this value falls in the range of 0.35 to 0.43.

So, similarity theory is to use *dimensional analysis* to incorporate all relevant *governing parameters* (such as velocity, length, or time scales) into a formula (or a theory). The most difficult task in developing a similarity theory is to come up with all of the relevant governing parameters. After dimensional rearrangement, one then needs to empirically determine the proportionality constants (or universal functions) involved.

Vertically integrating (12)—from the height where the extrapolated mean wind becomes

Table 2.1: Estimates of the von Kármán constant κ from measurements

Author(s)	κ	Comment
Goddard (1970)	0.41	
Dyer & Hicks (1970)	0.41	Also see Dyer (1974)
Hicks (1970)	0.42($\pm$0.02)	No detail provided
Businger et al. (1971)	0.35	See, e.g., Wieringa (1980)
Pruitt et al. (1973)	0.42	0.39 by Kondo & Sato (1982)
Frenzen(1973)	0.35($\pm$0.01)	$\alpha_u = 0.55$ was assumed
Frenzen(1974)	0.36($\pm$0.01)	See Garratt (1974)
Högström (1974)	0.35($\pm$0.03)	$\alpha_u = 0.55$ was assumed
Hicks (1976)	0.4	
Garratt(1977)	0.415($\pm$0.02)	inferred from C_f data
Wieringa (1980)	0.41	Re-analysis of the Kansas data used by Businger et al. (1971)
Francey & Garratt(1981)	0.38($\pm$0.04)	$\phi_m(\zeta) = (1 - 15.5\zeta)^{-1/4}$ was used
Shirasawa (1981)	0.42($\pm$0.03)	$|\zeta| \leq 0.1$ or 0.03
Kondo & Sato(1982)	0.39($\pm$0.03)	$|R_i| \leq 0.02$ or 0.05
Dyer & Bradley (1982)	0.385($\pm$0.021)	0.4 was suggested
Telford (1982)	0.37	"Theoretical Value"
Frenzen & Hart (1983)	0.41	$\alpha_u = 0.52$ was assumed
Högström (1985)	0.4($\pm$0.011)	0.36 suggested by Telford & Businger (1986)
Högström (1986)	0.39($\pm$0.01)	
Högström (1988)	0.4	
Zhang (1988)	0.4	
Frenzen & Vogel (1992)	0.38($\pm$0.017)	

Table 2.1 (SOURCE: Cai's Ph.D. thesis, 1993)

zero (denoted as z_0) to a reference height z—yields the following mean wind profile,

$$U(z) = \frac{u_*}{k}\ln\frac{z}{z_0}.$$ (13)

It shows that the mean wind profile is logarithmic in height within the surface layer. This is the well-known *"law of the wall"* in engineering term.

In deriving (13), we learn that the *roughness height* z_0 is defined as the height where the mean wind becomes zero if we extrapolate the logarithmic profile all the way down (Fig. 2.4). The roughness height z_0 is not a physical height where the mean wind actually goes to zero, because there exists a viscous layer (below the inertial sublayer) where the wind profile is not logarithmic.

In 1954, Monin and Obukhov applied the similarity-theory concept to stratified atmospheric surface layer. They assumed that with stratification relevant parameters should include not only u_* and z but also buoyancy parameters $\frac{g}{T_0}$ and the surface temperature flux
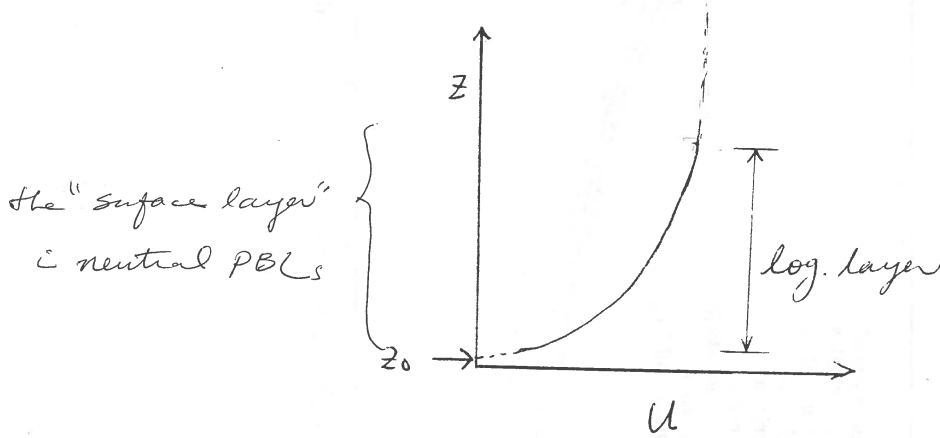
Figure 2.4

$\overline{w'\theta'}_0$. The only combination of including all these parameters to form a non-dimensional parameter is z/L, where $L = -u_*^3/[k\frac{g}{T_0}\overline{w'\theta'}_0]$ is called *Monin-Obukhov length*.

Therefore, the non-dimensional vertical gradient of mean wind is written as a function of the non-dimensional parameter z/L:

$$\frac{kz}{u_*}\frac{\partial U}{\partial z} = \phi_m(\frac{z}{L}), \tag{14}$$

where ϕ_m is a universal function. Formula (14) relates the mean wind shear to all of the relevant parameters in a stratified surface layer. Again the universal function cannot be determined by theory; it can only be estimated from measurements. There existed many field studies that were designed to find this *stability function ϕ_m*. Some of these measurements and their results for ϕ_m are listed in Table 2.2 (again taken from Cai's thesis). Each measurement came up with its own empirically-fitted formula, but these formulae are really not very different from each other, as shown in Fig. 2.5a.

Similarly, the non-dimensional vertical gradient of the mean temperature can be written as

$$\frac{kz}{\theta_*}\frac{\partial \Theta}{\partial z} = \phi_h(\frac{z}{L}), \tag{15}$$

where $\theta_* = -\overline{w'\theta'}_0/u_*$. Again ϕ_h is another universal function to be determined empirically.

Since (14) and (15) relate the flux parameters u_* and θ_* to the vertical gradients of the

22

J.2

Table 2.2: Estimates of $\phi_m(\zeta)$ from measurements for unstable surface layer

| Source	$\phi_m(\zeta)$	
Panofsky *et al.* (1960)	$\phi_m^4 - 9\zeta\phi_m^3 = 1$	KEYPS formula
Dyer and Hicks (1970)	$(1 - 16\zeta)^{-1/4}$	$-1 \le \zeta \le 0$
Businger *et al.* (1971)	$(1 - 15\zeta)^{-1/4}$	$-2 \le \zeta \le 0$
Carl *et al.* (1973)	$(1 - 16\zeta)^{-1/3}$	$-10 \le \zeta \le -2$
Wieringa (1980)	$(1 - 22\zeta)^{-1/4}$	$-2 \le \zeta \le 0$
Dyer and Bradley (1982)	$(1 - 28\zeta)^{-1/4}$	$-4 \le \zeta \le -0.004$
Kai (1982)	$(1 - 7\zeta)^{-1/4} - 0.2$	$-0.1 \le \zeta \le 0$
Korrell *et al.* (1982)	$(1 - 15\zeta)^{-1/3}$	$-0.6 \le \zeta \le 0$
Foken and Skeib (1983)	1	$-0.06 \le \zeta \le 0$
	$(-\zeta/0.06)^{-1/4}$	$-2 \le \zeta \le -0.06$
Högström (1988)	$(1 - 19\zeta)^{-1/4}$	$-3 \le \zeta \le 0$
Frenzen and Vogel (1992)	$(1 - 22.6\zeta)^{-1/4}$	$-0.6 \le \zeta \le 0$
	$(1 - 15.1\zeta)^{-1/3}$	$-0.6 \le \zeta \le 0$

Table 2.2 (SOURCE: Cai's Ph.D. thesis, 1993)

Figure 2.5a

23
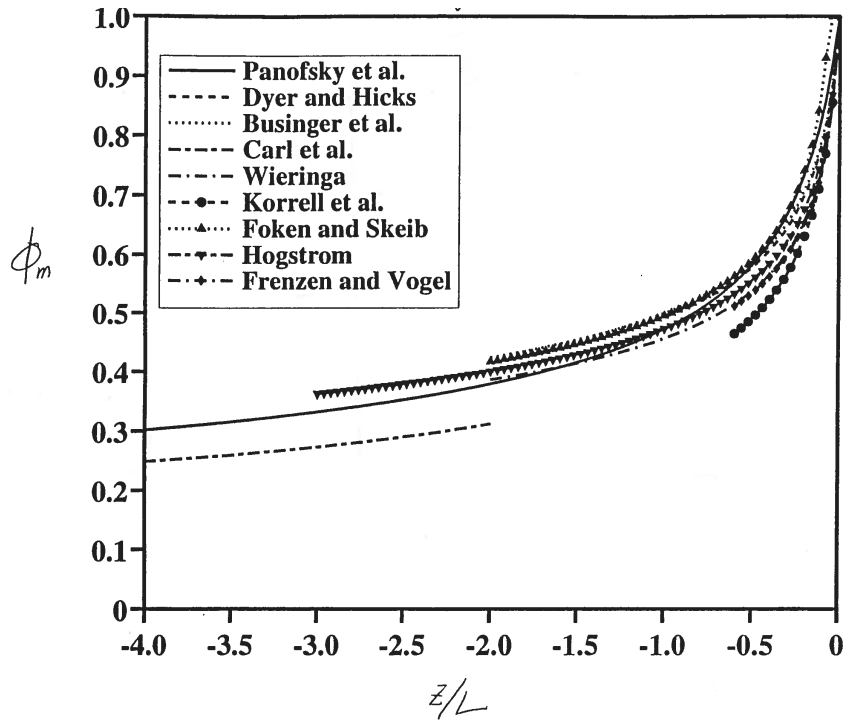
mean field, they are also referred to as *flux-gradient relationships.*

If you choose to use the Businger's formulae (see Businger et al 1971, JAS, 28, 181-189), shown in Fig. 2.5b, then vertically integrating (14) and (15) (Paulson 1970; JAM, 9,857–861) yields the mean wind profile within the surface layer:

$$\frac{U}{u_*} = \frac{1}{k}(\ln\frac{z}{z_0} - \Psi_1) \quad \text{for unstable case,} \tag{16}$$

$$\frac{U}{u_*} = \frac{1}{k}(\ln\frac{z}{z_0} + 4.7\frac{z}{L}) \quad \text{for stable case,} \tag{17}$$

and the mean temperature profile,

$$\frac{\Theta - \Theta_0}{\theta_*} = \frac{0.74}{k}(\ln\frac{z}{z_0} - \Psi_2) \quad \text{for unstable case,} \tag{18}$$

$$\frac{\Theta - \Theta_0}{\theta_*} = \frac{0.74}{k}(\ln\frac{z}{z_0}) + \frac{4.7}{k}\frac{z}{L} \quad \text{for stable case,} \tag{19}$$

where Θ_0 is the extrapolated temperature at z_0, which is not necessarily the actual surface temperature. Here $\Psi_1 = 2 \ln[(1+x)/2] + \ln[(1+x^2)/2] - 2\tan^{-1}(x) + \pi/2$ with $x = (1-15z/L)^{1/4}$, and $\Psi_2 = 2 \ln[(1+y)/2]$ with $y = (1-9z/L)^{1/2}$. (See Businger, J. A., 1973: *Turbulent Transfer in the Atmospheric Surface Layer*, in *Workshop on Micrometeorology*, Ed. D.A. Haugen, AMS.)

Formulae (16, 17) and (18, 19) can be used in two ways: Given the air temperature at z_0 and the wind and temperature at any height *within* the surface layer, we can determine u_* and θ_*, which then give the surface fluxes of momentum and temperature. On the other hand, given the surface fluxes we can use these formulae to find the mean wind and temperature profiles within the surface layer. From these formulae, we can also determine the drag coefficients C_D and C_H used in the bulk aerodynamic method: $\overline{u'w'}_0 = -C_D|\vec{V}|U$ and $\overline{w'\theta'}_0 = -C_H|\vec{V}|(\Theta - \Theta_0)$. It is important to remember that in order to use the flux-gradient relationships, the reference level z has to be within the surface layer because "constant flux" is assumed in their derivations.

The physical meaning of the Monin-Obukhov length is clear if you look at the Reynolds average TKE equation, which you derived in Homework 1C. The shear production term is on the order of u_*^3, whereas the buoyancy production is $\frac{g}{T_0}\overline{w'\theta'}$. So $z \sim L$ is the height
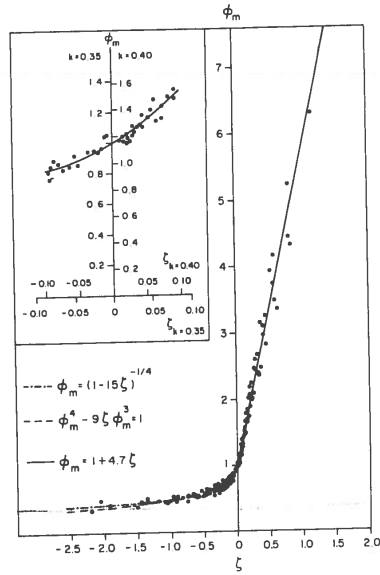
Fɪɢ. 2.1. Comparison of dimensionless wind shear observations with interpolation formulas (after Businger *et al.*, 1971).
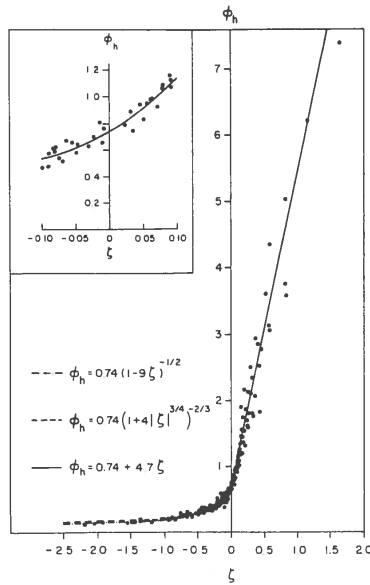

Fɪɢ. 2.2. Comparison of dimensionless temperature gradient observations with interpolation formulas (after Businger *et al.*, 1971).

Figure 2.5b (SOURCE: Businger et al 1971)

where these two TKE productions are about equal; below L, shear production dominates, and above L, buoyancy production dominates.

The TKE budget in the unstable surface layer measured in the field is summarized in Fig. 2.6 by Hogstrom (1990; JAS, 47, 1949–1972) and Wyngaard (1992; Annu. Rev. Fluid Mech. 24, 205–233). Normalized by $u_*^3/\kappa z$, the TKE budget can be expressed in terms of the M-O parameter z/L. First, the normalized shear production term ($S \equiv -\frac{\kappa z}{u_*^3}\overline{uw}\partial U/\partial z$ where U is the along-wind component) is simply ϕ_m and the buoyancy production term ($B \equiv \frac{\kappa z}{u_*^3}g\overline{w\theta}/T_0$) is $-z/L$. So these two terms can be expressed as functions of z/L exactly (shown as the two solid curves in Fig. 2.6). The normalized turbulent transport ($T \equiv -\frac{\kappa z}{u_*^3}\partial\overline{wE}/\partial z$) and dissipation term ($\frac{\kappa z}{u_*^3}\epsilon$) can be measured in the field; they are both negative. The normalized pressure transport term ($P \equiv -\frac{\kappa z}{u_*^3}\frac{1}{\rho_0}\partial\overline{wp}/\partial z$) cannot be measured accurately in the field and is therefore taken as the imbalance of the above four terms. (In quasi-steady states, $\partial E/\partial t$ is assumed to be zero.) Even with all the data scattering, it is still clear that the pressure transport term is a large gain in the unstable surface layer, first found from the Kansas experiment. This means that the pressure flux, which is zero at the ground, is negative and decreases with height in the surface layer.

In the limit of free convection, i.e., $U = 0$, the above M-O formulae no longer apply. Under this condition, there can still be some amount of u_* that is due to the local horizontal motion induced by thermal convection. This local wind generates local turbulence and local momentum fluxes, and hence $u_* \neq 0$. Businger (1973 BLM, 4, 323–326) proposed u_* proportional to the 1/3 power of the surface heat flux in free convection. Further studies on this topic can be found in Schumann (1988, BLM, 44, 311–326), Sykes et al. (1993, QJRMS, 119, 409–421) and Stull (1994, JAS, 51, 3–22).

For surface fluxes over the ocean, the most used surface-layer formula is from Liu et al. (1979, JAS, 36, 1722–1735) and its update: Fairall et al. (1996, JGR, 101, 3747-3765). Large and Pond (1982, J Phy Ocean, 12, 464–482) also present an extensive set of sensible and latent heat flux measurements over the ocean.

Homework 2:

A. Use (14), along with Businger's ϕ_m formula for the unstable surface layer, to plot (numerically) the drag coefficient $C_D = u_*^2/U_{10}^2$ as a function of z/L for $z_0 = 10^{-4}$ m. Here

U_{10} is the wind speed at $z = 10$ m.

B. Plot u_*^2/U_{10}^2 against z/L using the analytical formula (16), and compare this result with the first plot.
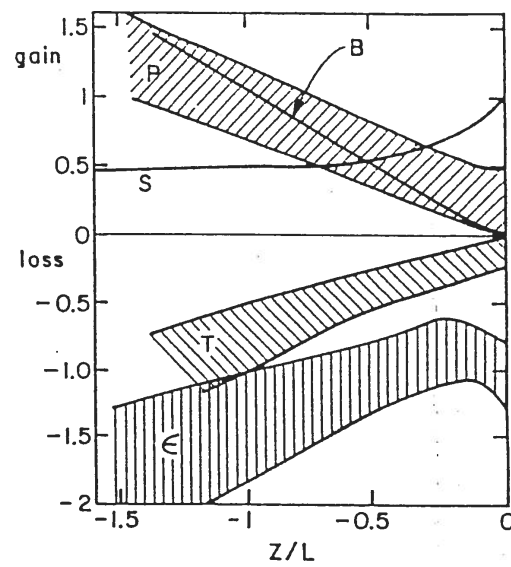

Figure   The budget of turbulent kinetic energy in the unstable surface layer. The shaded areas represent the spread of measurements from experiments summarized by Hogstrom (1990). *B* represents buoyant production; *P*, pressure transport; *S*, shear production; *T*, turbulent transport; and ε, viscous dissipation.

Figure 2.6 (SOURCE: Hogstrom 1990)
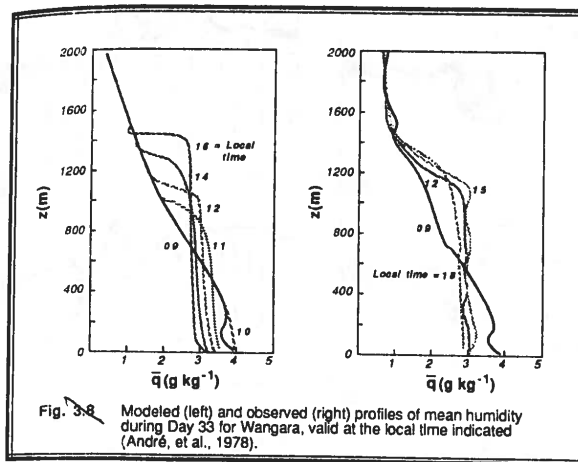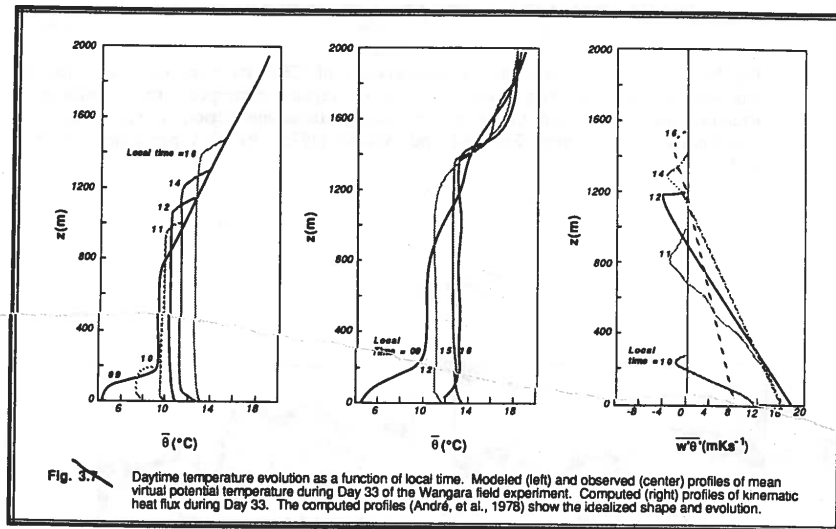
3   THE CLEAR CONVECTIVE PBL

When the sun warms up the ground, warm (lighter) air parcels (in the form of thermals or plumes) tend to rise. This is how convection can effectively generate turbulence on sunny days. The intensity of convectively driven turbulence is often very strong so it can quickly mix all conserved variables within the bulk of the PBL. Hence the clear convective PBL (CBL) is also called the *mixed layer*. (The term "mixed layer" is sometimes confused with uniformity. Turbulence does not mix spatial structure of flows such as local wind or local temperature to make them *uniformly distributed* in space or time. As described in section 1.4.3, the well-mixed quantities are the statistical properties, such as horizontally averaged mean wind and potential temperature.)

A typical sounding after the sun rises is shown in Fig. 3.1. The CBL grows in time via entrainment (to be explained later) and the mean potential temperature and moisture mixing ratio are well (or nearly) mixed within the bulk of the CBL. Notice also that the vertical profiles of heat flux are linear with height.

A typical CBL consists of three layers. The lowest 5-10% is the surface layer where small eddies dominate and the temperature lapse rate is superadiabatic (unstable surface layer). The middle 80-90% of the PBL is the well mixed layer where the temperature lapse rate is almost adiabatic. The top 5-10% is the *entrainment zone*, which is a layer consists of the undulation of the interface between the turbulent PBL and the overlying (often warmer) free atmosphere. The (local) interface, which can be sharp, moves up and down in space and time due to turbulent motion, so after averaging (either spatial or time or ensemble), the undulation forms a layer of finite thickness. The entrainment zone of the CBL is often characterized by temperature inversion, penetrating thermals, intermittent turbulence, internal gravity waves, and entrainment events.

3.1   Thermal or plume structures

There is increasing evidence that *coherent structures* (such as thermals, plumes, or roll vortices) carry most of the turbulent fluxes of momentum, heat, and other scalars. Therefore, many studies are aimed at understanding these structures. Some researchers hope to use coherent structures to describe turbulence properties, instead of using the traditional

Fig. 3.7   Daytime temperature evolution as a function of local time. Modeled (left) and observed (center) profiles of mean virtual potential temperature during Day 33 of the Wangara field experiment. Computed (right) profiles of kinematic heat flux during Day 33. The computed profiles (André, et al., 1978) show the idealized shape and evolution.

Fig. 3.8   Modeled (left) and observed (right) profiles of mean humidity during Day 33 for Wangara, valid at the local time indicated (André, et al., 1978).
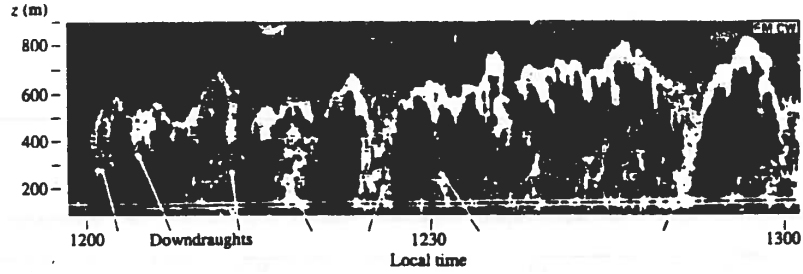
Figure 3.1 (SOURCE: Stull's textbook)

Figure 3.2 (SOURCE: Garratt's textbook 1992)

ensemble-mean statistics, which bury all the details of turbulent motions within the averages.

Within the CBL, thermals with a size of the PBL depth are the dominant structure. To "see" the whole picture of these structures, we rely mainly on radar or LES. Figure 3.2 displays radar return echoes near the PBL top, which shows thermals penetrating into the capping inversion. Based on observations, convection tank experiments and LESs, we form the following picture of turbulence structure in the CBL: Near the heated surface, warm air tends to converge at the narrow edges of irregular polygons (see Fig. 2.3), which are also where positive vertical-velocity fluctuations locate (but not always because of the nature of turbulence). Warm air parcels that exist at the intersects of polygons are likely to become strong updrafts and travel all the way up to the inversion. These form large-eddy thermals (or plumes). When thermals impinge onto the inversion, the stratification prevents them from going further up so they return back to the turbulent layer. Upon returning, they engulf (or push) some inversion air into the turbulent layer (Fig. 3.3 taken from Sullivan et al. 1998, 55, 3042–3064, JAS). We believe that these large-eddy impinging and engulfing processes, rather than small-scale mixing at the interface, are responsible for most of the entrainment of inversion air into the clear convective PBL. Small-scale mixing (of the turbulent and laminar flows) across the interface also occurs but it is likely to contribute only a small portion of the net entrainment in the CBL.

Downdrafts must fill in space between rising thermals (updrafts) because of mass continuity. These downdrafts are compensating motion and hence must be weaker than updrafts. This means the vertical velocity field is positively skewed. Since the mean vertical motion of turbulence is zero, the area covered by stronger updrafts (σ_u) then must be smaller than that covered by weaker downdrafts (σ_d), i.e., $w_u\sigma_u + w_d\sigma_d = 0$ and hence $w_u/|w_d| = \sigma_d/\sigma_u$.
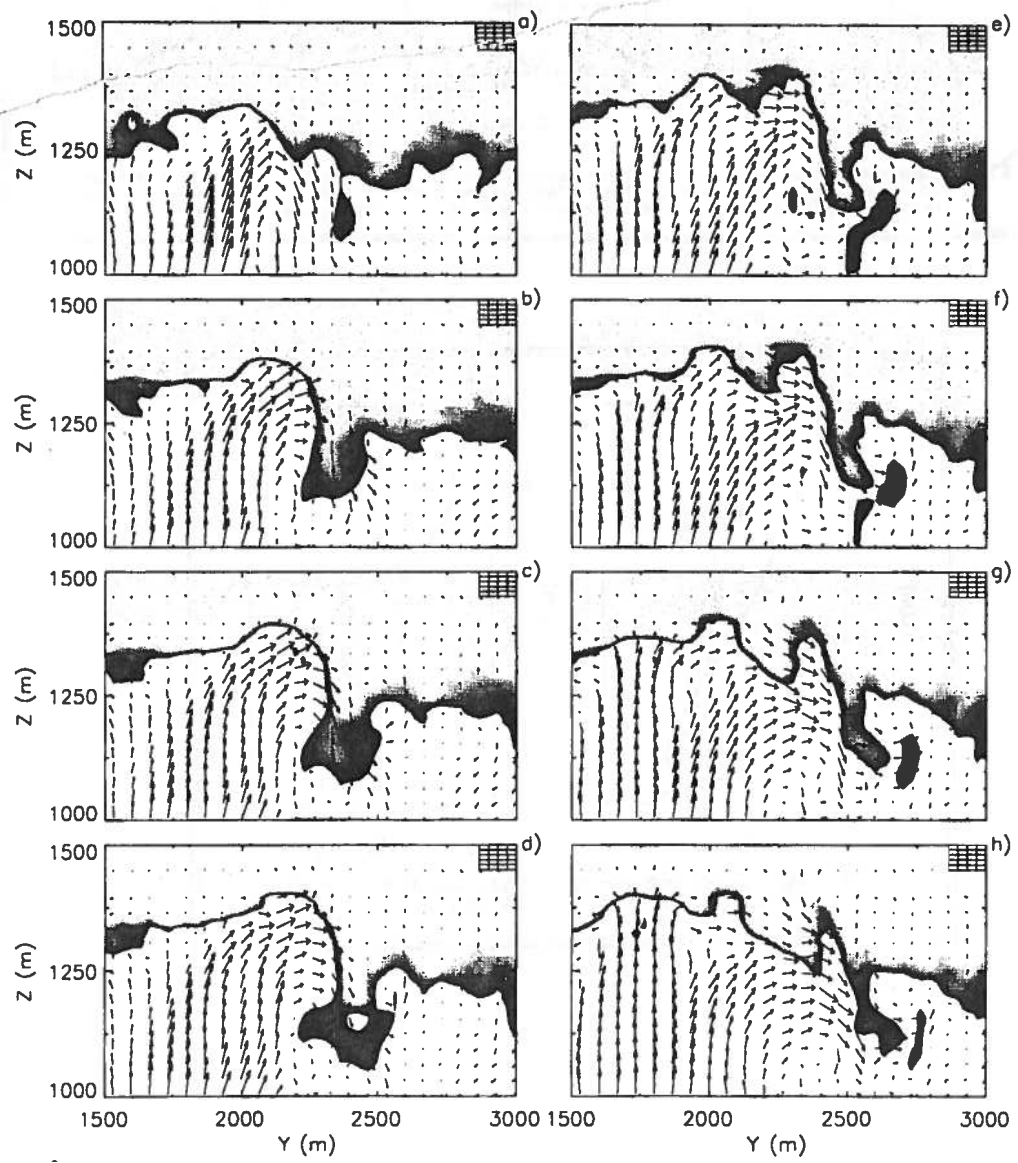
30

Figure 3.3 (SOURCE: Sullivan et al. 1998)

31

The skewed vertical velocity field has a strong impact on plume dispersion, as we will learn in section 3.5.

Thus, instead of transporting momentum and heat (and other scalars) locally like molecular diffusion, most of the transport is through large thermals. This feature results in *nonlocal transport* because large thermals can quickly carry fluxes all the way to the PBL top without much mixing with their surrounding downdrafts. Recognizing this highly efficient transport process, many PBL models include nonlocal transport effects for the CBL.

Another type of coherent structure in the CBL is convective rolls (or referred to as roll vortices), which was first observed in the field by Kuttner (1959, Tellus, 11, 267–294). These are quasi two-dimensional horizontal vortices. With sufficient moisture, they form cloud streets which are visually recognizable. Cloud streets exist in many different large-scale environments. They exist over the subtropical ocean where the mean wind is sufficiently strong and the surface sensible heat flux not very large (i.e., in the small $-z_i/L$ regime; e.g.,LeMone 1973; JAS, 30,1077-1091). Cloud streets also exist in cold air outbreak over warm water where the surface sensible heat flux is large (e.g., Chou and Ferguson; 1991, BLM, 55, 255–282). The cloud streets observed in these two regimes may have similar dynamical circulations, but they are likely to form from different instability mechanisms. Horizontal rolls also exist in cloudless convective PBLs, which are observed from Dual-Doppler-Radar (e.g., Kropfli and Kohn 1978; JPM, 17,669–676). The aspect ratio (defined as the ratio of the wavelength of the roll circulations to their vertical extent) of the observed convective rolls ranges from 2 to 15, as summarized by Etling and Brown (1993; BLM, 65, 215–248).

3.2 Scaling parameters and typical statistics profiles—for the CBL

Turbulence statistics in their dimensional form differ case by case because of different surface forcing, geostrophic wind, or different sounding. But with proper scaling, most turbulent statistics of the CBL collapse onto some universal curves, even though data are taken from different cases. This is another application of the so-called *similarity or scaling argument.* In other words, if we can come up with proper scaling parameters, turbulent statistics obtained from a wide range of meteorological conditions can be normalized in such a way that their non-dimensional statistics are similar. We should thank Deardorff for finding such a proper

scaling for the CBL.

Before Deardorff's early LES study in 1972, the only known scaling parameters to PBL researchers were friction velocity (u_*) and the Ekman PBL depth (which is proportional to u_*/f). As we know now, these two parameters are relevant only for shear-driven PBL and only without a capping inversion (i.e., the classical Ekman PBL). In that case, the wind stress is the only turbulent energy source and the Ekman layer depth (u_*/f) is the only length scale. However, this hypothetical neutral PBL does not exist in nature. For the CBL, surface heat flux dominates the wind stress in driving turbulence and a capping inversion (which is usually much shallower than u_*/f) limits the growth of the CBL.

Using a rather coarse resolution (by today's standard) in his LES, Deardorff (1972; JAS, 29, 91–115) generated several LESs spanning a range of shear and buoyancy regimes. From those numerical data, he found that the parameters u_* and u_*/f became irrelevant when buoyancy dominates (i.e., $-z_i/L > 4$, where z_i/L will be defined later), but when he used $w_*[\equiv (\frac{g}{T_0}\overline{w\theta}_0 z_i)^{1/3}$ where $\frac{g}{T_0}\overline{w\theta}_0$ is the surface buoyancy flux] and z_i instead, he was able to collapse all of his LES solutions for larger $-z_i/L$ into one curve, as shown in Fig. 3.4. The parameter w_* is called the *convective velocity scale*. Deardorff also proposed a temperature scale for the CBL as $T_* \equiv \overline{w\theta}_0/w_*$. This set of parameters is now known as the *"mixed-layer scaling"*. (From now on, I will neglect the prime symbol for turbulent fluctuations.) The ratio of w_* and u_* is related to the mixed-layer stability parameter as: $w_*/u_* = (-z_i/L)^{1/3}$, and is an indication of relative importance of surface buoyancy vs. surface shear effects in driving turbulence.

Figure 3.5 classifies the PBL into five regimes using the parameter z_i/L: the strong convective forcing CBL, mix of shear and buoyancy driven PBL, neutral PBL, weakly stable PBL, and strongly stable PBL. The above mixed-layer scaling only works for the CBL regime.

[The mixed-layer scaling is different from the surface-layer scaling. The length and velocity scales for the mixed layer are z_i and w_*, while those for the surface layer are z and u_*. The stability parameter for the mixed layer is z_i/L, vs. z/L for the surface layer.]

First studies that used the mixed-layer scaling to analyze field data were made by Lenschow (1974; JAS, 31, 465–474) and Lenschow et al. (1980, JAS, 37, 1313–1324), on aircraft data over the entire CBL. The data used in the latter study were from the well-known AMTEX (Air Mass Transformation Experiment) experiment. That study showed
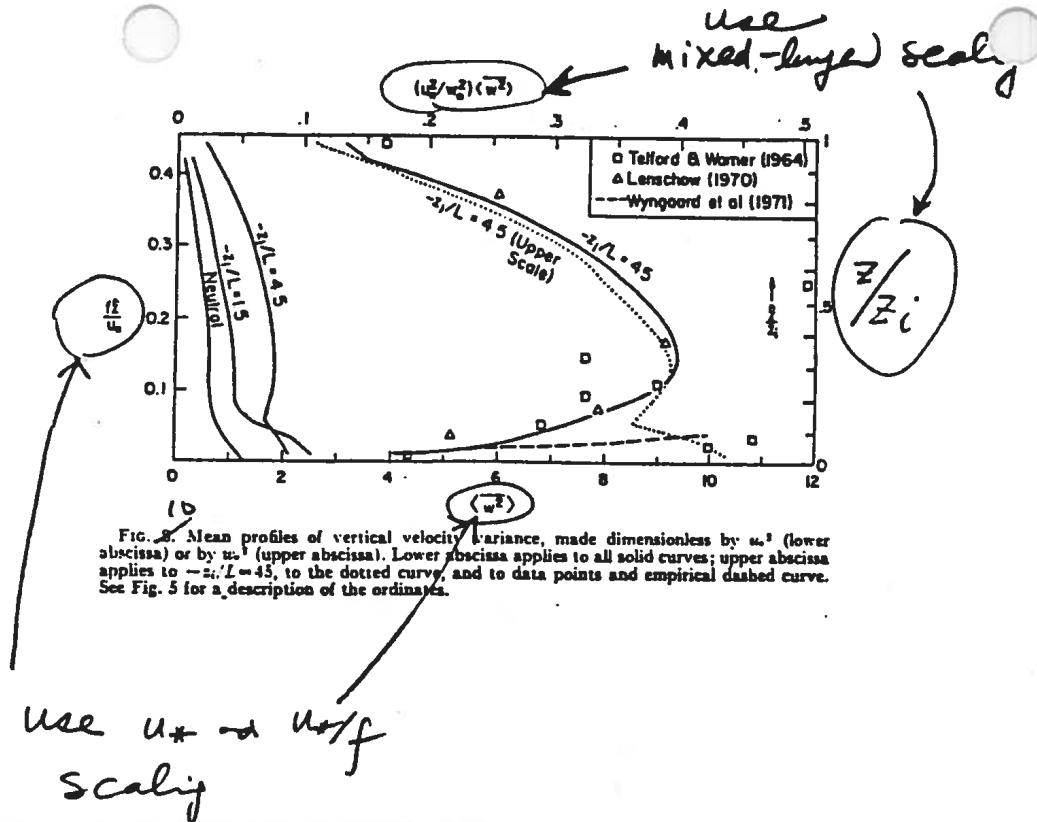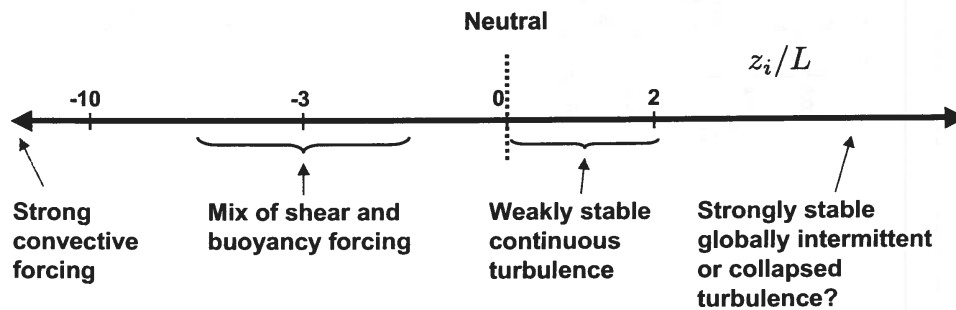
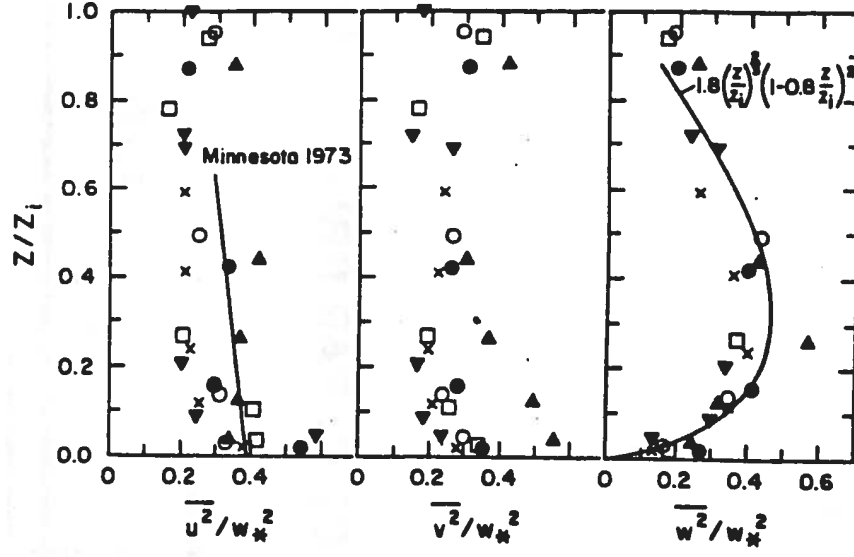Figure 3.4 (SOURCE: Deardorff 1972)

Figure 3.5

34

Figure 3.6 (SOURCE: Lenschow et al 1980)

the vertical distributions of many second- and third-moment statistics—scaled with the above mixed layer parameters—within the CBL. Here I show some of them: the normalized velocity variances in Fig. 3.6, heat flux in Fig. 3.7, vertical fluxes of velocity variances (3rd moment statistics) in Fig. 3.8. The overall distribution of normalized TKE budgets (taken from Stull's book) is shown in Fig. 3.9.

Some of the above profiles are now considered "typical" in the CBL. They have the following features:

(1) The two components of the horizontal-velocity variances within the CBL are about the same, indicating horizontal isotropy. These variances have two local maxima: one at the wall and the other at the capping inversion.

(2) The vertical-velocity variance peaks at about $0.4z_i$ with a maximum of about $0.4w_*^2$.

(3) For clear convective PBL, the buoyancy flux (Fig. 3.7), or the buoyancy production (BP-curve in Fig. 3.9), almost always linearly decreases with height. This is because that the vertical shape of the mean temperature remains unchanged in a horizontally-homogeneous, quasi-steady state, i.e.,

$$\frac{\partial}{\partial t}\frac{\partial \Theta_v}{\partial z} \sim 0 \sim -\frac{\partial^2}{\partial z^2}\overline{w\theta_v}. \tag{20}$$

35
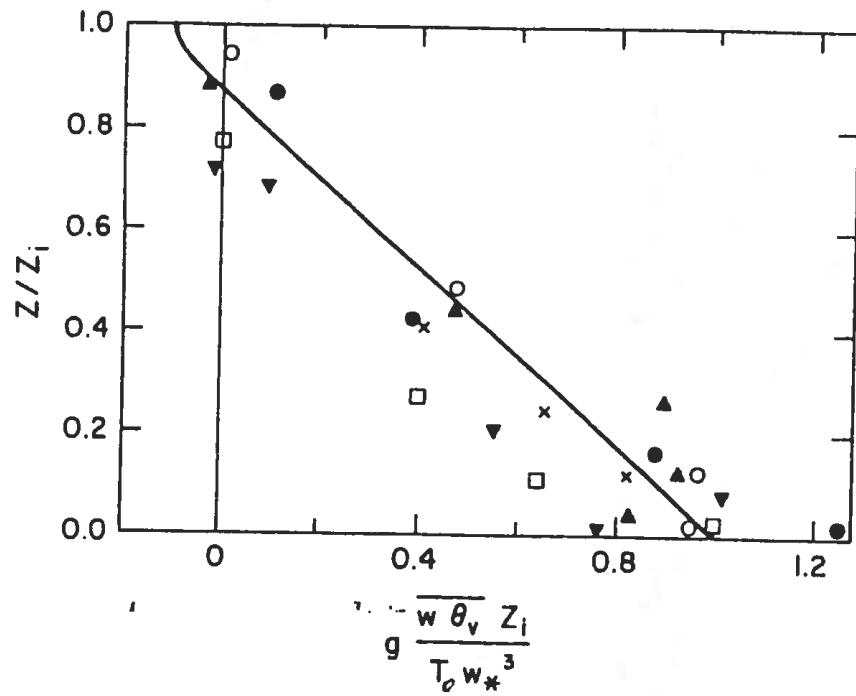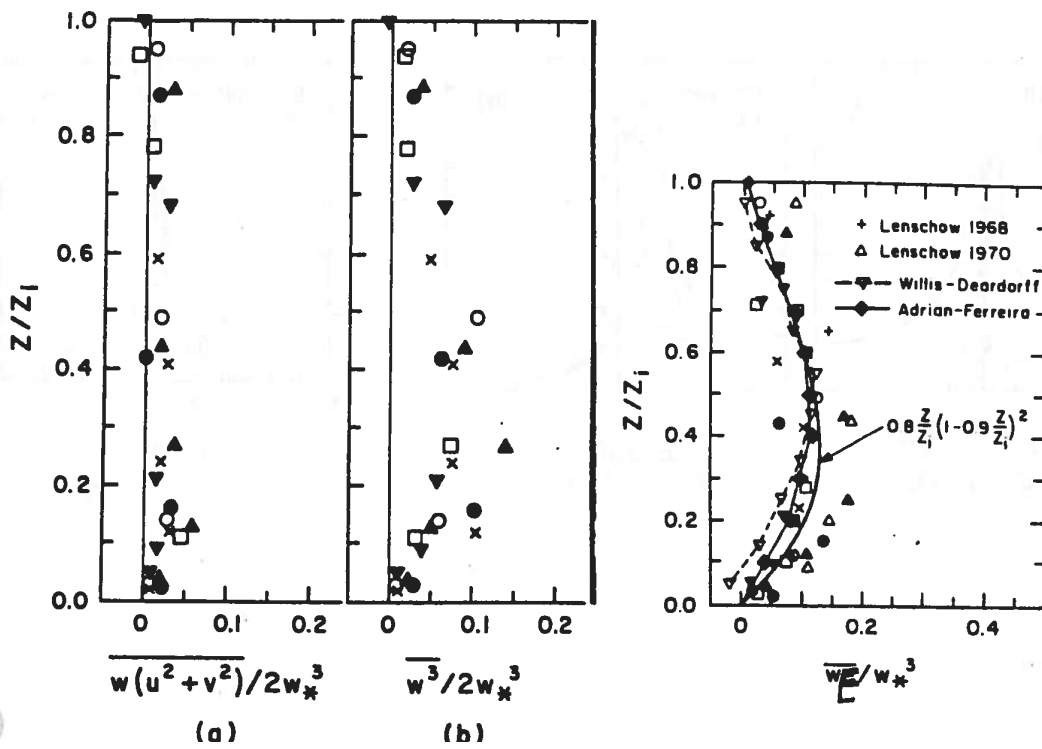
Figure 3.7 (SOURCE: Lenschow et al 1980)

Figure 3.8 (SOURCE: Lenschow et al 1980)

36

Fig. 3.4 Normalized terms in the turbulence kinetic energy equation. The shaded areas indicate ranges of values. All terms are divided by w_*^3 / z_i, which is on the order of $6 \times 10^{-3} m^2 s^{-3}$. Based on data and models from Deardorff (1974), André et al. (1978), Therry and Lacarrere (1983), Lenschow (1974), Pennell and LeMone (1974), Zhou, et al. (1985) and Chou, et al. (1986).
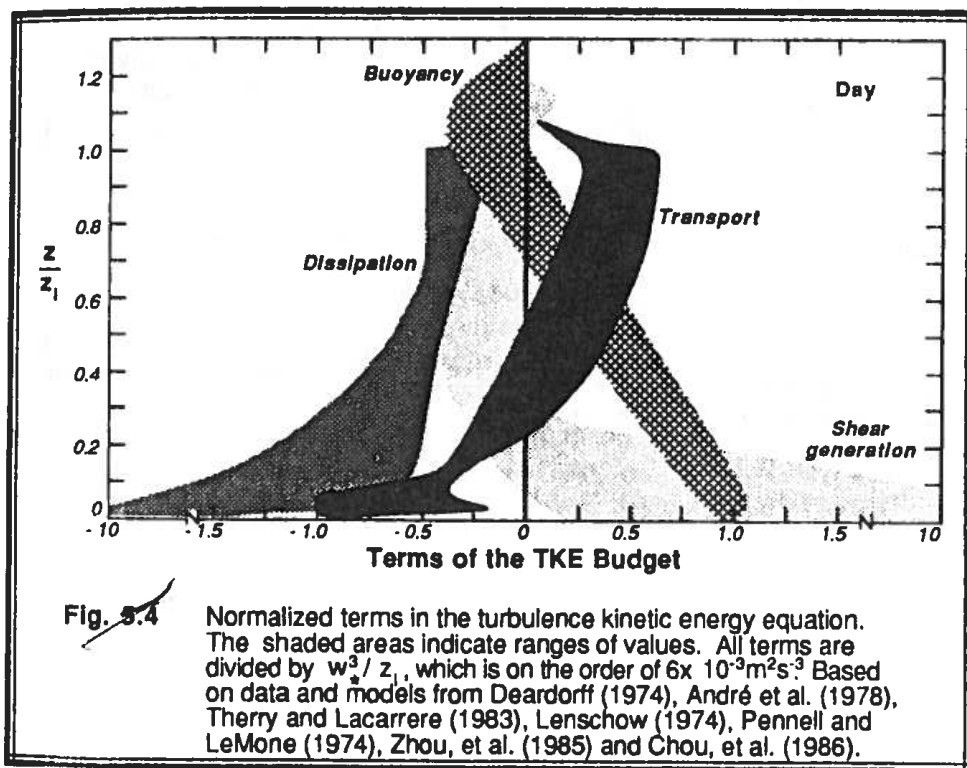
Figure 3.9 (SOURCE: Stull's textbook)

Thus, the curvature of the buoyancy flux should be zero within bulk of the mixed layer. This linearity is true for all conservative scalars, such as the moisture flux. The normalized buoyancy flux is 1 at the surface and about –0.2 at the PBL top. And hence the relationship $\overline{w\theta}_{z_i} \sim -0.2\overline{w\theta}_0$ is often used to determine the entrainment rate of the CBL. The reason that the ratio of the entrainment buoyancy flux to the surface flux is around –0.2 in the CBL has something to do with the fact that some amount of buoyancy production has to go to dissipation and some converts to potential energy through entrainment. But, the exact mechanism for this ratio is not fully understood. The entrainment fluxes of other scalars (such as moisture and ozone), however, vary greatly from case to case, depending on the vertical distributions of their mean concentration (such as vertical gradient across the CBL top). There is no -0.2 rule for other scalars.

(4) The vertical flux of vertical-velocity variance, $\overline{w^3}$, which peaks at mid-PBL, is much larger than $\overline{wu^2}$ and $\overline{wv^2}$. Using $\overline{w^2}$ and $\overline{w^3}$ shown in Figs. 3.6 and 3.8, we can calculate the vertical velocity skewness, defined as $\overline{w^3}/\overline{w^2}^{3/2}$; it is about $1 \sim 2$ throughout the whole CBL, a large positively skewed w-field.

(5) Unlike shear-driven turbulence, the transport term due to TKE-flux and pressure are also large in the CBL. However, the two transport terms tend to cancel each other (which we don't know why), and the net effect is a smaller transport. The net effect of the two transport terms is a vertical redistribution of the TKE from the lower CBL to the upper CBL. The major contributor to the turbulent transport term is the large $\overline{w^3}$, shown in Fig. 3.8. A large positive $\overline{w^3}$ is associated with a large skewed w-field. Thus, the larger the w-skewness (such as in the cumulus-cloud layer), the more important the turbulent transport term becomes in the TKE budget. This makes the prediction of TKE budget in a large skewed condition more difficult, because the turbulent transport term involves third moment statistics which requires closure assumptions. Note that the vertical integration of the net transport over the whole PBL is zero, since $\int_0^{z_i}[\partial\overline{wE + wp}/\partial z]dz$ equals to the difference of the fluxes $\overline{wE + wp}$ at (or just above) the top and the bottom of the PBL, which are zero in most cases. So these two transport terms cannot generate or consume TKE; they just redistribute

the TKE vertically.

(6) The dissipation term is nearly constant in the bulk of CBL (although Fig. 3.9 shows its magnitude decreases with height, LESs show this term to be nearly constant in the middle of the CBL). Its magnitude can be estimated as follows: When the shear production is negligibly small, the buoyancy flux at the PBL top is roughly –0.2 of the surface flux. By layer integrating the TKE budget from the surface to the PBL top, the two transport terms drop out, we obtain the layer integrated dissipation rate as:

$$-\int_0^{z_i} \epsilon dz \sim 0.4 \frac{g}{T_0} \overline{w\theta_{v0}} = 0.4 \frac{w_*^3}{z_i}. \tag{21}$$

The statistics of the CBL regime obtained from LESs (e.g., shown in Fig. 3.10b) compare well with those shown in Figs. 3.6–3.9, except that the simulated dissipation term are more constant in height. The convection tank results from Deardorff and Willis (1985, BLM, 32, 205–236) also show similar statistical profiles as those observed, implying that the medium-R_e tank convection is in the R_e-independent regime.

3.3 Scaling parameters and typical statistics profiles—for weakly convective near-neutral PBL

When the PBL is only weakly convective and the wind is strong, both buoyancy and shear become dominant sources in generating TKE. Then the above mixed layer scaling (which works only for buoyancy dominant CBL) no longer applies. The mixed shear-buoyancy driven PBL ($0 < -z_i/L < 4$) exists mostly over the ocean. It rarely exists over land because the land heats up after sunrise and cools down after sunset very quickly.

We don't have "typical" statistics profiles for this mix shear-buoyancy PBL regime. The reasons are: (1) the shear-also-dominant CBL exists mainly over ocean where observations are difficult to carry out; (2) they are often associated with clouds, which complicate the statistics; and (3) we don't have a proper scaling law (likely with various combinations of convective velocity w_* and friction velocity u_*) to normalize the data.

Moeng and Sullivan (1994; JAS, 51, 999–1022) performed two LESs of this PBL regime (for $-z_i/L \sim 1.4$ and 1.6) shown in Fig. 3.11. The simulated TKE budget from SB1 is
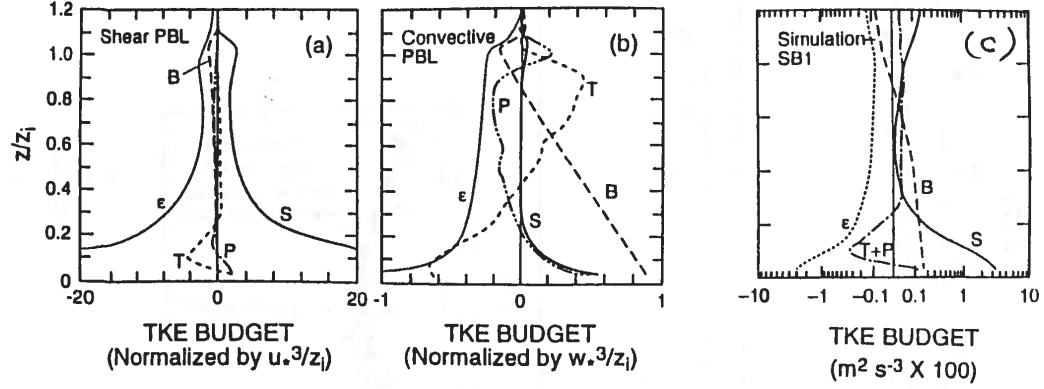
Figure 3.10 (SOURCE: Moeng and Sullivan 1994)

given in Fig. 3.10c, to compare to those of pure shear driven PBL (Fig. 3.10a) and the CBL (Fig. 3.10b). Both shear and buoyancy productions are significant in the TKE budget. Below I summarize the difference between the mix shear-buoyancy CBL regime from the buoyancy-only CBL:

(1) With increasing shear, statistics of the along-geostrophic-wind component becomes increasingly dominant, such as $\overline{u^2}$ and $\overline{wu^2}$, comparing to those of the vertical component. Statistics of the cross-wind component increasingly differ from their along-wind-component counterparts, i.e., an increasing in horizontal anisotropy.

(2) The vertical velocity variance $\overline{w^2}$ becomes smaller compared to the horizontal velocity variances and more uniform with height. It no longer shows a significant peak in the mid-PBL.

(3) The ratio of entrainment-to-surface buoyancy flux is now larger in magnitude (Fig. 3.11) compared to the CBL. The two mixed shear-buoyancy driven PBLs simulated by Moeng and Sullivan show an entrainment buoyancy flux that is about –0.5 of the surface buoyancy flux. This change of the entrainment/surface flux ratio, from $\sim$ –0.2 to $\sim$ −0.5, is clearly due to the increasing surface-stress (or perhaps shear across the entrainment zone) effect. When the entrainment buoyancy flux formula is generalized to include the u_* effect as $w_m = (w_*^3 + 5u_*^3)^{1/3}$ based on their LES solutions, Moeng and Sullivan show $-\overline{w\theta}_i \sim 0.2 w_m^3/z_i$. This gives a ratio of entrainment-to-surface buoyancy fluxes that is larger than 0.2 in magnitude.
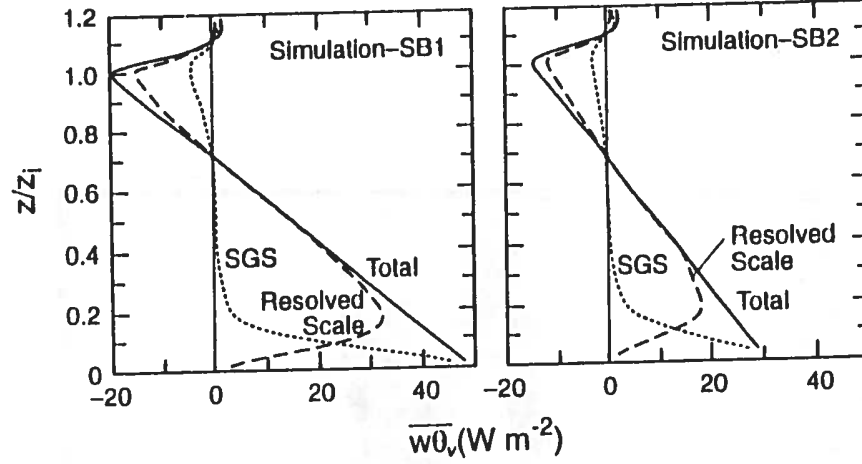
40

Figure 3.11 (SOURCE: Moeng and Sullivan 1994)

3.4 Spectra

We have learned in section 1.4.5 that Kolmogorov theory predicts the velocity spectrum in the inertial subrange as

$$S(k) \propto \epsilon^{2/3} k^{-5/3}, \tag{22}$$

which is expressed in the wavenumber space (spatial fluctuations). To analyze data in time series (time fluctuations), such as tower or balloon measurements, we use Taylor hypothesis to approximate wavenumber by frequency (n) as $k = n/U$. After multiplying both sides by n, we can express the spectrum in frequency space as:

$$nS(n) \propto \epsilon^{2/3} \, n^{-2/3}. \tag{23}$$

Using the mixed-layer scaling law, i.e., normalizing $n \, S(n)$ by w_*^2, dissipation rate by w_*^3/z_i, and the wavelength by z_i, the dimensionless form of (23) becomes:

$$\frac{nS(n)}{w_*^2} \propto \psi^{2/3} f_i^{-2/3}, \tag{24}$$

where $\psi \equiv \epsilon z_i/w_*^3$ is dimensionless dissipation rate and $f_i \equiv nz_i/U$ dimensionless frequency.

Kaimal et al. (1976; JAS, 33, 2152–2169) analyzed the Minnesota balloon data of the CBL $(-z_i/L > 30)$ using the above mixed-layer scaling. They presented (Fig. 3.12a) the 1-D spectra of u, v, and w along the wind direction at different heights within the CBL. For

41

isotropic turbulence, 1D spectra can be shown theoretically to have the same power law—also -5/3—as the 3-D spectra but with a different proportionality constant (ref: p. 253-254, Tennekes and Lumley). As far as I know, there is no theory that shows that 2D spectra of wind or temperature in the PBL also obey the -5/3 power law.

Figure 3.12b plots the peak wavelength of these spectra and also of the temperature spectrum. What Fig. 3.12 tells us are:

(1) Spectra of all three velocity components in the CBL can be generalized with the mixed-layer scaling because the inertial subrange spectra all collapse into one representative curve.

(2) The peak value of dimensionless longitudinal spectrum [which is defined as the spectrum of the velocity component that is parallel to the wavenumber direction, e.g., $S_u(k_x)$ is longitudinal spectrum] is about 0.15, whereas the peak of lateral spectrum [defined as the spectrum of the velocity component that is perpendicular to the wavenumber direction, e.g., $S_v(k_x)$ or $S_w(k_x)$ is lateral spectrum] is about 0.2. Longitudinal and lateral spectra are different. For isotropic turbulence, the lateral spectrum can be shown theoretically to be 4/3 of the longitudinal spectrum (ref: page 254 in Tennekes and Lumley's book).

(3) The characteristic wavelength, λ_m, where the spectrum peaks, is about $1.5z_i$ for u and v fields throughout the whole CBL.

(4) The characteristic wavelength for w increases linearly from z/z_i=0.01 to z/z_i=0.1, increases more gradually between z/z_i=0.1 and z/z_i=0.2, and then remains nearly constant above $0.2z_i$ at $\lambda_m \sim 1.5z_i$.

LeMone (1980; p. 182–246, *Workshop on the Planetary Boundary Layer*, edited by J. Wyngaard, AMS publication) analyzed the aircraft measurements obtained from GATE and found a somewhat larger λ_m, as shown in Fig. 3.13. The characteristic wavelength within the mixed layer is about 2-3 times larger than that observed by Kaimal et al. (which is shown as the solid curve in Fig. 3.13). This difference may be due to: (1) difference between PBLs over ocean (GATE) and over land (Minnesota data); (2) difference in spatial (aircraft
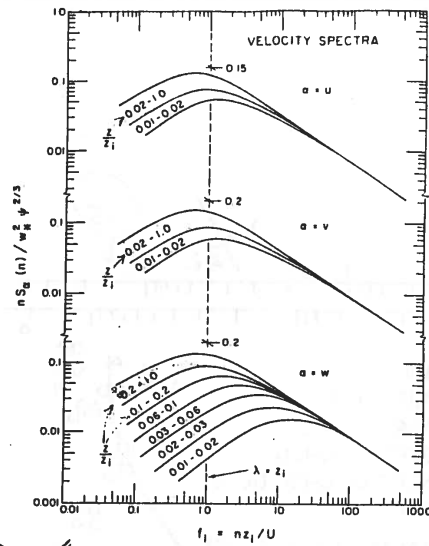
(a)

FIG. 8. Universal curves for velocity spectra expressed in mixed-layer similarity coordinates. The function ψ in the spectral normalization is the dimensionless energy dissipation rate $\epsilon/(g/T)Q_*$.
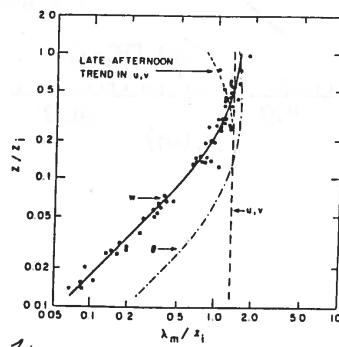
(b)

FIG. 9. Dimensionless peak wavelength for the velocity components and temperature plotted as a function of z/z_i. Scatter in the u, v and θ data points (not shown) is about twice as large as for w.

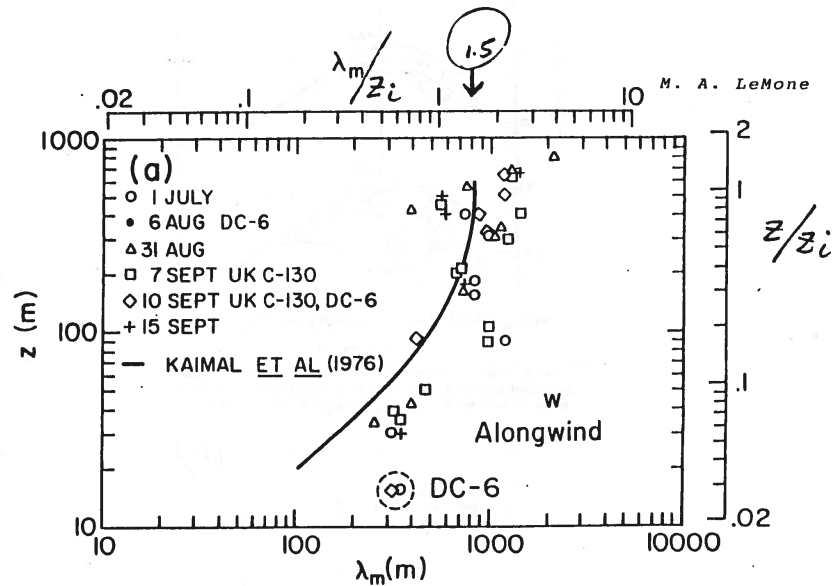Figure 3.12 (SOURCE: Kaimal et al 1976)

Figure 3.13 (SOURCE: LeMone 1980)

measurements) and time fluctuations (balloon measurements); or (3) existence of roll vortices (these rolls have a typical size of 2-3 z_i) in the GATE area.

Unlike the velocity spectra, the temperature and moisture spectra cannot be generalized within the framework of mixed-layer scaling, due to strong influence by entrainment. Remember the mixed-layer scaling does not include entrainment effects.

3.5 Scalar transport

Transporting the scalar fields (e.g., temperature, moisture or chemical species) is one of the important roles of PBL turbulence. Scalar transport by turbulence is crucial for studying air pollution and biogeochemical effects on climate change. In this section we will learn three special properties of scalar transport in the CBL, properties that are not observed in shear-driven turbulence (i.e., not in the neutral and stable PBLs).

3.5.1 Countergradient transport

Back in 1966, Deardorff (1966; JAS, 23, 503–506) observed that heat flux within the CBL was often countergradient, i.e., the flux direction is against the decreasing-of-the-mean direction. In other words, heat does not diffuse downgradient in the CBL. He then developed a theory

in 1972 (Deardorff 1972; JGR, 77, 5900–5904) to model this *countergradient transport*. His theory was based on the heat-flux budget as described in the following. The heat-flux equation

$$\frac{\partial \overline{w\theta}}{\partial t} = -\frac{\partial \overline{w^2\theta}}{\partial z} - \overline{w^2}\frac{\partial \Theta}{\partial z} + \frac{g}{T_0}\overline{\theta^2} - \frac{1}{\rho_0}\overline{\frac{\theta \partial p}{\partial z}} \tag{25}$$

consists of turbulent transport term (1st term on the RHS), mean-gradient production term (2nd), buoyancy production (3rd), and pressure covariance term (4th). (Again, I am going to ignore all the prime notations for all turbulent fluctuating quantities, e.g., $\overline{w'\theta'}$ is simplified as $\overline{w\theta}$.) The effect of pressure fluctuations is to "return" the turbulent motion to an isotropic state, i.e., it reduces the flux which has a preferred direction. Thus, the pressure term is a major sink in any flux budget, and is typically modeled as

$$-\frac{1}{\rho_0}\overline{\frac{\theta \partial p}{\partial z}} = -\overline{w\theta}/\tau, \tag{26}$$

where τ is called *return-to-isotropy* time scale by pressure.

Deardorff assumed that the turbulent transport term (a third moment term) in (25) is negligibly small. Then under quasi-steady states, Eq. (25) becomes

$$0 \sim -\overline{w^2}\frac{\partial \Theta}{\partial z} + \frac{g}{T_0}\overline{\theta^2} - \frac{1}{\tau}\overline{w\theta}. \tag{27}$$

This leads to an expression for the heat flux, as

$$\overline{w\theta} \sim -\overline{w^2}\,\tau[\frac{\partial \Theta}{\partial z} - \frac{g}{T_0}\frac{\overline{\theta^2}}{\overline{w^2}}]. \tag{28}$$

Deardorff then set $K_h = \overline{w^2}\,\tau$ and $\gamma = \frac{g}{T_0}\frac{\overline{\theta^2}}{\overline{w^2}}$ in eq. (28) and obtained

$$\overline{w\theta} \sim -K_h[\frac{\partial \Theta}{\partial z} - \gamma]. \tag{29}$$

The first term is the usual downgradient eddy diffusion term, while the second is a coun-tergradient term. (K_h and γ so defined are always positive.) The reason that γ is called countergradient is because if the mean potential temperature gradient becomes positive, the first term then contributes to a negative flux, but the γ term can keep the flux positive if it dominates the first term. This is particularly true withinin the well mixed layer, where the mean potential temperature gradient is usually negligibly small (due to strong turbulent mixing). But the heat flux remains positive in the bulk part of the mixed layer. Therefore,

the traditional eddy diffusivity approach, $\overline{w\theta} = -K\partial\Theta/\partial z$, would yield an ill-defined K. Adding the countergradient term then guarantees a positive potential temperature flux in the mixed layer where $\partial\Theta/\partial z \sim 0$.

Based on Deardorff's derivation, the countergradient effect comes from the buoyancy term $\frac{g}{T_0}\overline{\theta^2}$ of the heat flux budget, as seen from (28). This is because he derived the equation by assuming that the 3rd moment term in (25) is zero. But now we know (from LESs) that the turbulent transport term is not small and should not be neglected. Other ways to derive the countergradient term were given by Holtslag and Moeng (1991, JAS, 48, 1690–1698) and by Wyngaard and Weil (1991, Phy of Fluid, A3, 155–162), which gave a different physical interpretation to the countergradient term.

3.5.2 Transport asymmetry

In conventional K-models, the same (ad hoc) form of eddy diffusivity K has been applied to describe the diffusion process of all scalar species in the PBL; for example K for heat is also applied to K for moisture. This conventional usage was challenged by Wyngaard and Brost (1984; JAS, 41, 102–112) who argued that eddy diffusivity could be quite different for different scalars, even those scalars are within the *same turbulent flow field*. They introduced the so-called "*top-down and bottom-up*" concept, in which a passive scalar is hypothetically decomposed into two components (according to its flux): *top-down and bottom-up*. Top-down scalar consists of the part of scalar that is "driven" only by its entrainment flux at the PBL top and has a zero flux at the surface, and bottom-up scalar consists of the part of the scalar that is "driven" only by its surface flux and has a zero flux at the PBL top, as shown in the following sketch, Fig. 3.14.

This linear decomposition is made possible because the governing equation for a passive scalar is a linear equation in a given turbulent flow field. Pure top-down and pure bottom-up diffusion may never be found in nature, but there exist some scalars that are close to these two hypothetical scalar components. For example, ozone is often seen as a top-down scalar since its surface flux is much smaller than its entrainment flux. This decomposition is a useful tool to generalize all scalar fields, as we will demonstrate next.

The top-down, bottom-up concept can be mathematically described as the following: The mean concentration of any passive scalar, C, can be split into the top-down and bottom-up
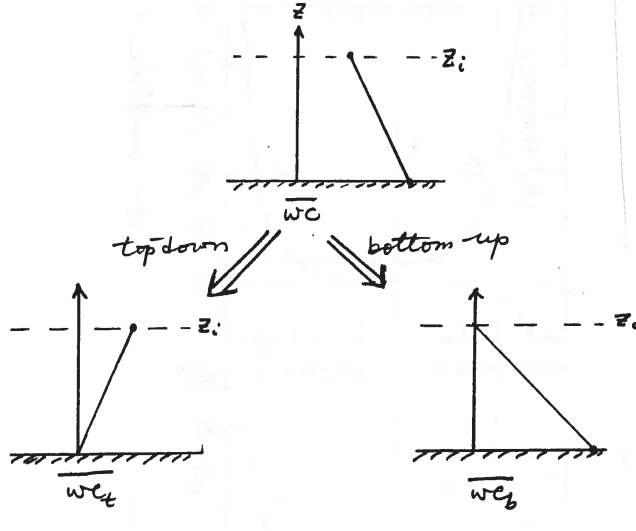
46

Figure 3.14

components,

$$C = C_t + C_b, \tag{30}$$

and thus its mean gradient can be written as

$$\frac{\partial C}{\partial z} = \frac{\partial C_t}{\partial z} + \frac{\partial C_b}{\partial z} = -\Big[\frac{\overline{wc_1}}{w_* z_i}\Big] g_t - \Big[\frac{\overline{wc_0}}{w_* z_i}\Big] g_b, \tag{31}$$

where $\overline{wc_1}$ and $\overline{wc_0}$ are the scalar fluxes at the PBL top and at the surface, respectively; and g_t and g_b are the dimensionless mean gradients for top-down and bottom-up components, and are *assumed* to be universal functions that depend only on z/z_i. In a quasi-steady state, the total flux is linear with height, so its top-down and bottom-up component fluxes are also linear with height, i.e., $\overline{wc_t} = \overline{wc_1} z/z_i$ and $\overline{wc_b} = \overline{wc_0}(1 - z/z_i)$.

Applying this decomposition to their LES data, Wyngaard and Brost (1984) and later Moeng and Wyngaard (1984; JAS, 41, 3161–3169) showed that the top-down and bottom-up gradient functions are *NOT symmetric* about the mid-PBL for the buoyancy-driven PBL, as illustrated in Fig. 3.15b, which is different from those of a shear-driven PBL shown in Fig. 3.15a. For a shear-driven PBL where the w-skewness is nearly zero, these two functions are rather symmetric about the mid-PBL. Thus, if we use eddy diffusivity to express the top-down and bottom-up fluxes as $\overline{wc_t} = -K_t \partial C_t/\partial z$ and $\overline{wc_b} = -K_b \partial C_b/\partial z$, since $\overline{wc_t}$ and $\overline{wc_b}$ are symmetric about the mid-PBL, K_t and K_b can be very different, as shown in Fig.
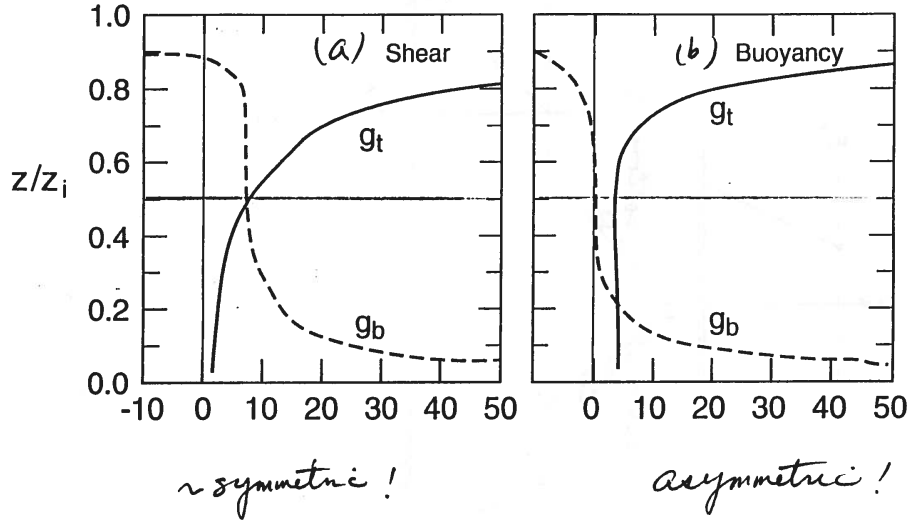
47

Figure 3.15 (SOURCE: Moeng and Wyngaard 1984)

3.16b. [Again, for comparison, I have also plotted K_t and K_b in a shear-driven PBL in Fig. 3.16a.] This implies that within the same CBL, any two scalars that have different surface and entrainment fluxes can have different eddy diffusivities, even though their background turbulent motions are the same.

Using the top-down and bottom-up decomposition, eddy diffusivity K_c for any scalar c can be generalized (see Holtslag and Moeng 1991 for derivation). The generalized form of K_c depends on the ratio of entrainment-to-surface-fluxes, $\overline{wc}_1/\overline{wc}_0$, which can vary among scalars, e.g., ozone and moisture.

3.5.3   Dispersion property

Another unique feature of the CBL is the dispersion property. Figure 3.17 shows this property from Willis and Deardorff's convective tank experiments (1976, QJRMS, 102, 427–445; 1978, Atmos. Environ, 12, 1305–1312; 1981, Atmos. Environ., 15, 109–117) where particles were released from three different heights ($0.07z_i$, $0.24z_i$, and $0.49z_i$) into the convective turbulent layer with a depth z_i. They showed that for the near-surface release the plume centerline (the maximum crosswind-integrated concentration) rise shortly after release, but for the more elevated sources (such as very tall chimneys) the centerline descends first until it intercepts the ground at some distance downstream before it rises. This peculiar feature of elevated
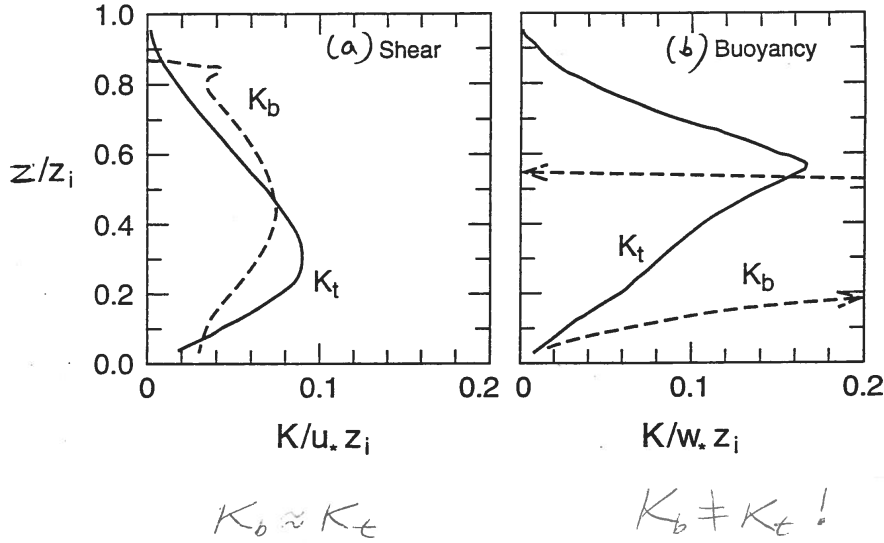
Figure 3.16 (SOURCE: Moeng and Wyngaard 1984)

release in the CBL was also found from an early LES study (Fig. 3.18) by Lamb (1978, Atmos. Environ., 12, 1297–1304) at about the same time as the tank experiment (notice the publication year and page numbers compared to Willis and Deardorff's 1978 paper).

The descent of the elevated plume maximum is due to the greater areal coverage of downdrafts, as a result of positively skewed vertical velocity field. As we showed in section 3.1, on average, updrafts are stronger than downdrafts in the CBL and hence the area covered by updrafts is smaller than that by downdrafts. Therefore, particles released from an elevated source have a greater probability to get into downdrafts than updrafts. Thus more particles are transported downward than upward. This finding has an important implication for air pollution modeling; *i.e.*, the prediction of the location and magnitude of the maximum concentration measured near the surface downstream from emissions depends strongly on the w-skewness of the turbulent field. It provided the basis for the revision of short-range dispersion models in the 1980s (see Turbulent Diffusion Article 441, Encyclopedia of Atmospheric Sciences, 2001, eds. by J. Holton, J. Pyle, and J. Curry, Academic Press).
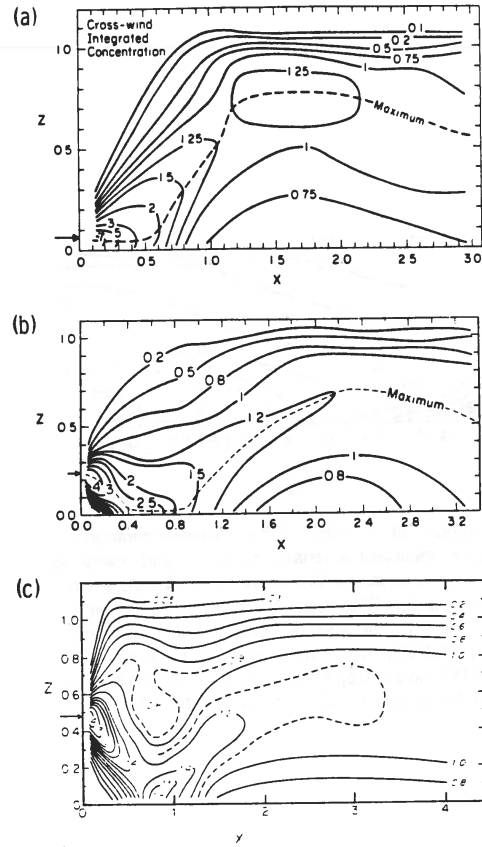
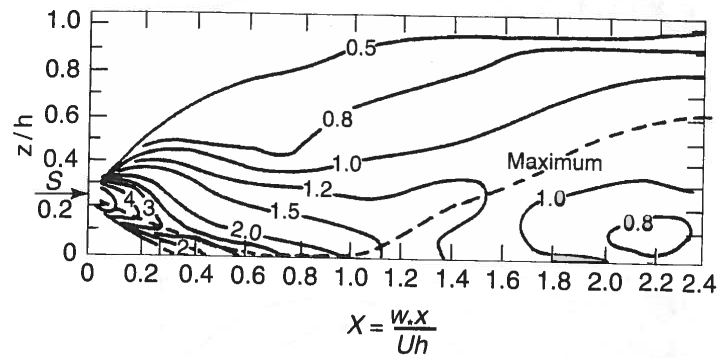Figure 3.17 (SOURCE: Willis and Deardorff 1976)

Figure 3.18 (SOURCE: Lamb 1978)

4 THE NEUTRAL AND STABLE PBLs

4.1 The neutral PBL

The neutral PBL is defined when the surface buoyancy flux is exactly zero (i.e., no buoyancy forcing for turbulence). This condition rarely occurs outdoors particularly over land. After sunset, the ground becomes colder than the air above it, the surface buoyancy flux becomes negative and the PBL becomes "stable". (Note: The definition of stable or unstable clear PBL is determined by the sign of the surface buoyancy flux, not by the potential temperature gradient within the PBL. A well mixed layer where $\partial \Theta / \partial z \sim 0$ is usually NOT a neutral PBL because such a well-mixed layer is likely to be maintained by strong surface heating.) During the transition from unstable to stable PBL (late afternoon over land) or vice versa (early morning over land), there may be an instant when the surface heat flux becomes exactly zero, but that period never lasts long enough to reach a quasi-steady neutral PBL.

This PBL regime is more likely to occur over the ocean (i.e., *marine boundary layer*), where the air-sea temperature difference is often small. The *oceanic mixed layer* (the thin turbulent layer BELOW the ocean surface) is mostly driven by surface wind stress, and hence its statistical behavior is often similar to the neutral PBL. (Note: Oceanographers like to use the term 'oceanic mixed layer'. It doesn't mean that the oceanic boundary layer turbulence is buoyancy-driven like the CBL in the atmosphere. Surface wind stress is still the dominant source for turbulence in most oceanic mixed layers.)

The structure and statistics of the neutral PBL is briefly summarized below. The neutral PBL is a pure shear-driven turbulent layer and has been studied mostly by the engineering community, in wind tunnels (e.g., Robinson, 1991, Ann. Rev. Fluid Mech, 23, 601–639) and numerical simulations (e.g., Moin and Kim, 1982, JFM, 118, 341–377). It was also examined by many PBL-LES groups (e.g., Andren et al. 1994, QJRMS, 120, 1457–1484). A distinct flow pattern of shear-driven turbulence is persistent streaky structures near the wall, roughly along the mean wind direction. In the TKE budget, the shear production nearly balances the molecular dissipation; the turbulent and pressure transport terms are negligibly small. The mean wind is not well mixed with height as the CBL; rather, it turns with height as described by the classical *Ekman Spiral* (Fig. 4.1; from Stull's textbook). The statistics can
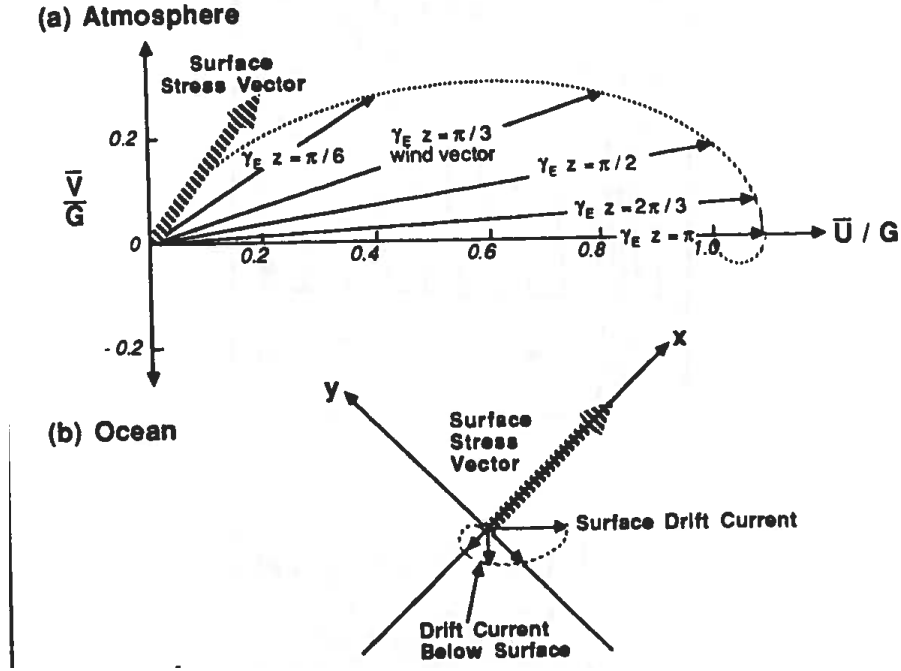
Figure 4.1 (SOURCE: Stull's textbook)

be scaled with surface friction velocity u_* and the PBL depth z_i. The largest component of velocity variances is along the mean wind (i.e., streamwise component). The maxima of $\overline{u^2}/u_*^2$, $\overline{v^2}/u_*^2$, and $\overline{w^2}/u_*^2$ occur near the wall with a magnitude of about 5-8, 3, and 1-2, respectively.

4.2   The weakly stable PBL

After sunset, the surface buoyancy forcing for turbulence disappears and the turbulence within the CBL quickly dissipates. Only wind shear can maintain the turbulence. Unlike buoyancy-driven turbulence, shear-driven turbulence is weaker, its transport is more local, and hence produces a shallower PBL. A typical stable PBL height is a few hundred meters or less. Thus, the PBL top drops abruptly after sunset. The previous mixed layer, however, remains up there although it is no longer a turbulent layer. This is called the *residual layer*. The pollutant that was transported up into the residual layer from previous CBL remains in that layer until large-scale motion advects it away.

The stable PBL is associated with a downward buoyancy flux at the surface. Buoyancy now works against the mean shear in suppressing turbulence. Turbulence can be maintained
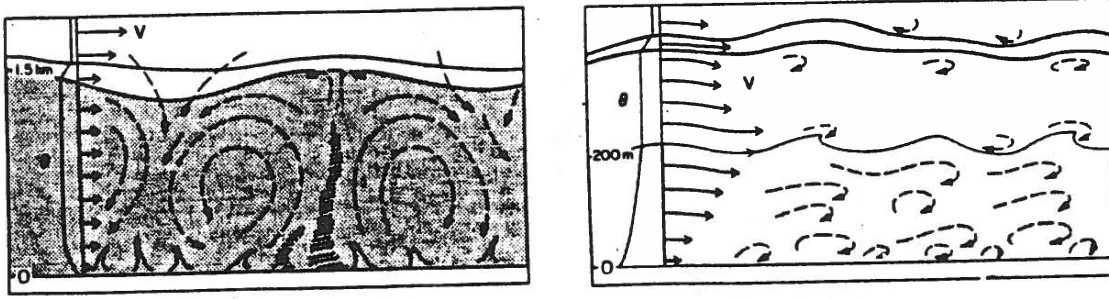
Figure 4.2 (SOURCE: Wyngaard 1992)

only when shear production is larger than buoyancy consumption. In the *weakly stable PBL* turbulence is maintained and remains continuous in space and time by wind shear. This situation happens when the wind is strong or the surface buoyancy flux is only slightly negative.

Because only largest eddies are directly influenced by the sign change of buoyancy, it is the large eddies that are directly suppressed by the negative buoyancy. Also, it is the vertical component of the flow field, w', that is directly suppressed by negative buoyancy. Thus, energy-containing eddies are squashed by stratification; their vertical-to-horizontal size ratio is about 0.1 in strong stratification and about 0.5 in weak stratification. A sketch (Fig. 4.2) by Wyngaard (1992; Annu, Rev. Fluid Mech., 24, 205–233) shows how large eddies that exist in the CBL are suppressed in the stable PBL.

Observational studies have demonstrated some success in generalizing the structure of the weakly stable PBL. The most successful method of generalization is *local similarity scaling* proposed by Nieuwstadt (1984; JAS, 41, 2202–2216), in which the statistics are scaled by the local momentum and heat fluxes $\tau(z) = [\overline{uw}(z)^2 + \overline{vw}(z)^2]^{1/2}$ and $\overline{w\theta}(z)$, rather than by the surface fluxes u_*^2 and $\overline{w\theta}_0$. According to this local scaling law, the normalized standard deviations of velocity and temperature are all constant, i.e., $\sigma_u/\tau^{1/2} \propto \sigma_v/\tau^{1/2} \propto \sigma_w/\tau^{1/2} \propto$ constant and $\sigma_\theta/[-\overline{w\theta}/|\tau|^{1/2}] \propto$ constant. For example, Fig. 4.3 (from Nieuwstadt 1984) shows that all data points lie around the $\sigma_w/\tau^{1/2} \sim 1.4$ curve, independent of the stability factor z/Λ, where $\Lambda \equiv -\frac{\tau^{3/2}}{k(g/T_0)\overline{w\theta}}$ is a local Monin-Obukhov length. Observations also show that $\sigma_\theta/[-\overline{w\theta}/|\tau|^{1/2}] \sim 3$.

To apply the local scaling law one needs to know the profiles of the heat and momentum
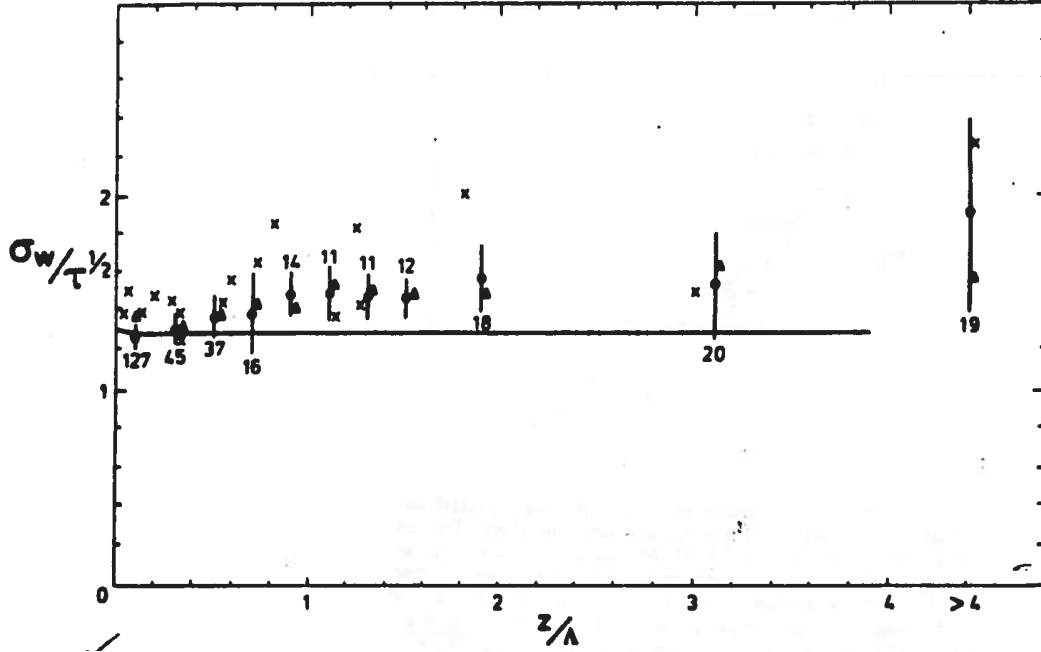
Figure 4.3 (SOURCE: Nieuwstadt 1984)

fluxes first. Some observations (e.g., Nieuwstadt, 1984) found that the heat flux within weakly stable PBLs is nearly linear with height, as shown in Fig. 4.4; i.e.,

$$\overline{w\theta}/\overline{w\theta}_0 \sim 1 - z/h, \tag{32}$$

which is consistent with the quasi-steady state condition for a conserved variable with no heat source or sink like radiation. But many other field studies found the heat flux is slightly curved (e.g., Caughey et al. 1979, JAS, 36, 1041–1052; Lenschow et al. 1988; BLM, 42, 95–121; Smedman 1991; JAS, 48, 856–868). The cross symbols in Fig. 4.4 are data from Caughey et al. which clearly show a curved heat flux profile. Figure 4.5 taken from Lenschow et al (1988) also indicates that the heat flux profile is not linear with height. Lenschow et al. (1988) provided the following interpretation: If longwave radiative cooling (in the air) plays a direct role in the heat budget, then

$$\frac{\partial \Theta}{\partial t} = -\frac{\partial \overline{w\theta}}{\partial z} + \left(\frac{\partial \Theta}{\partial t}\right)_{\text{rad}}. \tag{33}$$

Thus, for a quasi-steady state,

$$-\frac{\partial^2 \overline{w\theta}}{\partial z^2} + \frac{\partial}{\partial z}\left(\frac{\partial \Theta}{\partial t}\right)_{\text{rad}} = 0. \tag{34}$$
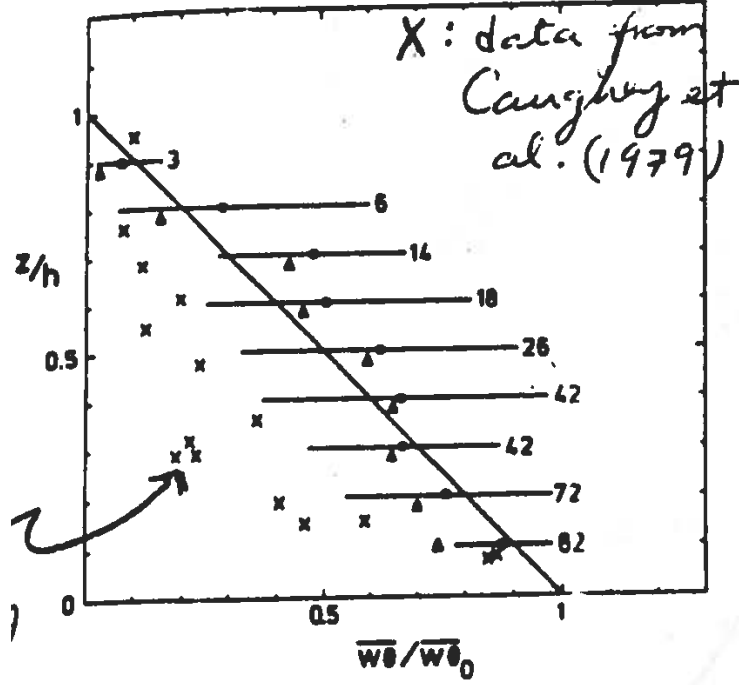
54

Figure 4.4 (SOURCE: Nieuwstadt 1984)

It is apparent that the radiation term in (34) can result in a non-linear heat flux profile, as evidenced from the SESAME data (Fig. 4.5). Lenschow et al (1988) fits the curve as:

$$\overline{w\theta}/\overline{w\theta}_0 \sim (1 - z/h)^{1.5}. \tag{35}$$

To derive the momentum flux profile requires some closure assumptions. Based on his field data, Nieuwstadt (1984) found that the gradient and flux Richardson numbers are nearly constant with height, which is consistent with his local scaling law. In other words,

$$R_i \equiv \frac{g}{T_0} \frac{\partial \Theta/\partial z}{|\partial U/\partial z|^2} = \text{constant} \tag{36}$$

and

$$R_{if} \equiv -\frac{g}{T_0} \frac{\overline{w\theta}}{\overline{uw}\partial U/\partial z} = \text{constant} \tag{37}$$

where U is the streamwise velocity. Nieuwstadt then used (36) and (37) as closures to analytically solve for the mean fields and also the heat and momentum flux profiles. Neglecting the radiative cooling effect in the heat equation, his analytical solution for heat flux is (32) and solution for $\overline{uw}$ is:

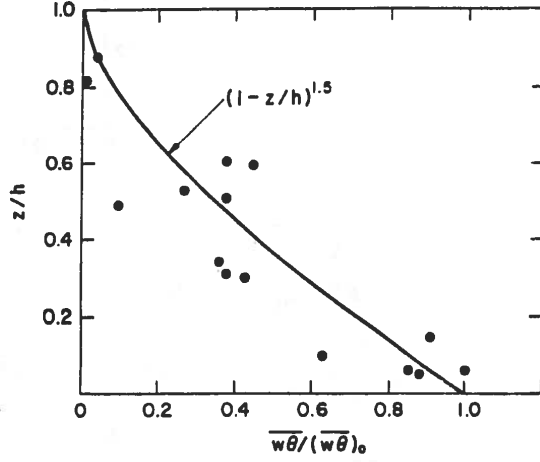$$\frac{\overline{uw}}{u_*^2} = (1 - z/h)^{1.5}. \tag{38}$$

55

Figure 4.5 (SOURCE: Lenschow et al 1988)

Such an analytical prediction is shown to agree well with his observations (Fig. 4.6). Because $\sigma_w/\tau^{1/2} \sim 1.4$, (38) then gives

$$\frac{\sigma_w}{u_*} \sim 1.4(1 - z/h)^{3/4}, \tag{39}$$

or

$$\frac{\sigma_w^2}{u_*^2} \sim 1.96(1 - z/h)^{1.5}. \tag{40}$$

On the other hand, Lenschow et al. (1988) showed that if radiative cooling plays a role in the heat budget and the heat-flux profile (35) is used instead, then the corresponding momentum-flux profile is:

$$\frac{\overline{uw}}{u_*^2} \sim (1 - z/h)^{1.75}, \tag{41}$$

which is supported by SESAME data shown in Fig. 4.7. Using (41), the local similarity law predicts that all velocity variances scaled by the square of surface friction velocity u_*^2 [i.e., $\sigma_w^2/u_*^2 \sim (\sigma_w^2/\tau)(\tau/u_*^2) \propto \tau/u_*^2$] also have the same vertical distribution as $(1 - z/h)^{1.75}$. Again, SESAME data (Fig. 4.8) support this similarity prediction.

For the standard deviation of the temperature variance, the theory predicts $\sigma_\theta/[\overline{w\theta}(z)/\tau(z)^{1/2}] \sim$ constant, hence $\sigma_\theta/\theta_* \propto (\frac{\overline{w\theta}}{u_*\theta_*})/(\frac{\tau^{1/2}}{u_*}) \propto (1 - z/h)^{3/2}/(1 - z/h)^{7/8} \propto (1 - z/h)^{5/8}$, which is a reasonable prediction compared to the field data (Fig. 4.9).

Lenschow et al. (1988) also performed a TKE budget analysis. Figure 4.10 shows that the shear production nearly balances the dissipation, just like the neutral PBL. The analysis
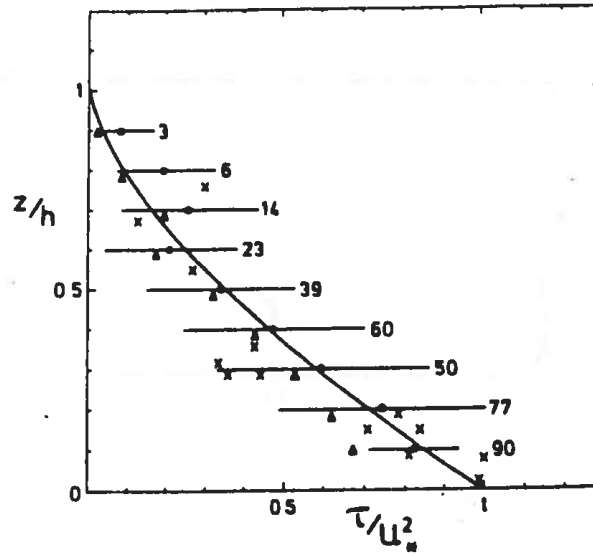
56

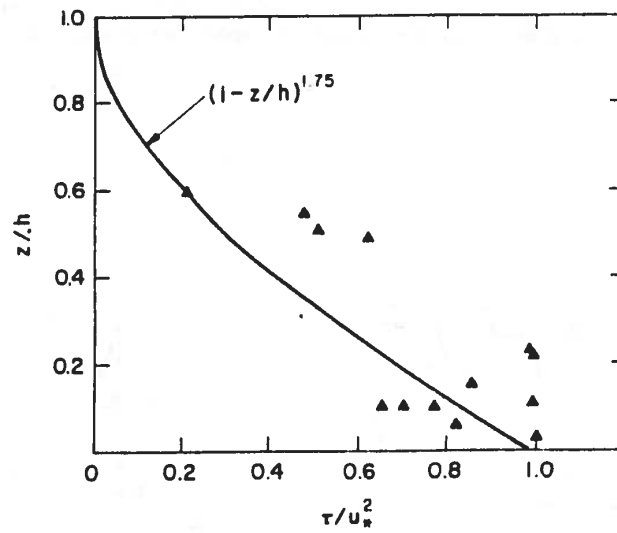Figure 4.6 (SOURCE: Nieuwstadt 1984)

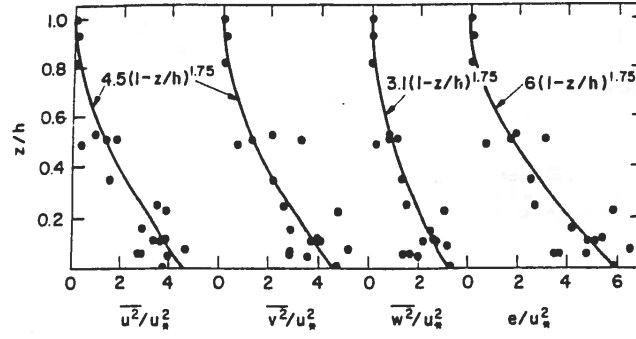
Figure 4.7 (SOURCE: Lenschow et al 1988)
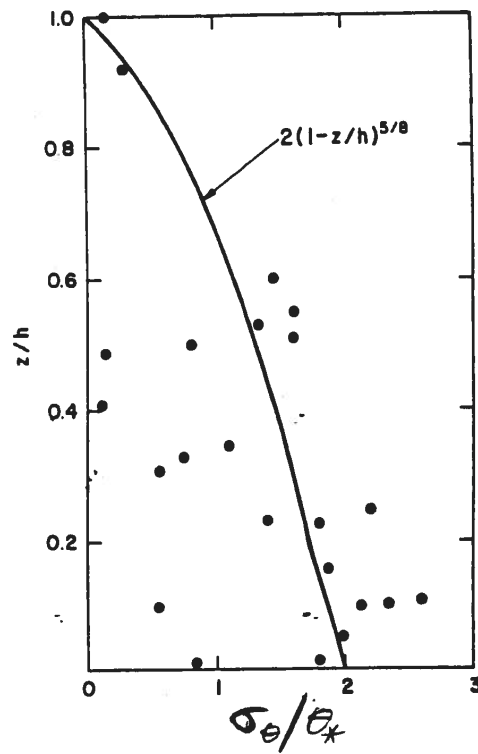
Figure 4.8 (SOURCE: Lenschow et al 1988)

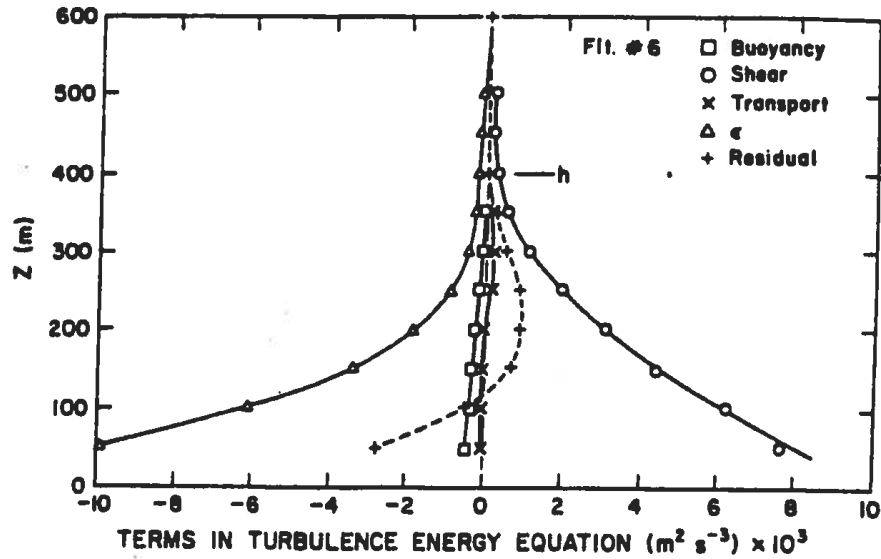Figure 4.9 (SOURCE: Lenschow et al 1988)

Figure 4.10 (SOURCE: Lenschow et al 1988)

indicates that the third-moment turbulence and pressure transport terms within the stable PBL are small, a feature that is similar to the neutral PBL but very different from the CBL. This implies that modeling the weakly stable PBL is easier than modeling the CBL because one can neglect the 3rd-order moment terms which are difficult to estimate.

4.3   The very stable PBL

The *very stable PBL* occurs when the wind at night is calm and/or the ground temperature is very cold. In this PBL regime, turbulence is so weak that it becomes intermittent or sparse, as shown in Fig. 4.11, from Caughey (1982, *Atmospheric Turbulence and Air Pollution Modeling*, edited by F.T.M. Nieuwstadt and H. van Dop, Reidel Publishing Co., page 142). In this case, shear production and buoyancy consumption have about the same magnitude. The ratio of the wind shear and buoyancy forces is called *flux Richardson number* $R_f = \frac{g/T_0 \overline{w\theta_v}}{[\overline{uw}\partial U/\partial z + \overline{vw}\partial V/\partial z]}$. By approximating the fluxes through K-theory (and assuming that eddy viscosity equals eddy diffusivity), this ratio becomes *gradient Richardson number* $R_i = \frac{g/T_0 \partial\Theta/\partial z}{[(\partial U/\partial z)^2 + (\partial V/\partial z)^2]}$. When the buoyancy dominates the shear effect, i.e., when R_f or R_i is larger than a critical number (somewhere between 0.2 and 1), turbulence ceases. Sometimes, turbulence exists locally at different heights where local Richardson number is below
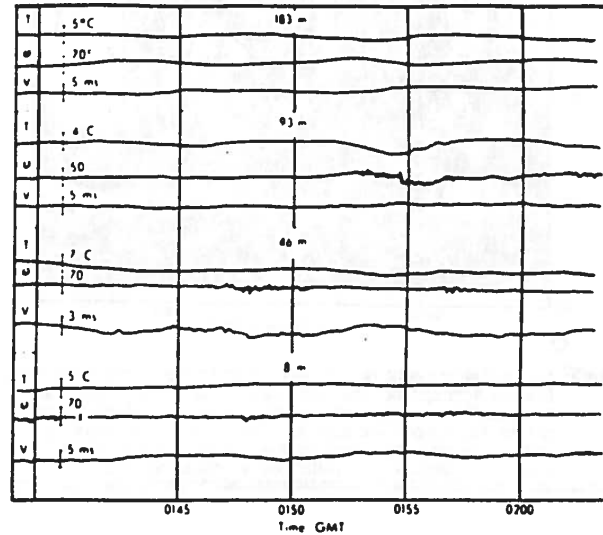
Figure 4.11 (SOURCE: Caughey 1982)

the critical value, shown as the shaded areas in Fig. 4.12 (Andre and Mahrt 1982; JAS, 39, 864–878).

So far, there is no proper theory (including the well-established M-O theory) that can describe the statistics in the very stable PBL. However, the very stable PBL is probably the most important regime for air dispersion. Pollution cannot be diffused or dispersed in a region where turbulence is weak or ceases to exist. This PBL regime is also important for agriculture and military applications, like frost formation. Surface sensible and latent heat fluxes are major budget terms in the time-rate-of-change of ground temperature, and hence may determine the onset of frost on cold nights.

Fortunately, turbulent eddies in this PBL regime are relatively small and they transport/diffuse things more like molecular, downgradient and local. Thus, the eddy diffusivity K approach, which is local and downgradient diffusion, works much better in the stable PBL than in the CBL.

4.4   Physical phenomena in the stable PBL

The following features further complicate the description of the stable PBL, particularly the very stable PBL:
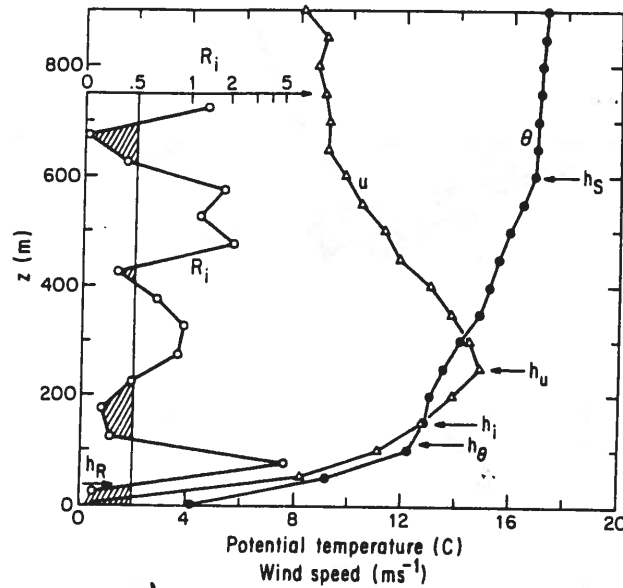
Figure 4.12 (SOURCE: Andre and Mahrt 1982)

(A) *Turbulence often occurs intermittently, and its energy level can be very low to measure or simulate.*

- Negative buoyancy forcing directly reduces the size of the largest turbulent eddies and weakens the turbulent kinetic energy. This makes field measurement more difficult because weaker TKE requires more sensitive instruments.

- Difficulties in analyzing and characterizing the very stable PBL (Mahrt 1985, JAS, 42, 2333-2349) also make it hard to generalize the statistical behavior. Mahrt showed that the observed very stable PBL cases may be too variable to describe.

- It's also difficult to simulate the very stable PBL with the LES technique because sporadic turbulent events are in transition stages between laminar and turbulence. Transition flows are difficult to simulate.

(B) *Gravity waves coexist with turbulent motion.*

There are plenty of gravity waves observed within the stable PBL, as shown in Fig. 4.13, taken from Stull's book (page 527). Gravity waves can be excited locally within a stratified layer by, e.g., turbulent motion. They can also be generated from shear instability aloft (e.g., nocturnal jet) and propagate downward into the stable PBL.

61
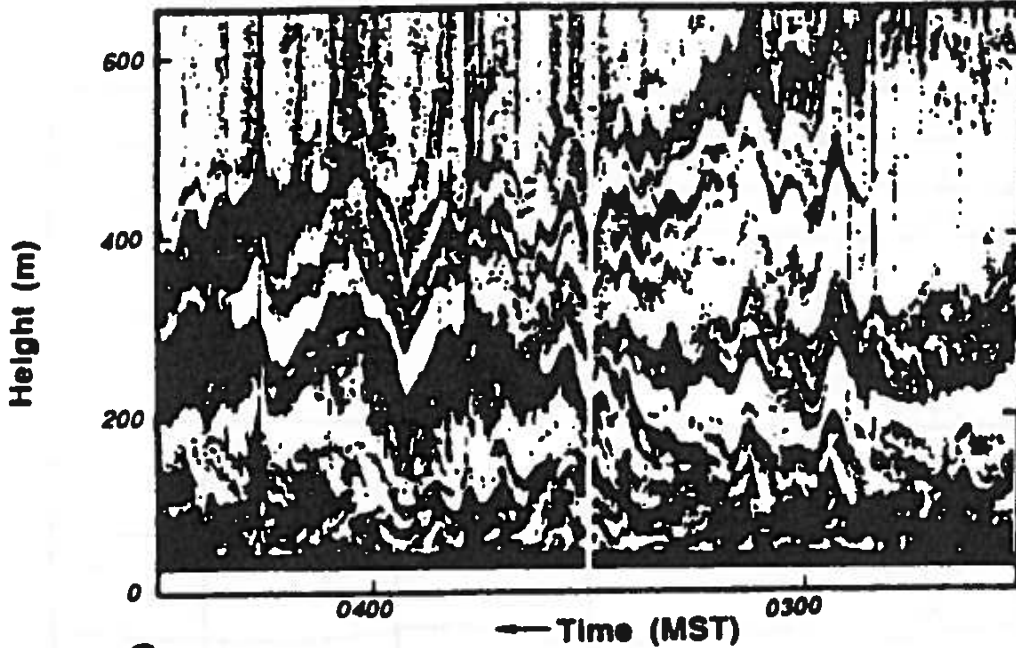
Figure 4.13 (SOURCE: Stull's textbook)

Many researchers have tried to separate gravity waves from turbulent motions, but it is not a trivial task. Gravity waves in the stable PBL can have more than one wavelength; those excited locally have a time period of $2\pi/N$, where $N = (g/T_0 \partial\Theta/\partial z)^{1/2}$ is the Brunt-Vaisala frequency. For a typical stratification within the stable PBL, the period is about 30–300 seconds. This is about the same as the characteristic time scale of turbulent eddies. So, the spectra of gravity waves and turbulent motion often overlap and are difficult to separate.

Gravity waves can interact with turbulence and sometimes break and become turbulence, which further complicates the stable PBL.

(C) *The structure of the stable PBL is very sensitive to sloping terrain.*

With a sloping surface, the gravitational effect modifies not only the vertical wind but also the horizontal wind as,

$$\frac{\partial U}{\partial t} = -\frac{\partial \overline{uw}}{\partial z} + f(V - V_g) + \frac{g}{T_0}\Delta\Theta\sin\alpha, \tag{42}$$

62

Figure 4.14

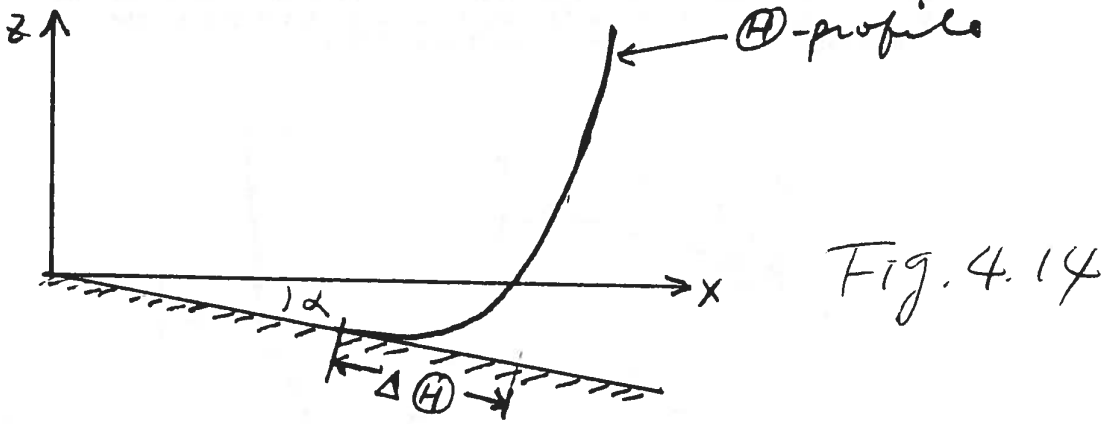where α is the angle of terrain slope and $\Delta\Theta$ is the temperature difference between the surface and the air above (Fig. 4.14).

This buoyancy effect accelerates the horizontal wind downslope, which leads to *drainage wind* or *katabatic flow*. For a typical stable PBL, $\overline{uw} \sim 0.01 \text{m}^2/\text{s}^2$, thus the turbulence term $-\partial\overline{uw}/\partial z$ in (42) is on the order of $u_*^2/h \sim 10^{-4}$ m/s^2, where $h \sim 100$ m is the typical depth of the stable PBL. If $\Delta\Theta \sim 3K$, it would take just a 0.1-degree slope angle to make this downslope acceleration effect as large as the turbulence term.

Since the downslope acceleration term is quite sensitive to the terrain slope, it can be quite different from site to site. Thus to generalize statistics collected from different sites can be difficult.

(D) *Nocturnal jet exists at the top of the stable PBL and it is changing with time.*

Within the stable PBL, the horizontal wind speed has a maximum near the PBL top. This *nocturnal jet* can form due to inertial oscillation acting on a sudden decrease of turbulence after sunset. We can derive this *supergeostrophic wind* from the horizontal mean-wind budget (assuming $V_g = 0$ for simple argument):

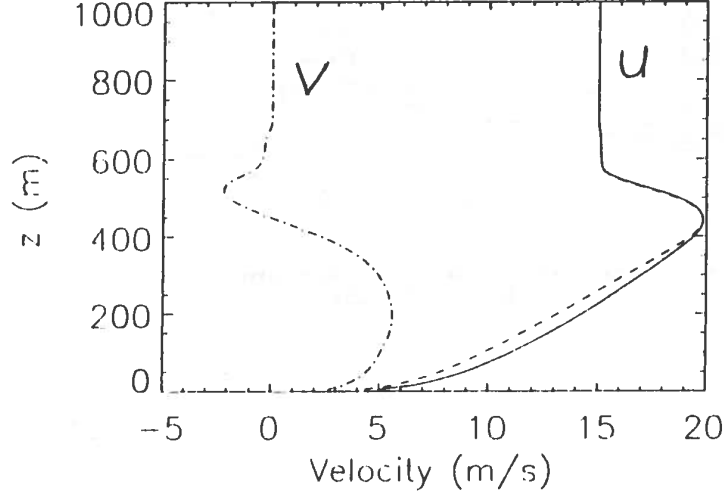$$\frac{\partial U}{\partial t} = -\frac{\partial\overline{uw}}{\partial z} + fV, \tag{43}$$

63

Figure 4.15

$$\frac{\partial V}{\partial t} = -\frac{\partial \overline{vw}}{\partial z} - f(U - U_g). \tag{44}$$

Before sunset, there is a balance (i.e., Ekman balance) among the three major forces: turbulence frictional force, Coriolis force, and pressure gradient force. In other words, the time-rate-of-change terms in (43) and (44) are negligible compared to the other terms within the CBL. Thus, before sunset, $fV \sim u_*^2/z_i$ and $\partial \overline{vw}/\partial z \sim -f(U - U_g)$ in the CBL. After sunset, turbulence decays quickly in the residual layer. Consider the level just above the stable PBL where the previously (before sunset) established turbulent fluxes ($\overline{uw}$ and $\overline{vw}$) suddenly drop to zero. Then, (43) and (44) now become $\frac{\partial U}{\partial t} \sim fV$ and $\frac{\partial V}{\partial t} \sim -f(U - U_g)$ at this level. The time-rate-of-change term in (43) now has to balance the fV term, which is on the order of $u_*^2/z_i \sim 2 \times 10^{-4}$ m/s^2. That means the $U-$wind is accelerated by fV at a rate of ~ 0.7m/s per hour. This acceleration slows down only when the V decreases. That can happen only when the U-wind becomes supergeostrophic, i.e., when $\partial V/\partial t = -f(U - U_g) < 0$. Figure 4.15 shows a nocturnal jet in a stable PBL (though it is taken from an LES, nocturnal jet is often observed in the field).

It is clear from this argument that other meteorological factors that can change the mean-wind budgets in (43) and (44), such as horizontal advection, flow-over-mountains,

and baroclinicity can also modify the nocturnal jet. The evolving nocturnal jet changes the mean wind shear, which in turn changes the properties of turbulence in the stable PBL.

(E) *There may not be a well-defined PBL top.*

Unlike the CBL, which typically has a capping inversion to mark its top, the stable PBL is growing into a neutrally stratified layer, i.e., the pre-existing well-mixed layer (the residual layer). Thus, it is harder to define the stable PBL top. Methods to define the PBL top include a) where the TKE decreases to, say, 5% of its surface value, b) where the magnitude of the momentum flux decreases to, say, 5% of its surface flux, c) where the temperature gradient becomes zero, and d) where the mean wind has a maximum (i.e., where the nocturnal jet is). Different methods may give different answers, an example shown in Fig. 4.12. This makes the scaling of statistics difficult.

(F) *The mean temperature gradient is changing with time due to surface longwave radiation cooling.*

Longwave radiation (IR) cooling produces a surface inversion (i.e., the ground is colder than the air above it), and the surface inversion results in a negative buoyancy flux, and the negative buoyancy flux suppresses turbulence. Therefore, a stronger IR surface cooling leads to a weaker turbulence. Weaker turbulence results in less diffusion of cold air upward into the PBL and this further enhances the surface inversion. Thus, the surface temperature inversion (i.e., the ground-air temperature difference) increases in time at a windless night where turbulent transport is weak and surface longwave cooling dominates.

This feedback mechanism is different from the CBL. In the CBL, the stronger the surface heating, the stronger the turbulence and transport, and hence the smaller the ground-air temperature difference.

Because of drainage flow, surface IR cooling, and evolving nocturnal jet, the vertical gradients of both mean temperature and mean wind in the stable PBL are changing with time. The characteristic time scale of these changes is on the order of a few hours and is SHORTER than the time for turbulence in the *upper* part of the stable PBL to feel the

changes of the surface cooling, which may take several hours. We can show this by using a diffusion argument, i.e., in terms of $K\frac{\partial^2 \Theta}{\partial z^2}$. (Note: As we learned before the K-approach works well for the stable PBL because small eddies which dominate the stable PBL transport like like molecular diffusion, local and downgradient.) The time scale for temperature or moisture to diffuse up to the top of the PBL is on the order of h^2/K_h, where K_h is the eddy diffusivity, which is on the order of 0.3 m^2/s in the stable PBL. For a typical depth of 100 m, the time required to diffuse temperature or moisture from the surface up to 100m is $\sim \frac{(100)^2\text{m}^2}{0.3\text{m}^2/\text{s}} \sim 33333$s $\sim$ 9$\sim$10 hours. Remember that in the CBL it takes only $z_i/w_* \sim 10$ minutes to transport temperature or moisture from the surface to the top of the CBL.

Thus, the statistical profiles in the stable PBL are unlikely to be scaled by the surface-flux scaling (such as u_* and w_*), as it does for the CBL. Individual turbulent eddies within the stable PBL are more in local equilibrium with their local mean condition, and this forms the basis for the local similarity scaling described in section 4.2.

5 BOUNDARY-LAYER CLOUDS

We often classify cloudy PBLs into two regimes: the *stratocumulus-topped PBL* (STBL) and the *shallow cumulus PBL*. The STBL consists of a nearly uniform stratocumulus layer which exists inside the well mixed layer, while cumulus cloud occurs above the mixed layer. In other words, the lifting condensation level (LCL) is below the top of the mixed layer in the STBL, while it is above the mixed layer in the shallow cumulus PBL. But that doesn't mean there is no turbulence in the cumulus cloud layer; scattered cumulus clouds are randomly distributed in space and time, behaving just like large turbulent eddies (or thermals) inside the CBL. However, the air in between clouds is either laminar or at the dissipating stage of a previous turbulent cloud.

Both cloud regimes are observed over the subtropical oceans west of major continents and they are more persistent during the Northern Hemisphere summer (Fig. 5.1a). The STBL regime appears near the coasts, with an extension of several thousands of miles into the subtropical ocean. This cloud regime is associated with large-scale subsidence (high pressure system), cold sea surface temperature, and a strong capping inversion. The strong capping inversion, a temperature jump of more than 10 degrees over a very thin layer of just several tens of meters, is resulted from the persistent large-scale subsidence, which adiabatically warms the lower troposphere above the STBL. With such strong capping inversion the STBL is usually shallow (400m–800m) and the cloud top is rather flat (Fig. 5.1b). Further downstream where the sea surface temperature becomes warmer and the inversion weaker, the STBL gives way to scatter shallow cumulus. The transition between the two cloud regimes is important for the Earth's radiation budget due to the abrupt change in cloud cover.

These boundary-layer cloud regimes also occur over cold-air outbreak regions: Great Lakes (Lenschow 1973; JAS, 568–581) or South China Sea (Agee and Hart 1990). But the cold-air-outbreak clouds are strongly affected by large surface heating and also by horizontal advection and wind shear, which differ from the subtropical marine PBL clouds. STBL also occurs over the North Sea (e.g., Nicholls and his colleagues, 1989, QJRMS, 115, 487-511) and summer Arctic Basin (see a summary of STBL by Randall et al 1998, BAMS, 79, 197-219). An unique feature of the Arctic stratus cloud is its multiple cloud layering structure and mixed-phase (water and ice) microphysics, which makes it difficult to study. In this notes, I

will focus only on the subtropical marine cloud types.

5.1 *Stratocumulus clouds*

Stratocumulus-topped PBL (STBL) turbulence is mainly buoyancy driven, by longwave radiation cooling at the cloud top. [Some STBLs were found to be mainly shear driven (Brost et al. 1982; JAS, 39, 800–836), but they are rare.] The stratocumulus-topped PBL is much more complicated than the clear convective PBL (CBL), even though both are buoyantly driven. First, there are many more physical processes involved in the STBL, as shown in Fig. 5.2.

The major complication comes from the fact that the buoyancy source for turbulence locates where entrainment takes place. Downdrafts that are cooled by cloud-top radiation are modified by entrainment before they travel downward and begin to buoyantly drive turbulence. Just how entrainment affects this turbulence-generation process is poorly understood because very little is known about the entrainment process itself.

Mathematically, there are more thermodynamic variables to deal with in the STBL. The buoyancy-related quantities, which are needed in, say, the TKE budget, are no longer conserved thermodynamic variables. Their fluxes need to be related to the fluxes of the conserved variables like liquid potential temperature, θ_l, and total water mixing ratio, q_T. These relationships are different in cloudy and clear regions, and are difficult to determine in partly cloudy regions as discussed by Randall (1987; JAS, 44, 850–858). Commonly-used definitions or relationships among the thermodynamic variables are (in linearlized forms):

$$\theta_v \sim \theta(1 + 0.609q_v - q_l) \sim \theta + 0.609\theta_0 q_v - \theta_0 q_l, \tag{45}$$

$$\theta_e \sim \theta + \frac{L}{c_p}q_v, \tag{46}$$

$$\theta_l \sim \theta - \frac{L}{c_p}q_l, \tag{47}$$

where q_v and q_l are water vapor and liquid water mixing ratios. θ_v is the virtual potential temperature (a buoyancy measurement) while θ_e and θ_l are (approximately) conserved variables in the moist adiabatic process.

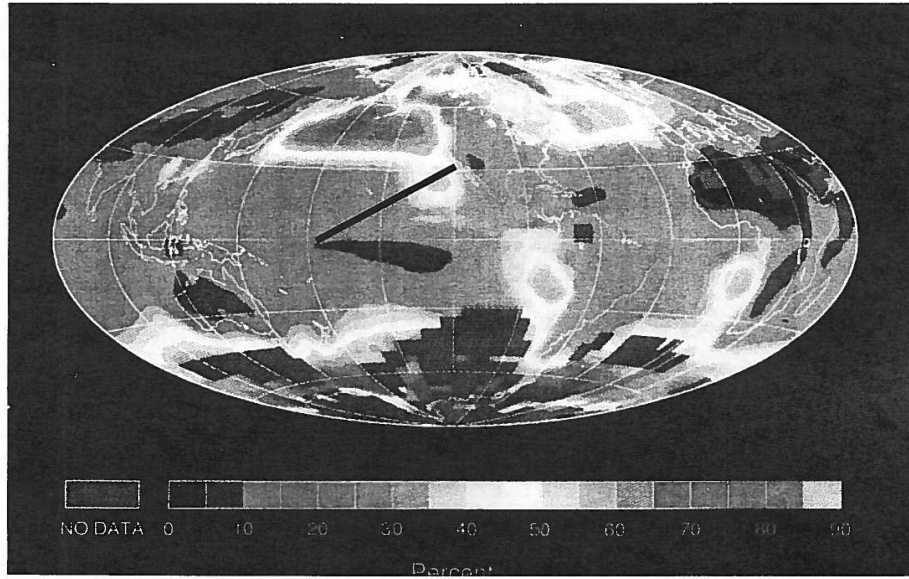NO DATA 0 10 20 30 40 50 60 70 80 90

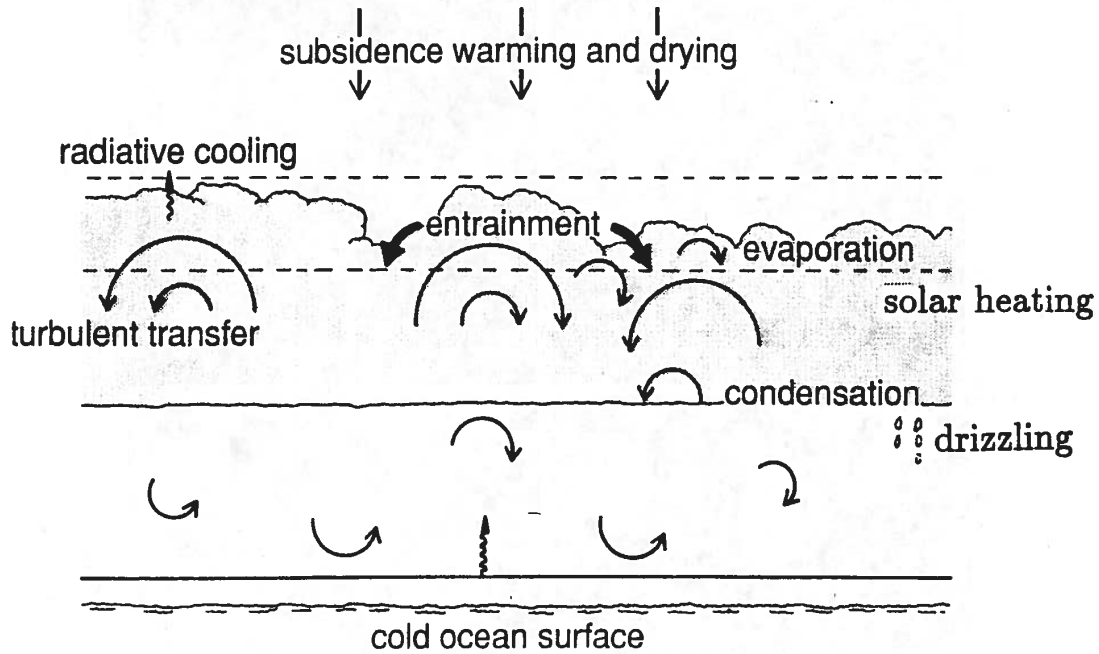Percent

Figure 5.1a

Figure 5.1b

69

Figure 5.2

In the following, I will describe physical processes and observed phenomena within the STBL, discuss some possible mechanisms that dissipate clouds, and show some typical statistical profiles.

5.1.1 Physical processes

The most fundamental physical processes are longwave radiation, turbulence, entrainment, and condensation/evaporation. They exist in all stratocumulus-topped PBLs. In addition, solar radiation can play some role in the daytime, and drizzle is often observed and may also be important in maintaining/dissipating the cloud layer.

- *Longwave radiation cooling at the cloud top*

    Longwave radiation cooling at cloud top exists due to the different radiative properties of water vapor and droplets. In the longwave radiation spectrum, there is a "window region" where water vapor cannot absorb or emit. But liquid water can absorb or emit at all longwave frequencies. Thus, the downward longwave flux above the cloud
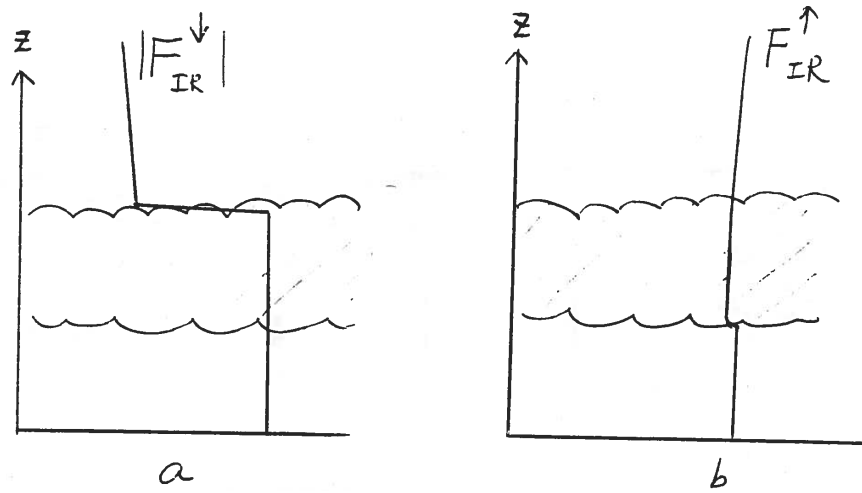
Figure 5.3

top, which comes from the water-vapor line emission of the overlying water vapor, is smaller than the flux within the cloud layer, which comes from the black-body emission of droplets, as shown in Fig. 5.3a. As a result, the magnitude of the downward flux sharply decreases upward across the cloud top. The upward flux, however, remains quite uniform with height, as shown in Fig. 5.3b, with only a slight change at the cloud base due to the slight difference in temperature at the surface and at the cloud base. The net flux thus has a sharp increase right at the cloud top, and hence strong cooling ($\sim$ several degrees per hour) occurs over a very thin layer ($\sim$ 50m) at the cloud top. (Note that the clear-air longwave radiation cooling is only about 1$\sim$2 degrees per day, which is two orders of magnitude smaller than cloud-top longwave radiative cooling.)
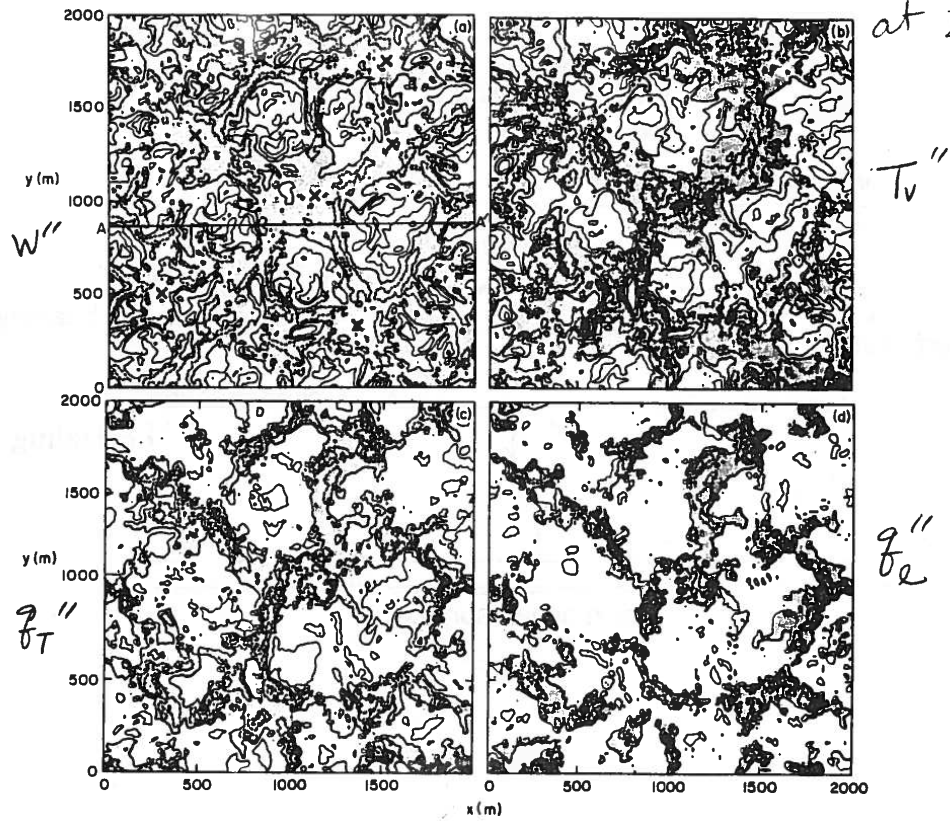
Figure 5.4 (SOURCE: Shen and Moeng 1989)

When a layer is cooled at the top, downdrafts that carry cooled air parcels are negatively buoyant and hence are accelerated downward. These downdrafts drive turbulence just like updrafts that carry the surface-heated air parcels in the clear CBL case. If the cloud top is a rigid lid, then cooling-from-top should generate turbulence exactly the same as heating-from-bottom CBL case. But the cloud top is a free interface that separates turbulent from non-turbulent air and hence entrainment occurs there. Nevertheless, some similar features were observed between the cooling-from-above and heating-from-below PBLs. For example, Nicholls (1989; QJRMS, 115, 487–511) observed cellular patterns near the cloud tops, with broad updrafts in the centers and narrow downdrafts around the edges. Shen and Moeng (1993; BLM, 65, 29–53) also showed irregular cellular patterns near the cloud tops from their large-eddy simulations, as shown in Fig. 5.4.

Turbulent circulations in the cooling-from-top case may not reach all the way to the

Figure 5.5

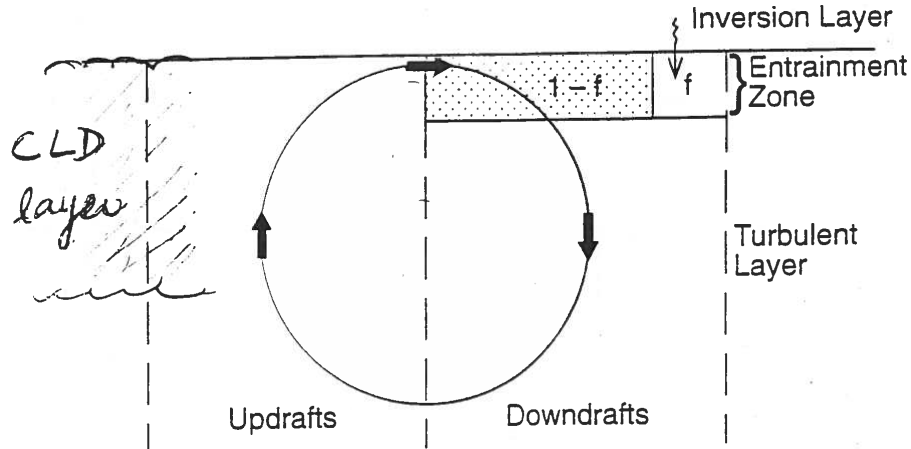surface. For example, in many of Nicholls' North Sea cases, circulations reach only to the cloud base, because of the decoupling phenomenon which we will study in section 5.1.2. [Notice that the cooling-from-above and heating-from-below concept is different from the top-down and bottom-up diffusion concept that we talked about in section 3. Cooling-from-above or heating-from-below provides the buoyancy force that affects turbulence dynamics. Top-down and bottom-up diffusion in principle applies only to passive scalars that cannot change the dynamics; the top-down/bottom-up diffusion occurs within the *same* turbulent flow field.]

- *Entrainment*

  Entrainment brings warm and dry air from above into the turbulent layer, and consequently modifies the near-cloud-top cloudy air parcels that are being cooled radiatively. Thus, before those radiatively cooled air parcels go down and buoyantly "disturb or drive" the flow field, they are modified by entrainment, as sketched in Fig. 5.5. This means that, unlike the CBL, we must know entrainment first in order to know how efficiently cloud-top radiation cooling generates buoyancy and hence turbulence. Because there exists no quantitative understanding of the entrainment processes, modeling the entrainment rate of the STBL remains a problem.

  Our qualitative understanding of entrainment is the following: Entrainment process depends on turbulence intensity, as well as the inversion strength. The stronger the

turbulence, the larger the entrainment rate. The stronger the capping inversion, the harder it takes for inversion air to be entrained. The above description may apply well to clear PBLs, but doesn't give the whole picture in determining the entrainment rate in the STBL. This is because cloud-top radiative cooling and entrainment processes interact strongly: More entrainment brings in more warm inversion air, which reduces the efficiency of longwave cooling in driving turbulence; weaker turbulence then in turn weakens entrainment. This is only true if we neglect the condensation/evaporation effect (e.g., a dust or smoke cloud case). With microphysics, the dry air entrained from above can result in another type of cloud-top cooling due to evaporation, as described below.

- *Condensation/evaporation*

  Condensation/evaporation process further complicates the STBL. Condensation occurs in the cloud layer so there typically exists a sharp increase of the buoyancy flux at the cloud base, as we will see in section 5.1.5. Near the cloud top, entrainment keeps bringing in dry inversion air, and this yields cooling due to evaporation of cloud droplets. When the inversion air is very dry but not very warm, the evaporative cooling effect dominates the entrainment warming effect, then entrainment can result in net cooling of the near cloud-top air. Under this condition, stronger entrainment gives stronger turbulence, which in turn enhances entrainment. This positive feedback is the so-called "cloud-top entrainment instability (CTEI)". We will talk about this instability in more detail in section 5.1.4. Notice that in the above CTEI argument, we have ignored the radiation cooling mechanism.

- *Solar radiation and drizzle*

  Other processes like solar radiation and drizzle can also play important roles in the stratocumulus-topped PBL, although these processes do not exist all the time. For stratocumulus over the ocean, the influence of solar radiation is from the solar absorption inside the cloud layer, rather than from surface heating and surface fluxes. Unlike longwave radiation, solar heating inside the cloud is more uniformly distributed throughout the cloud layer. The part of heating near the cloud top can offset longwave

74

radiation cooling in generating turbulence, while the part throughout the cloud layer directly increases the temperature of the cloudy air. These two effects together can result in a diurnal cycle (which will be mentioned in section 5.1.3) of marine stratocumulus clouds even though the ocean surface temperature remains nearly constant. Furthermore, when the whole cloud layer is warmed by the internal solar heating, the cloud layer may eventually become warmer than the subcloud layer and a thin stably stratified layer may occur at the cloud base. This is one of the mechanisms that is believed to decouple the cloud layer from the influence of the surface. We will talk about decoupling phenomenon next.

5.1.2 Decoupling

Decoupling phenomenon may result from the internal heating of solar radiation in the cloud layer as mentioned above. It can also be due to drizzle. When droplets fall out of the cloud layer, evaporation occurs in the subcloud layer and subsequently cools the subcloud air. When the subcloud air becomes colder than the air in the cloud layer, a thin stably stratified layer may occur somewhere in the subcloud layer, and hence decoupling forms. This drizzle effect has been observed in the field (e.g., Brost et al. 1982, JAS, 39, 818–836; Nicholls 1984, QJRMS, 110, 783–820) and in 1-D closure models (Wang and Wang 1994, JAS, 51, 1559–1576).

Some researchers believe that decoupling is a mechanism that can dissipate clouds. When the cloud layer is decoupled from its underlying surface influence, moisture supply from below is suppressed, and the cloud dissipates. Decoupling phenomenon was first reported by Brost et al. (1982) and Nicholls (1984). Based on aircraft data taken from the North Sea, Nicholls found that the conserved thermodynamic variables, such as equivalent potential temperature or total water mixing ratio, "tend to display small discontinuities near cloud base" and that the observed buoyancy and total water flux profiles show negative values near the cloud base. Nicholls' 1984 paper described many interesting phenomena later observed during FIRE and ASTEX, such as decoupling reported by Betts (1990; Tellus, 42A, 302–304) and drizzle or cumulus cloud forming under the stratiform cloud layer reported by Paluch and Lenschow (1991; JAS, 48, 2141–2158). On the effects of drizzle, Nicholls stated that "The inclusion of precipitation can significantly alter the net transfer of water substance

Stratocumulus ————————→ Cumulus under stratocumulus ————————→ Trade wind cumulus

Cloud layer

Subsidence inversion

Sub cloud layer

Level of decoupling

Surface mixed layer
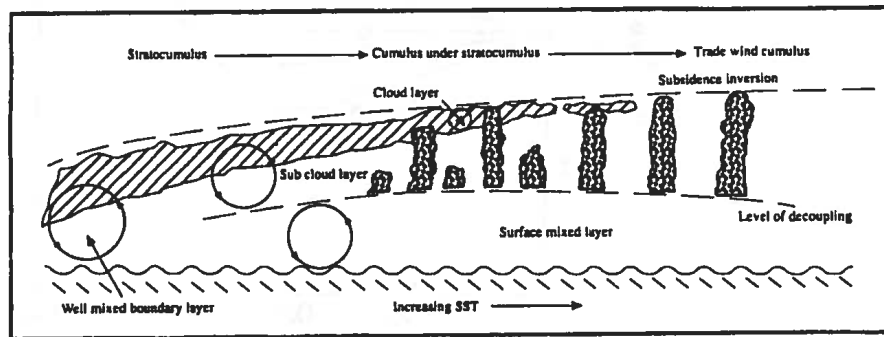
Well mixed boundary layer

Increasing SST ————→

Figure 5.6 (SOURCE: Betts 1990)

and evaporation below cloud can have a significant stabilizing influence on mixing between the cloud and lower layers." On the decoupling phenomenon, he observed that "The cloud and sub-cloud layers are found to be decoupled, i.e., they appear as two separated mixed layers." After decoupling occurs, he found that "If the thermodynamic state of the sub-cloud layer subsequently evolves in a manner which enables condensation to occur within it, the resulting cumulus convection may again link the cloud and surface layers. Cumulus rising into stratocumulus is a very common phenomenon..."

This cumulus-under-stratocumulus phenomenon is illustrated in Fig. 5.6, taken from Betts (1990; Tellus). When stratocumulus cloud is decoupled from the surface influence, cumulus cloud can occur in the lower LCL, beneath the upper LCL where the stratocumulus cloud base is. Since cumulus-under-stratocumulus was a commonly observed phenomenon during the ASTEX field experiment, this phenomenon is believed to be part of the stratus-to-cumulus transition process (e.g., Krueger et al. 1995, JAS, 52, 2839–2850).

5.1.3 Diurnal cycle

Marine stratocumulus cloud undergoes a diurnal cycle even though the underlying ocean surface temperature remains about the same. The diurnal cycle was observed in the 1940's and modeled by Oliver et al. (1978; JAS, 35, 301–316), and it has gained more attention recently. The cloud layer becomes thinner and its liquid water content becomes smaller in the daytime when the sun heats the cloud layer directly. In addition, the solar heating at the cloud top offsets the longwave radiation cooling there, weakens the buoyancy force that drives turbulence, and hence decreases the moisture supply from the surface to the cloud layer. Sometimes the cloud layer may disappear all together during the day, and reforms at night.

The diurnal cycle of stratocumulus over land can be quite different from that over ocean. Over land, the ground can heat up quickly after sunrise due to the part of solar radiation that penetrates through the cloud layer. When the ground heats up, the surface buoyancy flux increases, and the surface sensible heating enhances turbulent transport. If the ground is moist, this enhanced transport can supply more moisture into the cloud layer and therefore helps to maintain the cloud. But if the ground is dry, this enhanced turbulent motion brings warmer air up into the cloud layer, which increases the temperature (and the saturation mixing ratio) of the cloudy air. Thus the change in surface fluxes over land can either thin or dissipate the cloud.

5.1.4 Cloud Top Entrainment Instability (CTEI)

Cloud-Top Entrainment Instability (CTEI) is believed to be a mechanism that breaks up the PBL stratocumulus. This mechanism was first suggested by Lilly in 1968 (QJRMS, 94, 292–309). That classical paper has two very important contributions: It presented the first mixed-layer modeling of the stratocumulus PBL and it is also the first paper proposing CTEI for stratocumulus. I will talk about CTEI next and discuss mixed-layer modeling in section 6.

Lilly (1968) argued that when the air above the cloud layer has a smaller equivalent potential temperature than the cloudy air, i.e., $\Delta\Theta_e = \Theta_e(B^+) - \Theta_e(B^-) < 0$, where B^+ and B^- are levels just above and below the cloud top, then any mixture of air from above

and air inside the cloud will remain colder than the cloudy air. So the mixture can accelerate downward, i.e., becomes negatively buoyant downdrafts, and sink deeper into the cloud layer. This is the so-called CTEI.

Randall (1980; JAS, 37, 125–130) and Deardorff (1980; JAS, 37, 131–147) revised this CTEI criterion by considering the effects of liquid water on the buoyancy. From the virtual potential temperature formula shown in (45), we know that q_l can modify the buoyancy variable θ_v. Based on this definition and other relationships between different thermodynamic variables, Deardorff constructed a buoyancy mixing diagram and used it to demonstrate the CTEI mechanism. Randall, on the other hand, used the flux relationship between buoyancy and conserved variables to demonstrate CTEI. These two different methods ended up with the same conclusion that $\Delta\Theta_e$ has to be much smaller than 0 in order for CTEI to occur.

I will use Randall's derivation for illustration. Assuming that after mixing the mixture becomes saturated, then $q_v = q_*$, where q_* is the saturation mixing ratio. Since $q_*(T,P) \sim q_*(T_0, P) + (\frac{\partial q_*}{\partial T})_p(T - T_0)$, $q_v' \sim (\frac{\partial q_*}{\partial T})\theta' \sim \frac{c_p\gamma}{L}\theta'$, where $\gamma \equiv \frac{L}{c_p}(\frac{\partial q_*}{\partial T})_p$. Using the virtual and equivalent potential temperature formulae given in (45) and (46), we can show that the buoyancy flux can be related to the fluxes of the equivalent potential temperature and total water mixing ratio as

$$\overline{w\theta_v}(B^-) = a\overline{w\theta_e}(B^-) - b\overline{wq_T}(B^-), \tag{48}$$

where a and b are thermodynamic coefficients for saturated air. Using the jump condition, $\overline{w\theta_e}(B^-) = -w_e\Delta\Theta_e$ and $\overline{wq_T}(B^-) = -w_e\Delta Q_T$, where w_e is the entrainment rate, then (48) becomes

$$\overline{w\theta_v}(B^-) = w_e[-a\Delta\Theta_e + b\Delta Q_T]. \tag{49}$$

For the instability to take place, downdrafts ($w' < 0$) have to be negatively buoyant ($\theta_v' < 0$) such that buoyancy flux near the cloud top remains positive, i.e., $\overline{w\theta_v}(B^-) > 0$. Thus, the right-hand side of (49) has to be positive in order for downdrafts to accelerate downward, i.e.,

$$\Delta\Theta_e < \frac{b}{a}\Delta Q_T. \tag{50}$$

The right-hand side of (50) is almost always negative and is about –1 $\sim$ –3K. If we neglect the liquid water term in the θ_v formula (45), the coefficient b in (48) becomes zero and (50) becomes Lilly's criterion.
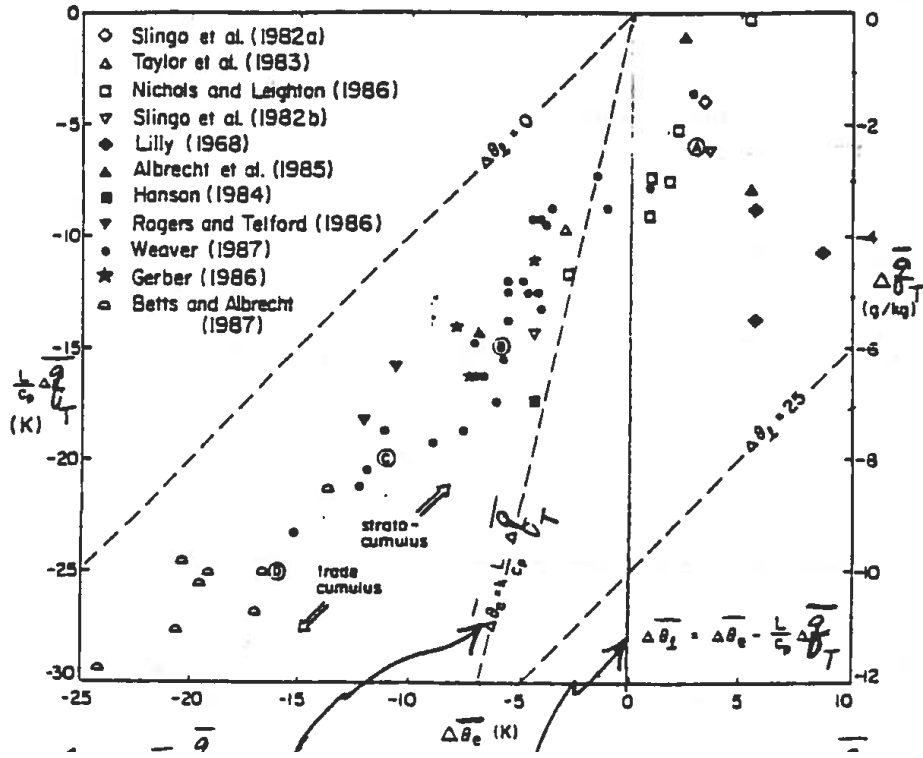
Figure 5.7 (SOURCE: Kuo and Schubert 1988)

The above CTEI criterion was challenged by observations, however, which often found solid stratocumulus cloud deck under conditions that satisfy the instability criterion (50). The most cited evidence is shown Fig. 5.7, taken from Kuo and Schubert (1988; QJRMS, 114, 887–916); it clearly shows that stratocumulus can still exist when $\Delta\Theta_e < 0$ (Lilly's CTEI condition) and $\Delta\Theta_e < \kappa\frac{L}{c_p}\Delta Q_T$ (Randall-Deardorff's CTEI condition). Here $\kappa = (b/a)(c_p/L)$. (However, I would like to remind you that in practice it is difficult to define the jump conditions $\Delta\Theta_e$ and ΔQ_T because in nature there is often no well-defined mixed layer. Also, soundings often show large variations in these thermodynamic fields just above the cloud top.)

Because of the controversy, many studies (e.g., Kuo and Schubert 1988; Siems et al., 1990; QJRMS, 116, 705–739) began to look into more details at the entrainment mixing and evaporation processes involved in the CTEI theory. They used the following thermodynamical analysis to show that not all cloud-top air parcels become saturated after entrainment

79

and mixing. Consider a mixture that consists of χ mass units of warm air that is entrained from above and $(1-\chi)$ mass units of cool moist air within the cloud layer. The equivalent potential temperature and total mixing ratio of the mixture are (ignore the radiation effect):

$$\theta_e = \chi\theta_{ea} + (1 - \chi)\theta_{eb}, \tag{51}$$

$$q_T = \chi q_{Ta} + (1 - \chi)q_{Tb}, \tag{52}$$

where the subscript a represents the above-cloud air and b represents the cloudy air. Using the definitions of θ_e (Eq. 46), θ_v (Eq. 45), and

$$q_l = q_T - q_* \quad \text{when} \quad q_T > q_*, \tag{53}$$

$$q_l = 0 \quad \text{when} \quad q_T < q_*, \tag{54}$$

one can then iteratively solve for θ_v as a function of χ for given θ_{ea}, θ_{eb}, q_{Ta}, and q_{Tb}.

Figure 5.8 shows examples of four different θ_{ea}, θ_{eb}, q_{Ta}, and q_{Tb}, with the y-axis showing the buoyancy difference between the mixture air and its unmixed cloudy environment. These four cases have the jump conditions located at points A, B, C, and D, respectively, in Fig. 5.7. The kinks in these four curves at $\chi = \chi_*$ indicate the amount of mixing fraction for the mixture to become saturated. Mixtures with $\chi < \chi_*$ are saturated and those with $\chi > \chi_*$ are unsaturated.
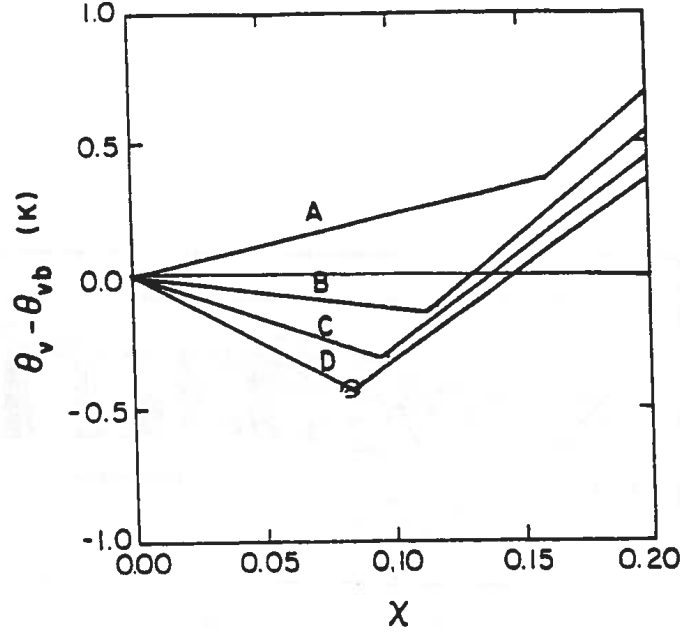
Figure 5.8 (SOURCE: Kuo and Schubert 1988)

Figure 5.8 shows that when the jump condition is on the stable side of the Lilly-Deardorff-Randall curve, such as curve A, all mixtures, with any χ amount, remain warmer than the cloudy (unmixed) environment; none becomes negatively buoyant. When the jump condition satisfies the Lilly-Deardorff-Randall's criterion, curves B, C, and D, some of their mixtures indeed become colder their unmixed cloudy environment, and thus become negatively buoyant (i.e., accelerate downward). However, not all of the mixtures are negatively buoyant; those with larger χ (larger than about 0.15) are still warmer than the unmixed cloudy air. Thus, Kuo and Schubert concluded that the CTEI criterion proposed by Deardorff and Randall is only a necessary, not sufficient, condition for cloud breakup. They also suggested, based on their two-dimensional numerical simulation, that "surface evaporation and upward transport processes can apparently provide enough water vapor to compensate for the evaporative effects associated with the weak evaporative instability".

Siems et al. (1990) provided a similar interpretation by using the *buoyancy reversal* concept; buoyancy reversal is a process that after mixing parcels become denser than either of the unmixed fluids, and cannot return to their original place. Parcels experience buoyancy reversal are those having $\theta_v - \theta_{vb}$ smaller than zero in Fig. 5.8. Siems et al. defined a D

value that is the ratio of $\theta_v - \theta_{vb}$ at χ_* (i.e., the most negatively buoyant mixture) and the buoyancy difference between the two unmixed layers, i.e.,

$$D = \frac{\theta_v(\chi_*) - \theta_{vb}}{\theta_{vb} - \theta_{va}}. \tag{55}$$

Using this definition, Randall-Deardorff's instability criterion is $D > 0$. (Note that the denominator is negative.) Siems et al. argued that the D value has to be much larger than 0 in order for sustained vigorous mixing (i.e., instability) to occur based on Shy and Breidenthal's (1990; JFM, 214, 1–15) laboratory experiments in a convective tank.

The Shy-Breidenthal lab tank consists of two layers of fluids, initially separated by a plate. The lower fluid is denser than the upper one. After a sudden removal of the plate, these two fluids mix *nonlinearly* and produce mixtures that are denser than either of the two initial fluids. This mixing phenomenon is similar to the mixing of clear and cloudy air; after clear air is entrained into the cloud layer, evaporation occurs, and the mixtures can become denser than either of the unmixed clear or cloudy air. The laboratory results showed that when the buoyancy reversal is relatively large, $D > 1.3$, the whole system experiences "explosive entrainment" and becomes unstable, in the sense that "the perturbed interface did not relax back to horizontal, but developed a strong tilt." Because of the explosive entrainment, the depth of the lower fluid, Δh, increases significantly when $D > 1.3$, as shown in Fig. 5.9, taken from Shy and Breidenthal.
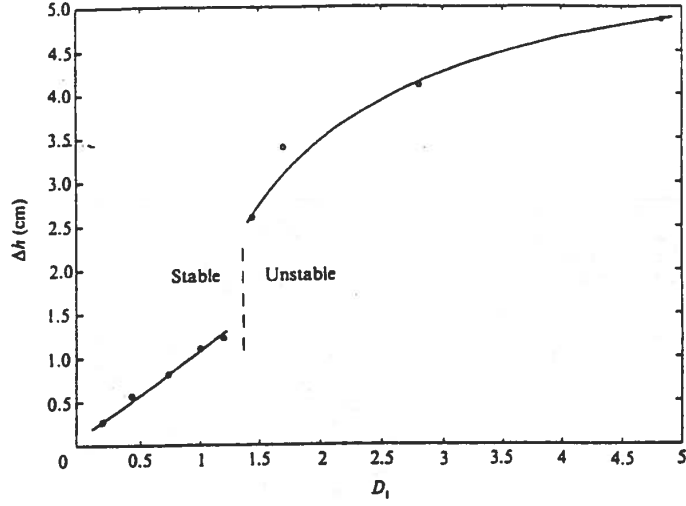
Figure 5.9 (SOURCE: Shy and Breidenthal 1990)

Siems et al. also used a two-dimensional numerical model to simulate the laboratory flow; the numerical results confirmed the laboratory results, as indicated in Fig. 5.10. The entrainment rate of their numerical flows increases significantly only when $D > 1.3$. For applications, Siems et al. concluded that this large D value is unlikely to occur "in the range of hydrodynamic parameters characteristic of mixing at the inversion capping a subtropical stratocumulus cloud layer. Thus it appears unlikely that C(T)EI triggers stratocumulus breakup." However, Siems et al. also recognized the difficulty in defining D or mixing fraction amount from atmospheric sounding, "because neither the boundary layer nor the upper-level environment are perfectly well-defined mixed layers" as is flow in the laboratory or simulations.

Homework 3:

A. Derive (48) and show the expressions for a and b. Also estimate the value of $\kappa = (b/a)(c_p/L)$ for typical values of a and b.

B. Show that if the q_l term in (45) is neglected, then $b = 0$. [Hint: Use the Clausius-Clapeyron equation $T dq_*/dT = Lq_*/RT$, where $c_p \sim 1000$J kg^{-1} K^{-1}, $L \sim 2.45 \times 10^6$ J kg^{-1}, and $R \sim 461$ J kg^{-1} K^{-1}.]

C. Using the definition of θ_v and the equations (51)-(54), plot $\theta_v - \theta_{vb}$ as a function of χ

for θ_{ea}=319.4K, θ_{eb}=316K, q_{Ta}=4.5g/kg, and q_{Tb}=10.5g/kg and show your result in a plot like Fig. 5.8.
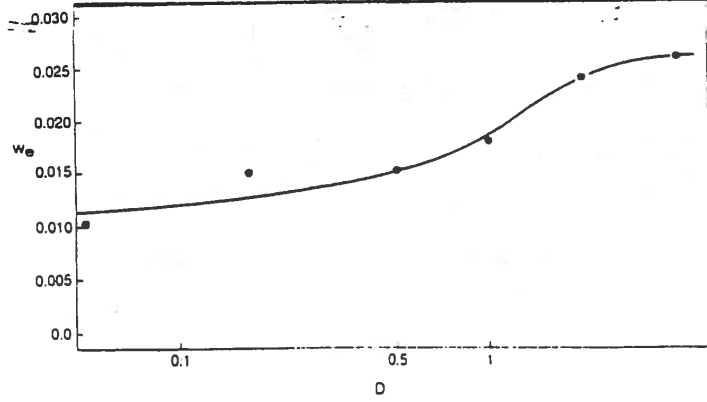

Figure 5.10 (SOURCE: Siems et al. 1990)

5.1.5   Vertical distributions of turbulence statistics

Before I show you some "typical" profiles of statistics in the stratocumulus-topped PBL, let's see which flux profiles should be linear with height in a horizontally homogeneous, quasi-steady state. As in the CBL, we expect the fluxes of conserved thermodynamic quantities to be linear with height under a quasi-steady state. We will use the liquid potential temperature (θ_l) as an example. Total water mixing ratio is also a conserved variable when there is no drizzle. The governing equations for their means are

$$\frac{\partial \Theta_l}{\partial t} = -\frac{\partial \overline{w\theta_l}}{\partial z} - \frac{1}{\rho c_p}\frac{\partial F_{rad}}{\partial z}, \tag{56}$$

and

$$\frac{\partial Q_T}{\partial t} = -\frac{\partial \overline{wq_T}}{\partial z}, \tag{57}$$

where F_{rad} is the radiative flux. Taking the z-derivative of (56) and (57) leads to

$$\frac{\partial(\partial \Theta_l/\partial z)}{\partial t} = -\frac{\partial^2 \overline{w\theta_l}}{\partial z^2} - \frac{1}{\rho c_p}\frac{\partial^2 F_{rad}}{\partial z^2}, \tag{58}$$

and

$$\frac{\partial(\partial Q_T/\partial z)}{\partial t} = -\frac{\partial^2 \overline{wq_T}}{\partial z^2}, \tag{59}$$

84

which should be nearly zero under a quasi-steady state. Therefore the total heat flux, $H \equiv \overline{w\theta_l} + \frac{1}{\rho c_p} F_{rad}$, and the total water flux, $\overline{wq_T}$, should remain linear with height if turbulence reaches a quasi-steady state. Since F_{rad} the longwave radiative flux (or longwave plus solar radiative flux in daytime) is not linear with height, the liquid-potential-temperature flux $\overline{w\theta_l}$ alone is not linear with height either.

When decoupling occurs, turbulence is split to two separate layers and the above argument no longer applies. In this condition turbulent mixing does not extend throughout the whole PBL, H and $\overline{wq_T}$ may have two linear curves representing the two separate mixed layers, as suggested by Nicholls.

Profiles of statistics within the stratocumulus-topped PBL vary from case to case, depending on the type of forcing that generates/consumes turbulence. Statistics are different between buoyancy and shear driven PBLs, and also different between cloud-top-cooling driven and surface-heating driven PBLs.

- *When turbulence is driven mainly by cloud-top radiation cooling*

  This type of STBL has been studied the most, observationally and numerically. Typical structure for this type of STBL was reported by Nicholls (1989; QJRMS, 115, 487–511) based on aircraft data taken over the North Sea over solid and horizontally uniform stratocumulus cases, even though most of these cases were decoupled from the surface. The statistics shown in that paper were plotted only for the upper well-mixed layer, i.e., from the cloud top ($z'/h = 0$) down to the bottom of the upper well-mixed layer ($z'/h = 1$) where the cloud-top radiative cooling effect can reach. Thus h here denotes the depth of the upper well-mixed layer, not the whole PBL depth. Nicholls used the following scaling parameters to normalize the statistics: $w_* = [2.5(g/T_0)h\ B]^{1/3}$, $T_* = 2.5B/w_*$, and $q_{T*} = (\overline{wq_T})_{z_i}/w_*$, where B is the layer-averaged buoyancy flux over the mixed layer h and $(\overline{wq_T})_{z_i}$ is the maximum total water flux near the cloud top.

  Figure 5.11a shows the expected linear trend of the total water flux, although the data are quite scattered. Figure 5.11b shows that the maximum buoyancy flux exists at some distance below the cloud top, i.e., at $z' \sim 0.1h$. At $z'/h = 1$ where the decoupling occurred, the buoyancy flux at that level became negative.
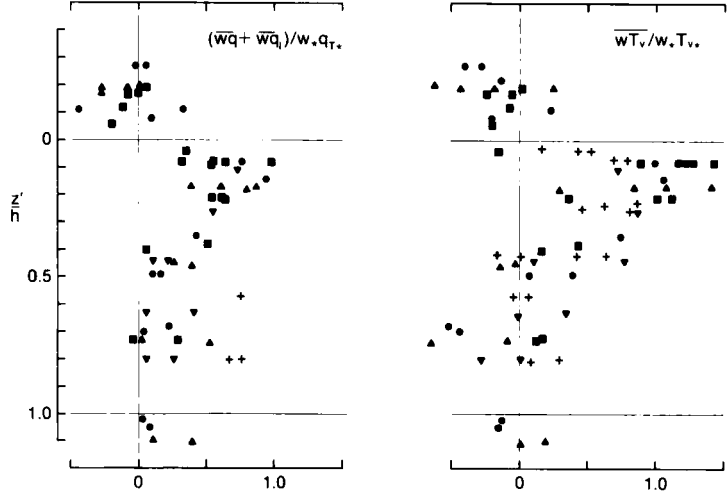
Scaled total water and virtual temperature fluxes $v.$ z'/h. The plotting symbol for each flight is given in Table 1.

Figure 5.11 (SOURCE: Nicholls 1989)

The velocity variances shown in Fig. 5.12 are all on the order magnitude of $0.5w_*^2$ with a peak at about $0.8h$, close to the cloud top.

Nicholls compared his TKE budgets (Fig. 5.13a) with the upside down budgets of a clear CBL (Fig. 5.13b; from Lenschow et al 1980; JAS, 37, 1313-1326) and those of an LES of STBL (Fig. 5.13c; from Moeng 1986; JAS, 43, 2886–2900). From Fig. 5.13a and b, Nicholls concluded that the STBL is similar to the upside down version of surface-heated CBL. Unlike the Nicholls's observed case, the LES shown in Fig. 5.13c does not have the decoupling phenomenon, and hence turbulent mixing takes place throughout the whole PBL. Thus, in Fig. 5.13c $z'/h = 1$ is the Earth's surface, whereas in Fig. 5.13a it is a cloud-base level. Because of this difference we may compare them only above $z = 0.5h$. As pointed out by Nicholls, the overall features between model and observations above $0.5h$ are similar except the turbulence transport term, $T = -\partial \overline{wE}/\partial z$. Near the cloud top, observations show large negative, but LES shows a nearly zero T. Between $0.2h < z' < 0.5h$, T is positive in the observations, but negative in the simulation.

The coarse resolution of the LES was first suspected to be the reason for the discrepancy between the observed and simulated T term. But from a much finer
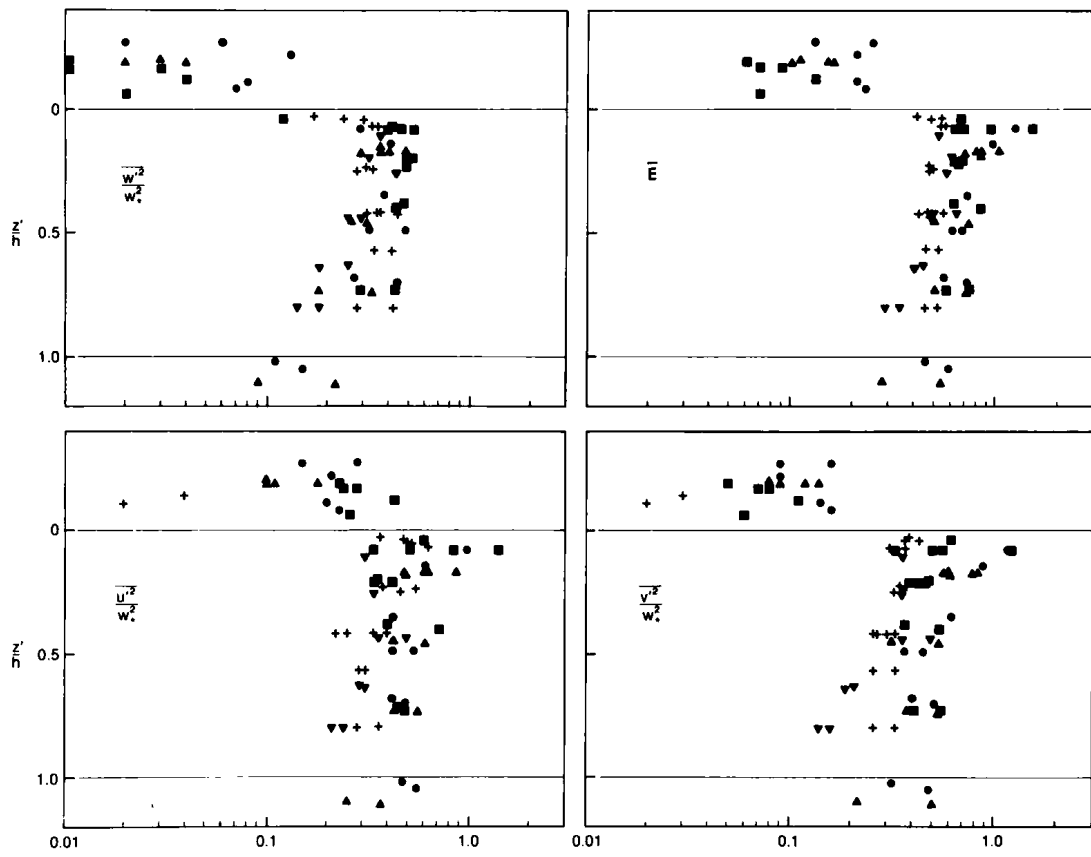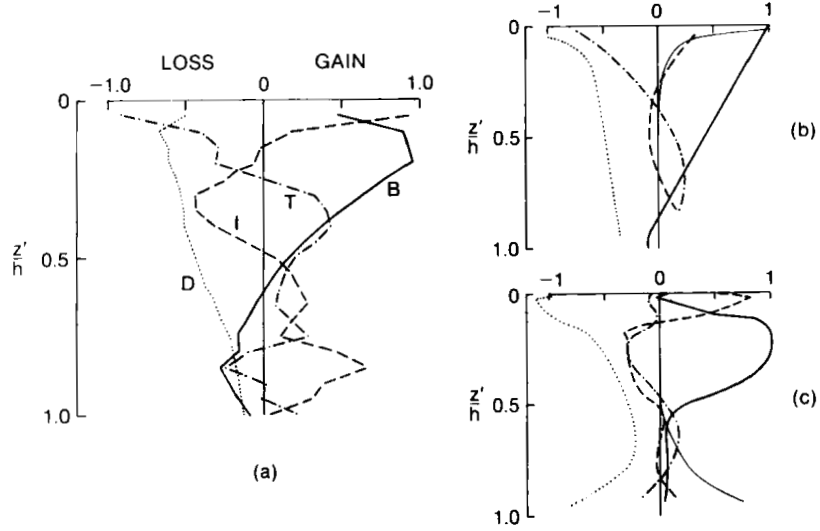
Figure 5.12 (SOURCE: Nicholls 1989)

Figure 17. (a) The composite TKE balance. The terms are described in the text (see Eq. (11)). (b) As (a), but from Lenschow *et al.* (1980) plotted upside down. Here, the thin full line represents S (see Eq. (11)), the shear generation. (c) As (a), but from Moeng (1986). As in (b), the thin full line represents S.

Figure 5.13 (SOURCE: Nicholls 1989)

resolution LES (with $160 \times 160 \times 80$ grid points covering the same domain such that $\Delta x = \Delta y = \Delta z = 12.5m$), Fig. 5.14, we see that the discrepancy in T term is worse; the fine-resolution LES shows that T is clearly positive near the cloud top. (Compared between the two LESs, the fine-resolution LES has a slightly larger surface heating.)

It is clear that the discrepancy in T-term between Nicholls' observations and the LES came from the different distributions of $\overline{w^3}$. The observed $\overline{w^3}$ is negative in the cloud layer and increases to zero at the cloud top: This yields a negative TKE flux $\overline{wE}$ (Fig. 5.15b) throughout the cloud layer for most of the five flight cases. The LES flow, on the other hand, shows a positive $\overline{w^3}$ in the cloud layer, which decreases to zero at the cloud top, and a negative $\overline{w^3}$ in the lower PBL. The $\overline{w^3}$ dominates $\overline{wE}$, which is then positive in the upper and negative in the lower PBL (Fig. 5.15a; results were from the fine-resolution LES).

An explanation for the simulated distribution of $\overline{w^3}$ shown in Fig. 5.15a was given in Moeng and Rotunno (1990; JAS, 47, 1149–1162) based on a direct-numerical-simulation (DNS) study. If there is only surface heating, $\overline{w^3}$ and hence the w-skewness
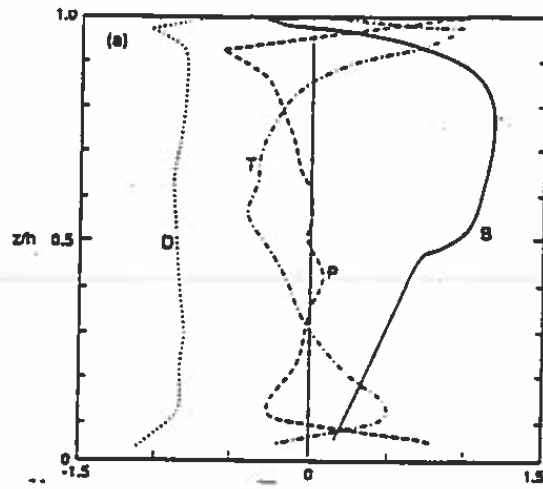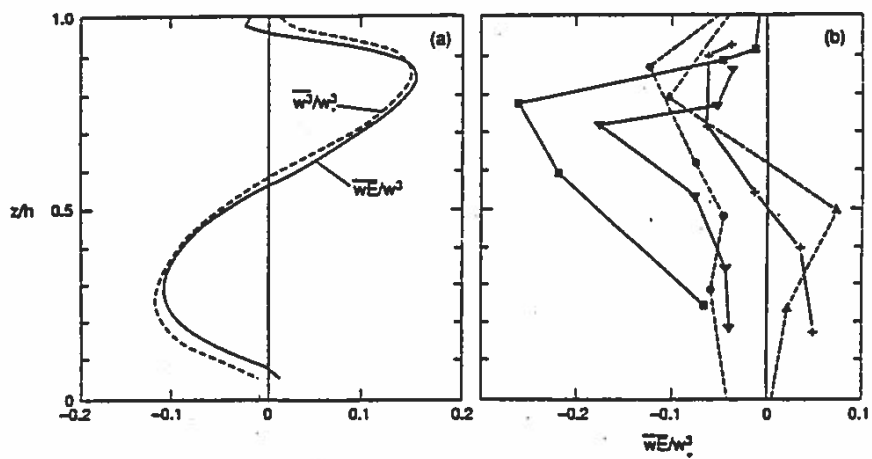
Figure 5.14 (SOURCE: Shen and Moeng 1993)

Figure 5.15 (SOURCE: Shen and Moeng 1993)

$[\equiv \overline{w^3}/(\overline{w^2})^{3/2}]$ are positive throughout the whole PBL (just like in the CBL, Fig. 3.9b) because surface-generated updrafts are stronger than downdrafts. Since only few of these strong updrafts can reach to the cloud top, the area coverage by strong updrafts decreases with height. Thus, the largest positive w skewness is likely to occur near the PBL top. Now consider just the effect of cloud-top cooling. Cloud-top cooling generates strong downdrafts, with a few of them reaching all the way to the surface (but only if there is no decoupling). Hence the most negative skewness is likely to be near the surface. Combining the cloud-top cooling and surface heating effects, positive w-skewness occurs in the upper PBL due to surface heating, and negative w-skewness in the lower layer due to cloud-top cooling, just like what we see in Fig. 5.15a. In the observational cases, however, the upper mixed layer was decoupled from its surface influence, so the only buoyancy source that drives turbulence here was cloud-top cooling. Therefore, throughout the whole mixed layer $\overline{w^3}$ and hence $\overline{wE}$ are negative.

To see if turbulence statistics generated from LES depend sensitively on its numerics, SGS parameterizations, SGS condensation, and/or longwave radiation representations, the GCSS Boundary Layer Cloud Working Group performed its first intercomparison study in 1994. The group got together to discuss their results during the 1994 NCAR/GCSS Boundary Layer Cloud Workshop, and the result is summarized in Moeng et al (1996, BAMS, 77, 261–278). An idealized STBL—horizontally homogeneous, nearly solid cloud deck, no solar heating, no decoupling, no drizzle, plus negligibly amounts of surface heating and wind shear—was chosen to be the first intercomparison case. Ten LES groups participated in this intercomparison study. Although the results vary in magnitude, mainly because the cloud-top radiative cooling amount is different among the LESs as shown later, the vertical distributions of fluxes (Fig. 5.16), velocity variances (Fig. 5.17), and TKE budget (Fig. 5.18 shows the three major terms) calculated from the ten LES codes are quite similar in shape.

Figure 5.18a shows that the magnitudes of the buoyancy production vary among the LESs. Comparing Figs. 5.17a and 5.18a, we see that the LESs that have the largest buoyancy production term (e.g., UW) yield the strongest turbulence intensity.
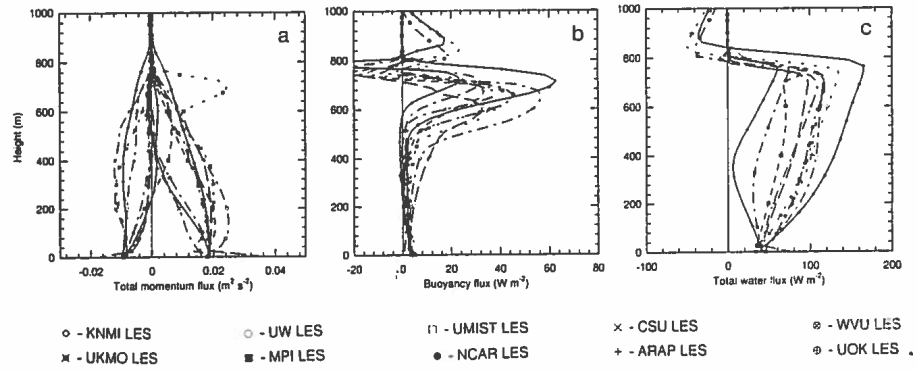
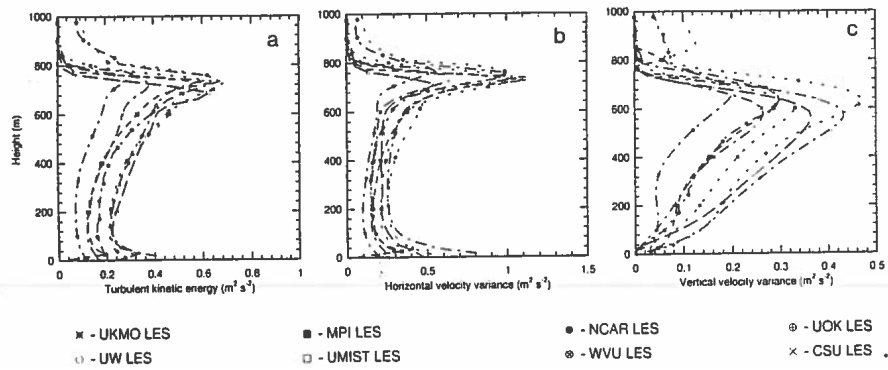Figure 5.16 (SOURCE: Moeng et al 1996)

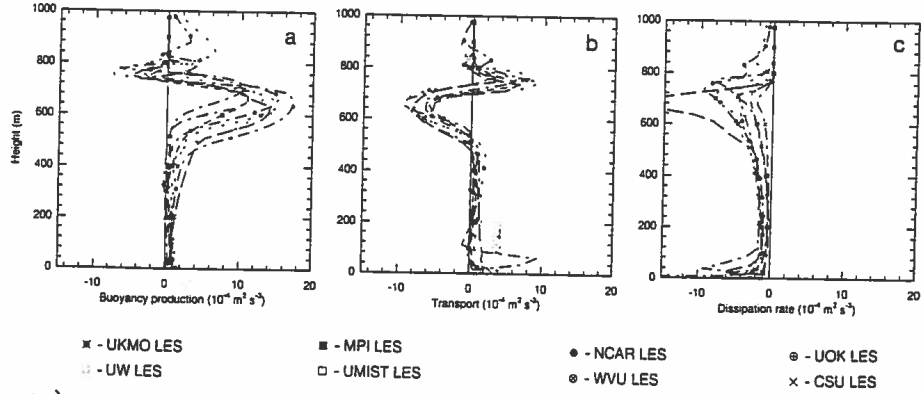Figure 5.17 (SOURCE: Moeng et al 1996)

Figure 5.18 (SOURCE: Moeng et al 1996)

(Note: the UKMO's total TKE is suspiciously large, because both of their horizontal and vertical velocity variances are smaller than those of the UW.) The difference in the buoyancy production term is apparently due to the different amount of cloud-top cooling, which is the main source of buoyancy (and hence turbulence) in this case. The cloud-top cooling rate is an internally determined quantity in LES, calculated from a longwave radiation scheme; different LES codes used different longwave radiation schemes and hence obtained different cloud-top cooling rates (Fig. 5.19). As you can see, the cloud-top cooling rates predicted by the KNMI (diamond-solid line) and UW (open circle-dashed dotted curve) LESs are larger than 4K/hour. Consequently, their buoyancy flux (Fig. 5.16c) and hence the velocity variances (Fig. 5.17; KNMI result is not shown here) are the largest among all LESs.

- *When surface heating also dominates*

  Moyer and Young (1993; JAS, 50, 2759–2771) analyzed ten FIRE flights, and showed that the buoyancy forcing within the STBL ranged from purely surface forcing to purely cloud-top forcing. Figure 5.20, taken from their paper, shows the variation of the surface heat flux during those ten flights, from slightly negative to significantly positive.

- *When wind shear dominates*

  One of the documented STBLs that were driven by shear was reported by Brost et al. (Part I and II 1982; JAS, 39, 800–817 and 818–836). They suggested that the
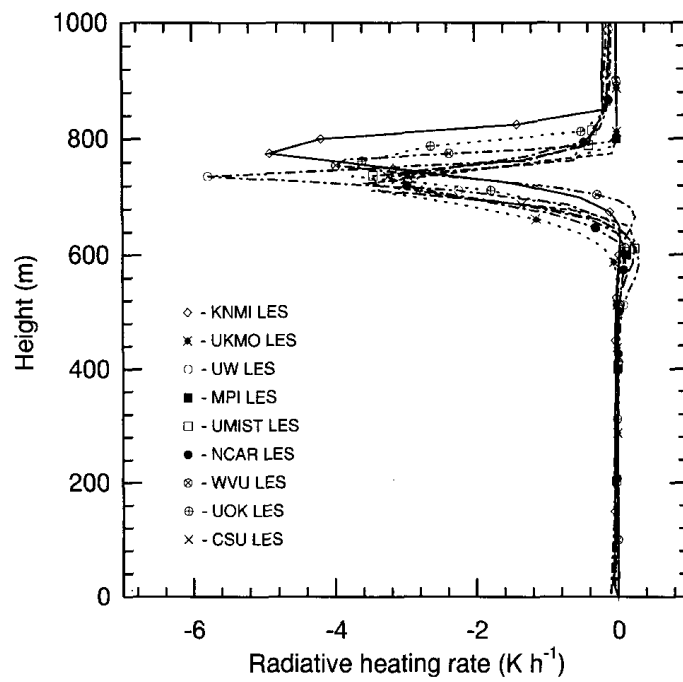
Figure 5.19 (SOURCE: Moeng et al 1996)
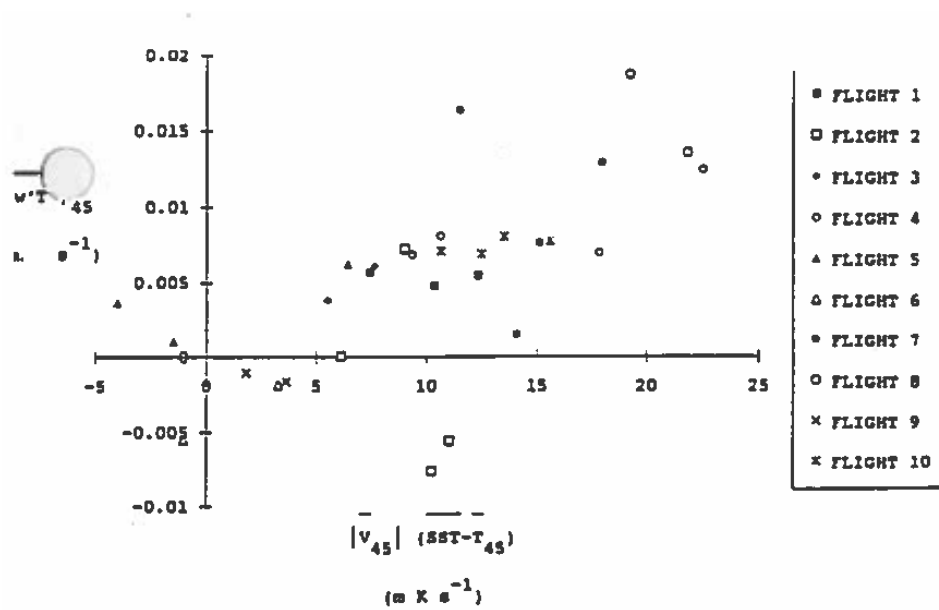
Figure 5.20 (SOURCE: Moyer and Young 1993)
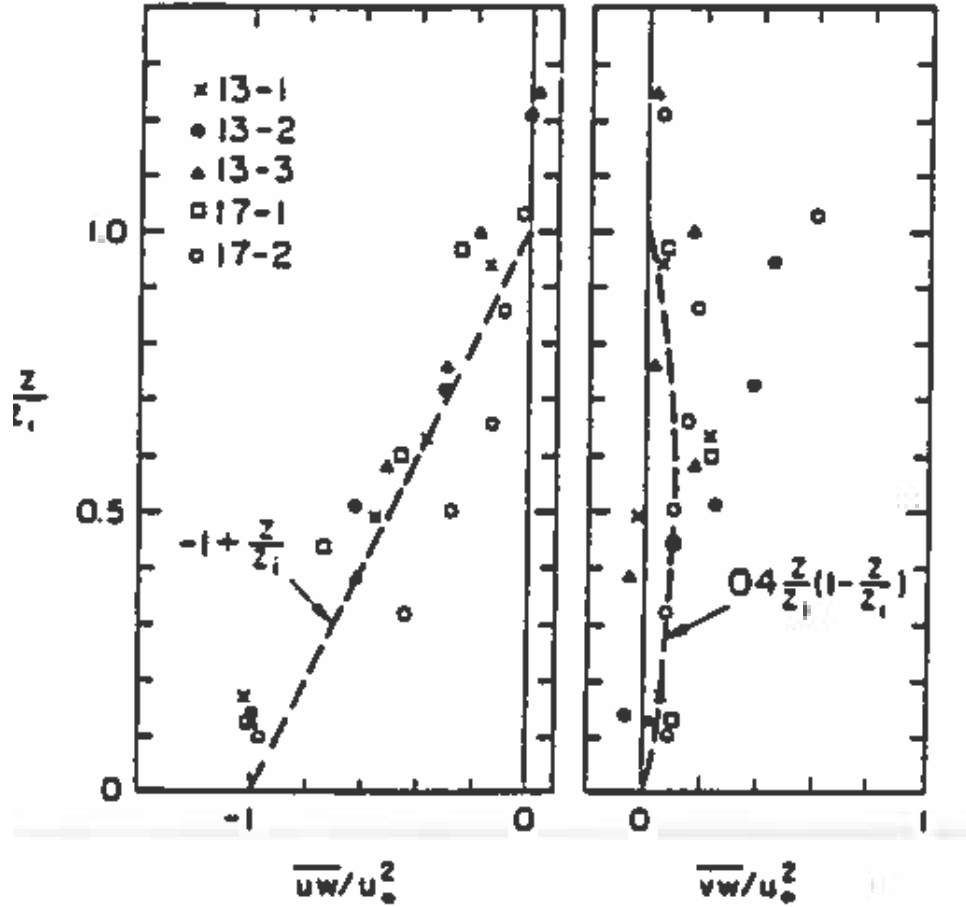
Figure 5.21 (SOURCE: Brost et al 1982)

longwave radiative cooling near the cloud top was balanced by entrainment of warm inversion air, and thus produced no impact on mixed-layer turbulence for the cases they analyzed. The mean wind was however very strong, $\sim$ 12–20 m/s, and the turbulence was driven mainly by shear. In those cases, the liquid water content near the cloud top was very low, $\sim$ 0.1 g/kg.

This type of PBLs has a very different structure comparing to buoyancy-driven stratocumulus PBLs. As pointed out by Brost et al., the structure is more like the neutral PBL, where the velocity fluxes and variances scaled well with the friction velocity u_*, as shown Figs. 5.21 and 5.22.

The temperature and moisture fluxes (Fig. 5.23) obtained by Brost et al. were

94

Figure 5.22 (SOURCE: Brost et al 1982)

quite complicated. In most cases the total water mixing ratio flux was not linear with height because drizzle occurred. The TKE budget (Fig. 5.24) showed a near balance between the shear production and dissipation, at least in their cases 13-2 and 17-2, which is a feature of neutral, shear-driven PBL.

From the above examples (observed and simulated), you can see that the vertical distributions of statistics (such as the buoyancy flux profile) in the STBL vary from case t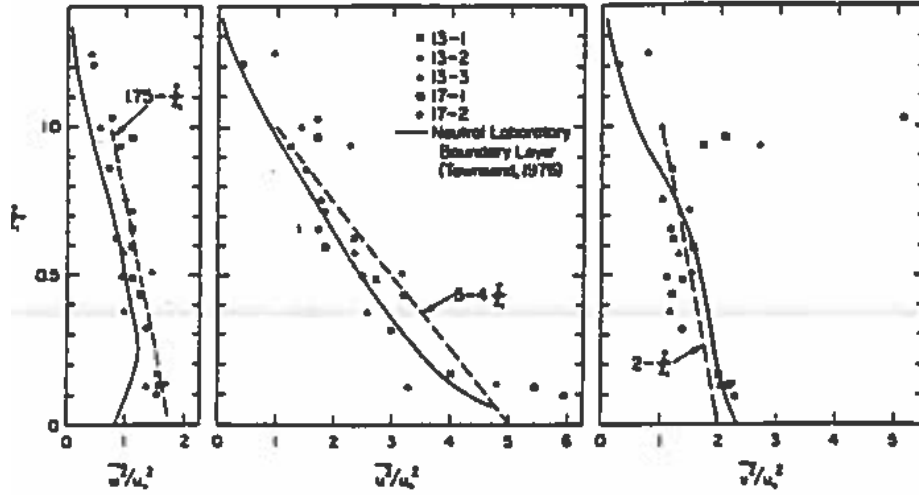o case; the distributions depend strongly on where and what the dominant turbulence sources (e.g., surface heating, cloud-top cooling and wind shear) are. Therefore, it is unlikely that we can scale the statistics into universal profiles, like we do for the CBL.

5.1.6   Climate-related issues

PBL stratocumulus plays a major role in climate, and hence it is important to accurately represent (parameterize) it in climate models. Randall et al. (1984; BAMS, 65, 1290-1301) pointed out that a mere 4% increase in the area coverage of marine stratocumulus regime could produce a 2-3 K cooling in the global mean temperature, based on a simple 1-D radiative equilibrium calculation. Such cooling is more than enough to offset the global warming due to doubling CO_2. This sensitivity was also found by T. Slingo (1990; Nature, 343, 49–51) using a 3-D general circulation model. He showed that the net albedo depends
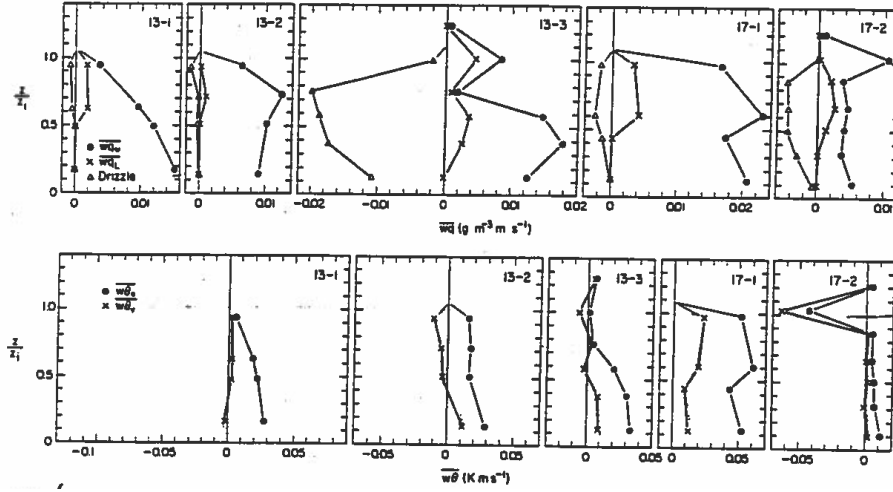
95

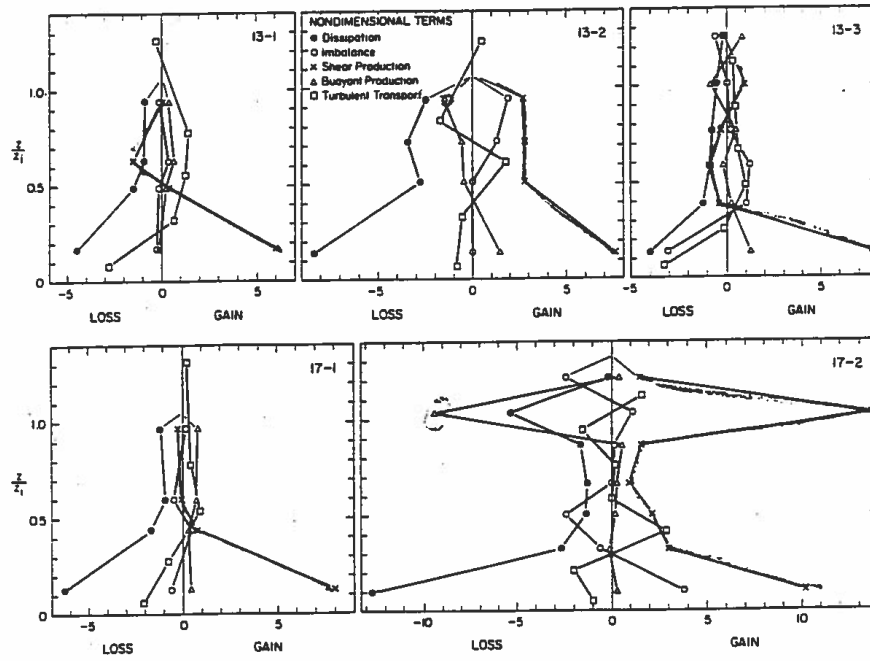Figure 5.23 (SOURCE: Brost et al 1982)

Figure 5.24 (SOURCE: Brost et al 1982)

sensitively on not only the cloud amount but also the details of cloud microphysics near the cloud top, such as the dropsize distribution. Not knowing how to accurately represent these cloud properties of the marine stratocumulus poses a big challenge in predicting climate changes.

To develop such a parameterization, we need to put our qualitative understanding of the cloud regime (described in early subsections) into quantitative forms. This is a difficult task, however, because as we have learned that there are many physical processes involved and all of them can play an important role in determining the cloud properties. One way to pursue this problem is to consider just a few dominant physical processes to see if we can express the turbulent fluxes and the cloud properties as functions of large-scale forcing and sounding. For such a study, we may ignore the solar radiation (and drizzle) and consider just some basic physical processes like longwave radiation, entrainment, turbulent transport, and condensation/evaporation.

But if one is interested in the direct impact of this cloud regime on climate, one needs to include solar radiation because the direct impact of stratocumulus is due to its much larger cloud albedo than the ocean surface's.

Current GCMs use very simple cloud schemes to represent the marine stratocumulus. The majority use an empirical cloud scheme developed by J. Slingo (1987, QJRMS, 113, 899–927), in which the cloud fraction depends on large-scale quantities like stability in the lower atmosphere (i.e., the inversion strength) and the relative humidity in the PBL. The scheme was developed based on climatology data and is purely empirical. One of the deficiencies of such a scheme is that the cloud field is not directly linked to the turbulence and radiation fields. In fact, most GCMs treat these three fields (turbulence, radiation and cloud) separately by using three separately developed schemes; the only link among these processes is through the large-scale mean field. As we have learned, these physical processes are strongly coupled on turbulence time scale, so they should be treated as a whole system in climate models. The only GCMs that directly link these processes are the ones that use mixed-layer models, developed by Randall and his UCLA/CSU colleagues (Suarez et al. 1983, MWR, 111, 2224–2243; Randall et al 1985, JAS, 42, 641–676), but in that type of modeling there are complicated closure problems (such as entrainment-rate closure) to deal with.

Finally, I would like to point out that most stratocumulus studies have been focused on cloud breakup mechanisms, e.g., decoupling, CTEI, stratus-to-cumulus transition; very few on formation processes. Before cloud forms, there is no cloud-top longwave cooling to drive the boundary-layer turbulence. And since most cloud regime exists over cold ocean surface, there is not much surface heat flux to generate turbulence either. How then is the moisture being transported upward to form cloud? One possibility is that this cloud regime, at the very upstream region, may form as fog, and then longwave radiative cooling occurs at the fog top, which drives turbulence; with more turbulence and entrainment the fog then evolves to an elevated cloud as it moves downstream. Another possibility is that the wind shear is strong in this upstream region to driven enough turbulence to carry moisture up to the lifting condensation level, then cloud forms. Without knowing what mechanism drives turbulence to form cloud, it is difficult to come up with a parameterization scheme for cloud formation.

5.2 *Shallow cumulus*

Shallow cumulus clouds occur often over the tropical and subtropical oceans. In the 70's when aircraft observationalists were searching for horizontally-homogeneous, quasi-steady state PBLs, they naturally went out to the tropical oceans to collect such data. Among those datasets were the Puerto Rico cases reported in e.g., LeMone and Pennell (1976; MWR, 104, 524–539) and the GATE data analyzed by e.g., Nicholls and LeMone (1980; JAS, 2051–2067).

A shallow-cumulus-topped PBL is often found to have a three-layer structure, as first observed by Malkus (1958; Papers Phys. Oceanogr., 13, 47pp): subcloud mixed layer, cloud layer, and the in-between transition layer, as sketched in Fig. 5.25. The transition layer is defined as the upper part of the mixed layer where entrainment effect is significant. Note that, unlike stratocumulus, cumulus clouds exist in a stably stratified environment, and their surrounding air is not very turbulent.

5.2.1 Interaction between cloud and subcloud layers

Among the three Puerto Rico cases they analyzed, LeMone and Pennell (1976) characterized two types of shallow cumulus clouds, that occurred in "suppressed" convective conditions,
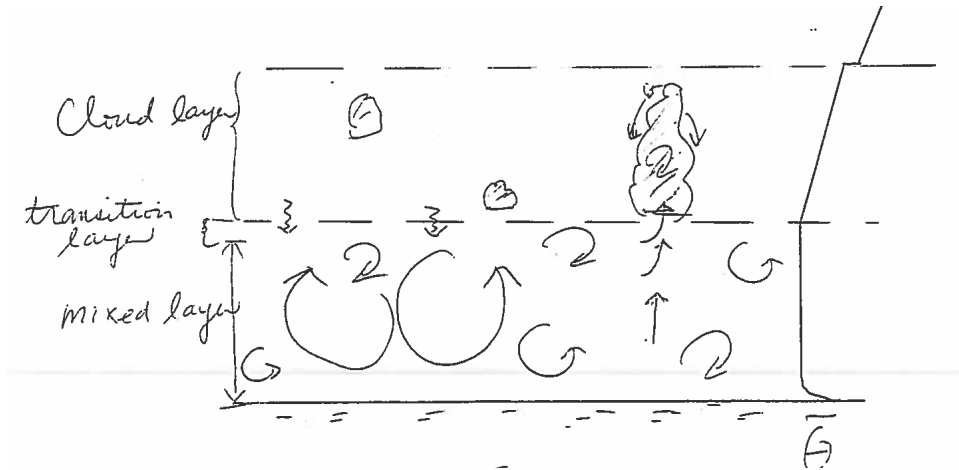
Figure 5.25

e.g., their Cases I and II, and that in more enhanced convection conditions, e.g., Case III. The difference between "suppressed" and "active" cumulus clouds was shown in their schematic diagram, Fig. 5.26.

In "suppressed" conditions, cumulus clouds formed at the tops of rising thermals from the mixed layer that penetrate into the condensation level. In Puerto Rico Cases I and II rising thermals were carried upward in the rising branches of 2-D roll vortices. This type of cumulus clouds is passive, and is like those described as "forced" cumulus clouds in Stull's book. These clouds are more likely to organize in lines, in the form of roll vortices. They do not dynamically alter subcloud layer.

For more enhanced cumulus convection, as in Case III, clouds were found to strongly interact with subcloud layer. This type is described as "active" cumulus clouds by Stull. These clouds are positively buoyant and the associated pressure fields may produce strong updrafts near the cloud base to "suck up" mixed-layer air into cumulus clouds (LeMone et al. 1988, MWR, 116, 2062–2068). These updrafts were traceable to at least 100m below cloud base, according to LeMone and Pennell.

5.2.2 Subcloud-layer spectra and statistics

Figure 5.27, taken from LeMone and Pennell, shows the wavelengths of spectral peaks in the u, v, and w wind fields, which represent the dominant eddy sizes, within the subcloud layer. Roll scales were observed in Cases I (diamonds) and II (circles), as seen in the v

99
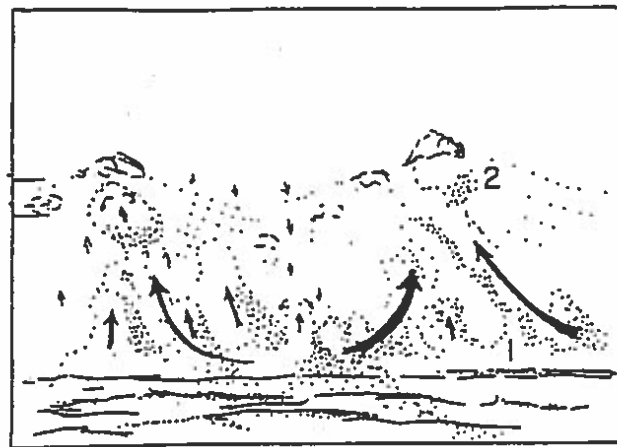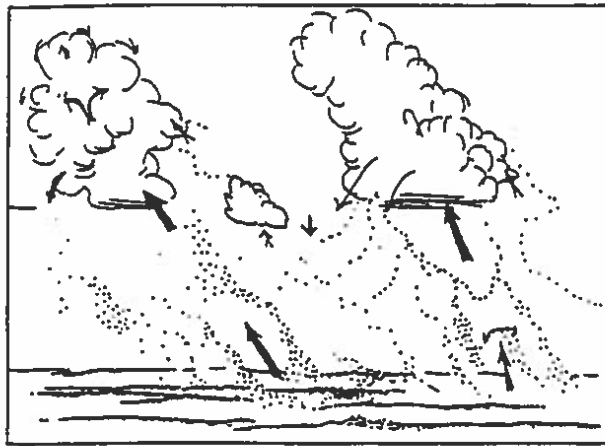
Figure 5.26 (SOURCE: LeMone and Pennell 1976)

(or u) spectrum, but less in the w spectrum since random turbulent motion dominates the w-spectrum. Convective roll vortices were not observed in Case III (triangles). Dominant turbulent eddies shown in the w spectrum increased nearly linearly with height to $\sim 0.5z_i$.
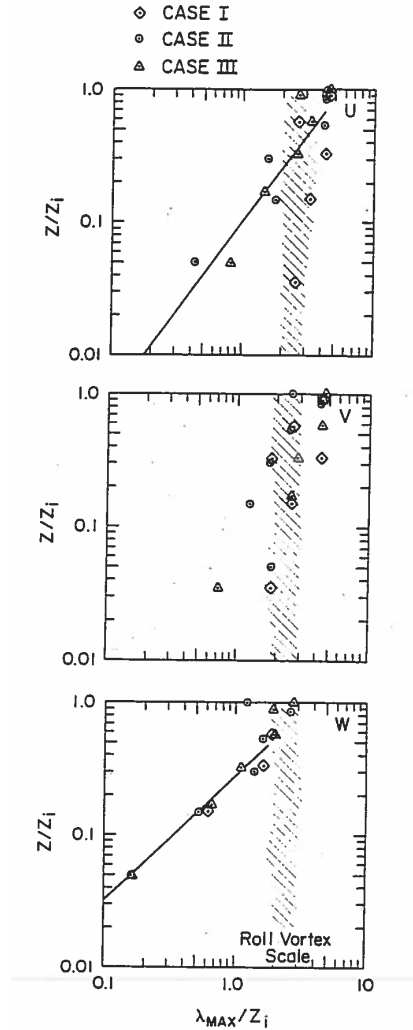
Figure 5.27 (SOURCE: LeMone and Pennell 1976)

The GATE aircraft data reported in Nicholls and LeMone (1980) were mostly under "suppressed" convective conditions and had much weaker winds than the Puerto Rico cases. 2-D roll vortices were not common there. Figure 5.28 shows that the peak wavelengths in the w-spectrum in the cumulus-topped mixed layer over the ocean had a similar distribution to, but larger in size than, those of CBLs over land reported by Kaimal et al. (1976). (Note that Kaimal et al. spectra were obtained from tethered balloon data, and hence should

101
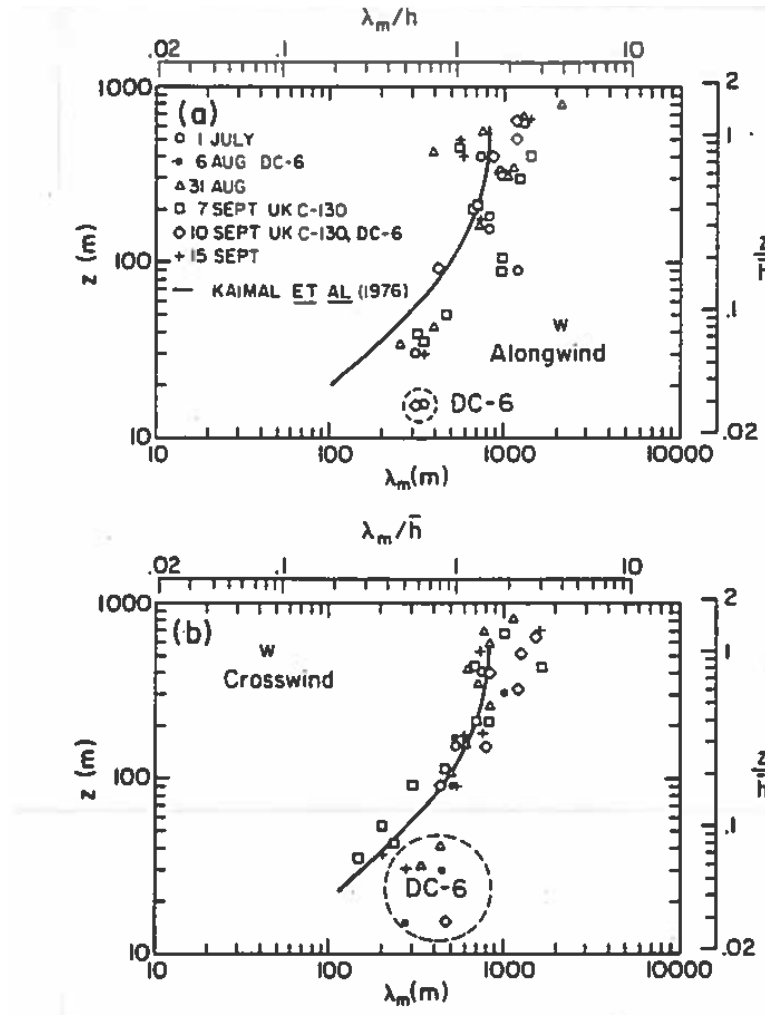
Figure 5.28 (SOURCE: Nicholls and LeMone 1980)

be compared with the alongwind aircraft data as shown in Fig. 5.28a.) In the moisture spectrum, Fig. 5.29, no clear dominant eddy size was found; fluctuations of the order of 10 km in scale often occurred and even dominated the spectrum. However, these large-scale bands carried very little moisture flux, as shown by the peaks in the $w - q$ cospectra, Fig. 5.30, taken from Nicholls and LeMone.

The horizontal structure of these large-scale fluctuations were constructed by LeMone and Meitin (1984; MWR, 112, 1985–1997), using several parallel flight legs at $z =$150m, shown in Fig. 5.31. The cloud base height in these cases was about 600m. There were clearly mesoscale band structures. LeMone and Meitin found that these bands were aligned with subcloud-

Figure 5.29 (SOURCE: Nicholls and LeMone 1980)
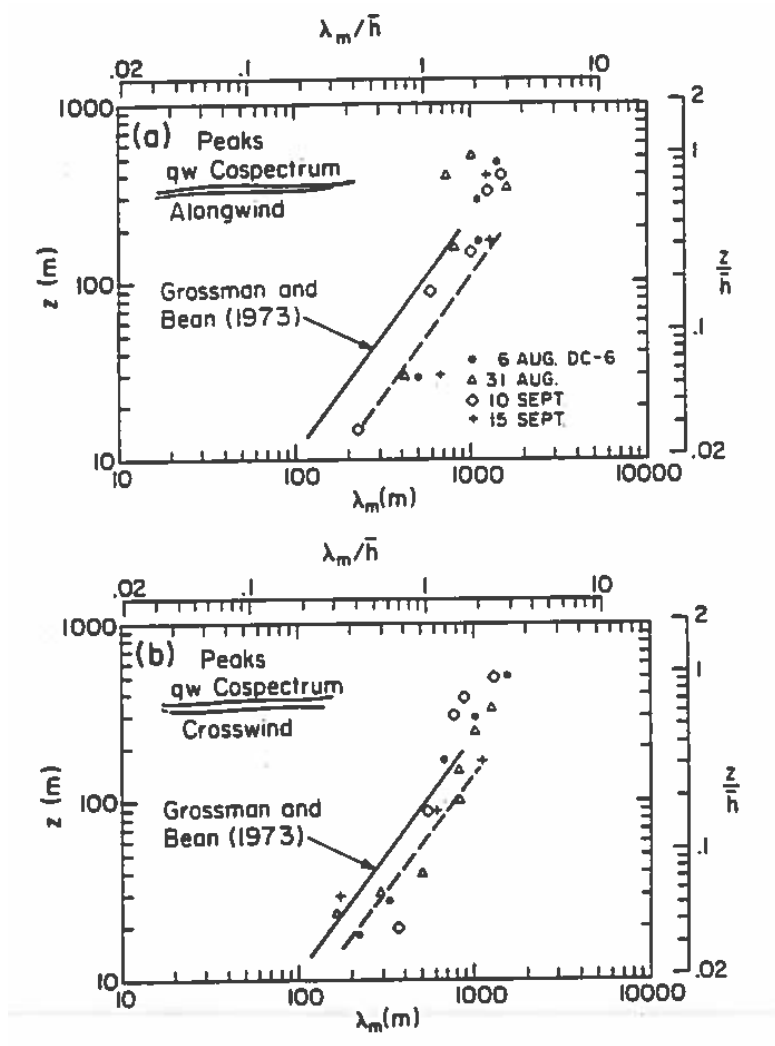
Figure 5.30 (SOURCE: Nicholls and LeMone 1980)
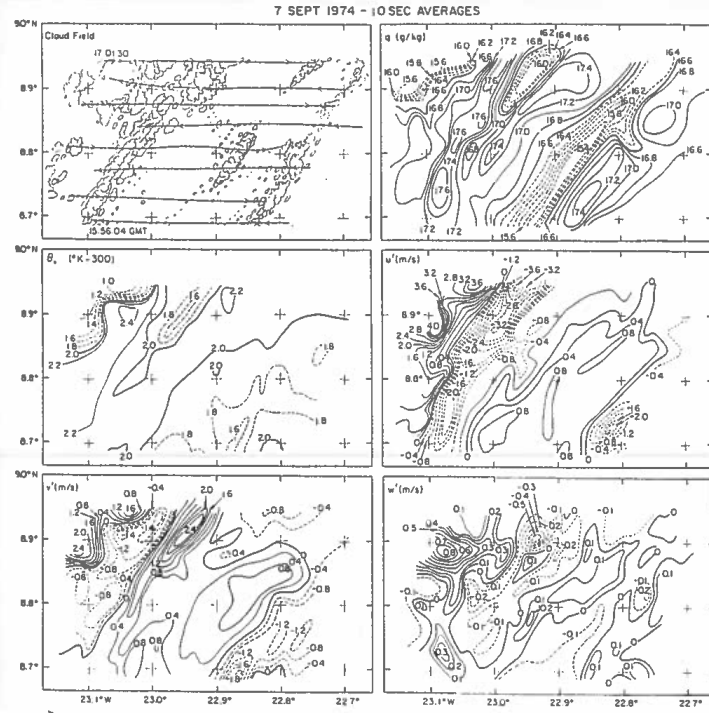
Figure 5.31 (SOURCE: LeMone and Meitin 1984)

layer shear and traveled in a direction of the subcloud-layer wind. Thus, they concluded that this 2-D structure is primarily subcloud-layer phenomena. The horizontal:vertical aspect ratios of these mesoscale bands are on the order of 25–50, similar to 3-D mesoscale cellular convection (i.e., open and close cells). These mesoscale organizations have a much larger aspect ratio than the 2-D roll vortices or 3-D irregular hexagonal convections we mentioned in section 3, which are scaled with z_i, i.e., aspect ratio ~ 1. What causes the large aspect ratio, either in 2-D or 3-D form, remains an interesting research topic. One hypothesis is that the structures resulted from modulation of the PBL by tropospheric gravity waves, which themselves may have originated from clouds, as discussed by Clark, Hauf, and Kuettner (1986; QJRMS, 112, 899-926). A numerical simulation by Balagi et al (1993; JAS, 50, 3571–3589) produced observed cloud structures, i.e., similar orientation and wavelengths.

The large eddy simulation method was used to simulate the Puerto Rico cases by Sommeria and LeMone (1978; JAS, 25–39), and then recently by Cuijpers and Duynkerke (1993; JAS, 50, 3894–3908) and a BOMEX case by Siebesma and Cuijpers (1995; JAS, 52, 650–666). Most of the fluxes or variances obtained from those simulated fields agreed quite well with

105
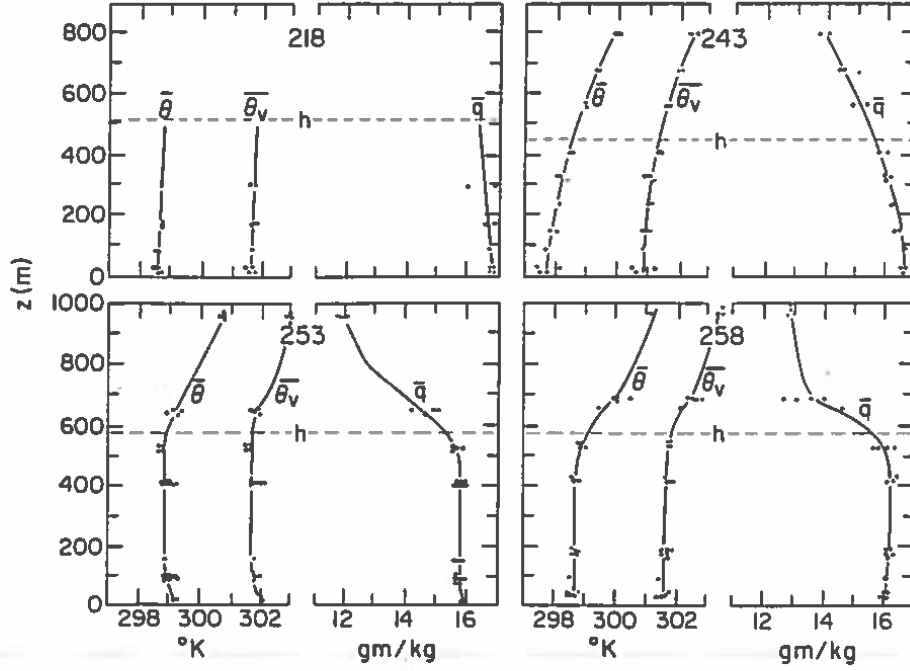
Figure 5.32 (SOURCE: Nicholls and LeMone 1980)

observations. The KNMI (Siebesma et al.) has been using their LES solutions as database to develop mass-flux parameterizations of cumulus for GCMs.

I also show the GATE observations: mean fields in Fig. 5.32 moisture variance in Fig. 5.33, and the temperature and moisture fluxes in Fig. 5.34, taken from Nicholls and LeMone (1980). The subcloud layer was well mixed. As indicated in the moisture variance profiles, the upper part of the mixed layer was strongly affected by entrained dry air from above. Figure 5.35 showed that $\overline{wT}$ and $\overline{wq}$ at the cloud base varied among different cases, while $\overline{wT_v}$ at the cloud base remained nearly zero. This led Nicholls and LeMone to conclude that "the sensible and latent heat fluxes at the top of the mixed layer (and therefore the distribution of heating and moistening in the boundary layer) are strongly affected by the presence or absence of cumulus convection while the virtual heat flux remains unaffected."

Another interesting study in the Nicholls and LeMone paper is on the convective mass flux, which is a closure in mass-flux modeling as we will learn in section 6. In mass flux modeling, the vertical flux of any scalar c is expressed as
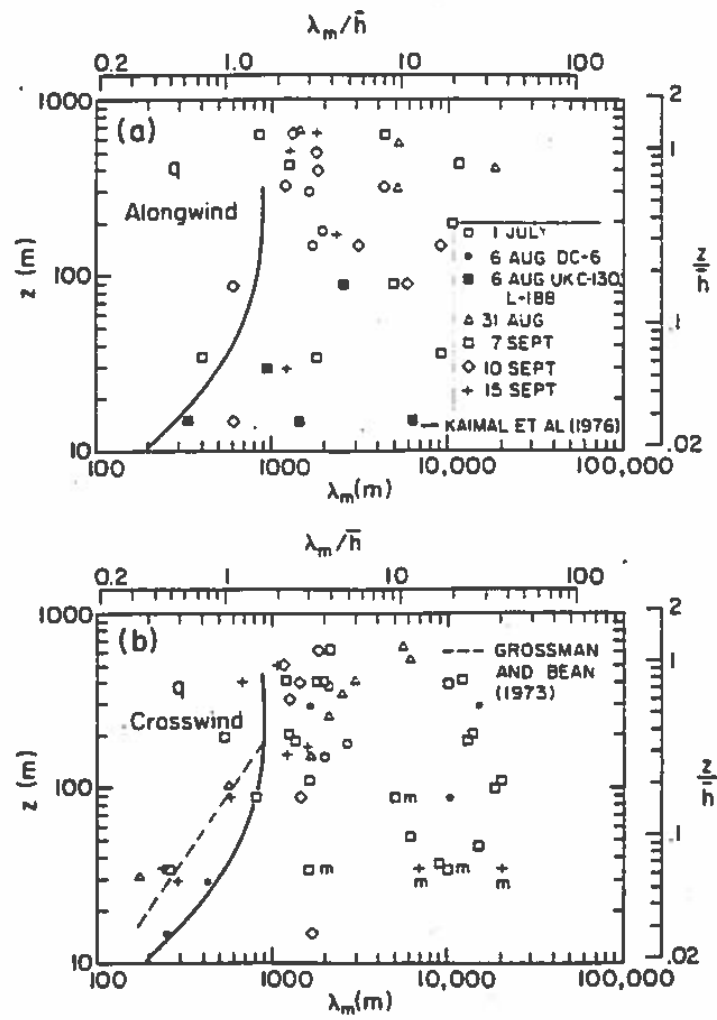
$$\overline{wc} = \omega_c(C_U - C_D), \tag{60}$$

106
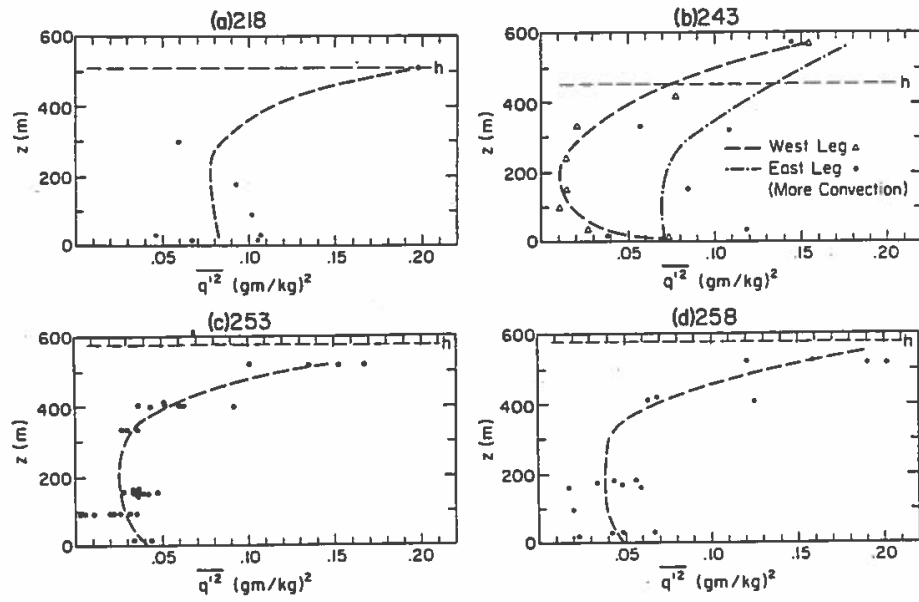
Figure 5.33 (SOURCE: Nicholls and LeMone 1980)
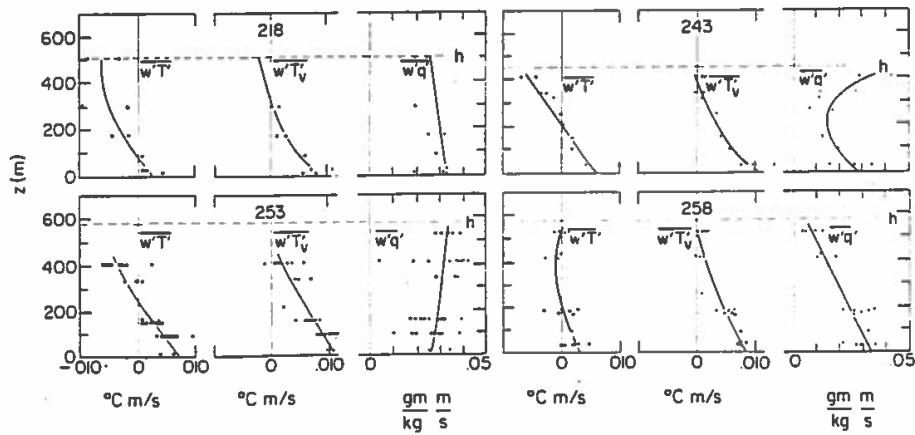
Figure 5.34 (SOURCE: Nicholls and LeMone 1980)
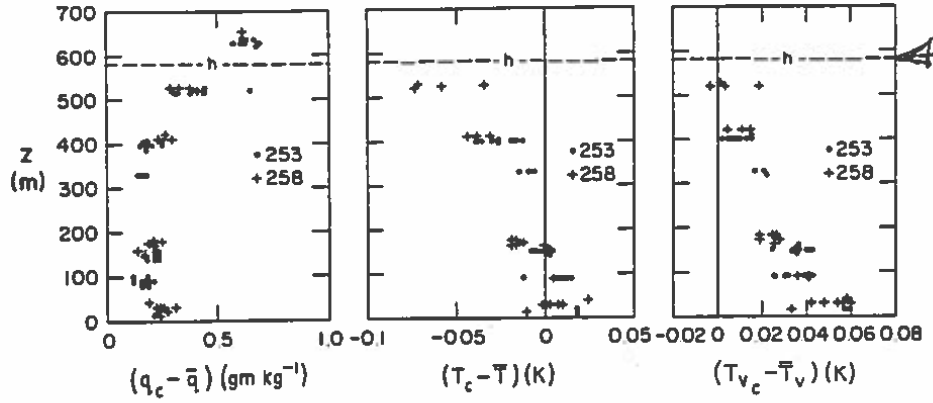
Figure 5.35 (SOURCE: Nicholls and LeMone 1980)

where $\omega_c \equiv \sigma(1-\sigma)(w_U - w_D)$ is a convective mass flux; σ is the area covered by all updrafts; w_U and w_D are averaged vertical-velocity speeds within updrafts and downdrafts, respectively; and C_U and C_D are averaged concentrations of c within updrafts and downdrafts. Another way to write (60) is

$$\overline{wc} = \omega^*(C_U - \overline{C}). \tag{61}$$

$\overline{C}$ is the averaged concentration over the whole horizontal plane, i.e., over both updraft and downdraft regions, defined as $\overline{C} = \sigma C_U + (1 - \sigma)C_D$. $\omega^* \equiv \sigma w_U$ is also a convective mass flux. Nicholls and LeMone used the GATE data, which gave the fluxes shown in Fig. 5.34 and the differences $(q_U - \overline{q})$, $(T_U - \overline{T})$, and $(T_{vU} - \overline{T_v})$ shown in Fig. 5.35, to compute ω^*; their results are shown in Fig. 5.36. Nicholls and LeMone noted that the mass flux at the cloud base was only a small fraction of that in the middle of the mixed layer. Nevertheless, this small amount of cloud-base mass flux ($\sim 0.1\omega^*/w_*$) produced large fluxes of sensible temperature and moisture there, because $T_U - \overline{T}$ and $q_U - \overline{q}$ were large at the cloud base. Note that the vertical distribution of this mass flux was similar to the profile of standard deviation of vertical velocity shown in Fig. 5.37, so we may assume that $\omega^* \propto \sigma_w$; they are both larger at the cloud-base level when clouds are present at the top of the mixed layer, compared to the clear CBL. This provides important information for mass flux modeling, as we will see in section 6.
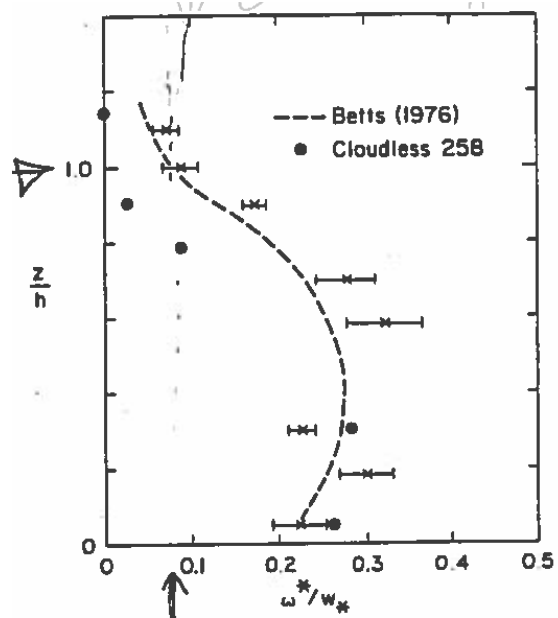
Figure 5.36 (SOURCE: Nicholls and LeMone 1980)
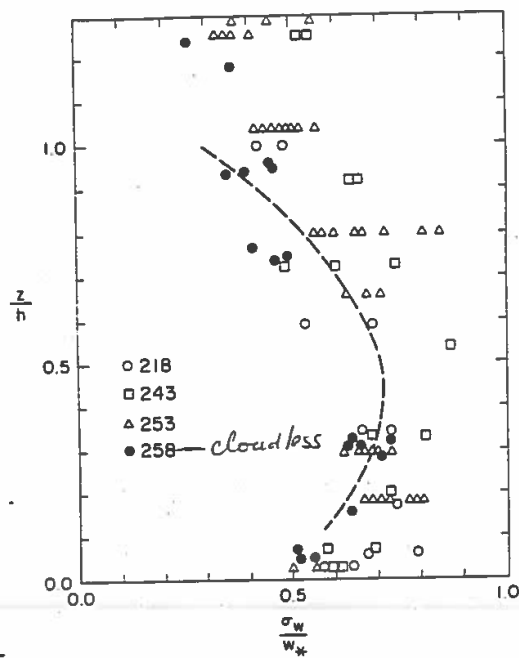
Figure 5.37 (SOURCE: Nicholls and LeMone 1980)

5.2.3 Climate impact

Trade-wind cumulus plays an important role in transporting moisture from the ocean surface to the lower troposphere, which is then advected to the ITCZ to supply the moisture to deep convection. Recently, the KNMI research group (e.g., Siebesma and Cuijpers 1995; JAS 52, 650–666; Siebesma 1997; NATO ASI Series on Buoyant Convection in Geophysical Flows, Kluwer Academic Publishers, 491pp) has been using LES as database to develop mass flux parameterizations of trade cumulus for GCMs. For such a development, some basic questions need to be answered first. For example: What determines the mass flux from the mixed layer into cumulus clouds? How does the cumulus ensemble affect the mixed-layer turbulence? How to parameterize the later mixing between the cumulus ensemble and its environment?

6 PBL MODELS (PARAMETERIZATIONS)

PBL modeling (or called PBL parameterization) is an attempt to describe the statistical behavior of PBL turbulence through simplified equations or modeling frameworks. We can *parameterize* PBL turbulence in a climate or weather forecast model because its time scale is much shorter than the time scale of large-scale variation. Thus we can assume that turbulent flow responds to large-scale forcing almost instantaneously and that its statistics remain at an equilibrium state for a given large-scale environment. A PBL model is usually designed to provide the following statistical information to a large-scale model: the PBL depth, surface stress, surface fluxes of heat, moisture and other species, vertical profiles of these fluxes within the whole PBL, and cloud amount, if the large-scale condition favors low-level clouds. The surface fluxes are needed to couple the atmosphere with the land processes, the vertical profiles of fluxes determine the time-rate-of-changes of wind speed, wind direction, temperature, and moisture, etc., and cloud amount determines the amount of radiation in/out of the Earth's surface. Therefore all meteorological forecast models need a PBL model.

We may categorize all existing PBL models into six different frameworks: Higher-order closure model, Richardson-number-dependent K approach, K-profile model, mixed-layer (bulk) model, transilient theory/integral closure model, and mass flux model. As we will learn next, some models are more elegant and sophisticated than others, but as John Wyngaard stated, they don't necessarily perform better than simple models. As John put it: "The key to PBL model performance is not its framework, but calibration against data". It is also important to note that all schemes are just an attempt to describe complicated turbulence processes with a simple set of equations or frameworks. We should never expect any of them to work perfectly. As Lumley stated, these models at their best produce only likenesses of turbulence, and work only in a limited range about their calibration state. Some PBL models are developed for—or calibrated against—shear-driven turbulence, and others are for buoyancy-driven turbulence.

6.1 *Higher-order closure model (or single-point closure)*

6.1.1 Higher-moment equations and closure problems

Higher-order closure modeling began in the 1970s when researchers found that simple eddy diffusivity (K) models failed to properly represent the PBL turbulence, especially the buoyancy-driven turbulence, and also because computers became more powerful. This turbulence modeling approach carries prognostic equations for higher-moment statistics. The idea behind this approach is that "if a crude assumption for second moments predicts first moments adequately, perhaps a crude assumption for third moments will predict second moments adequately" (Lumley and Khajeh-Nouri 1974; Advances in Geophysics, 18A, 169–192). The hypothesis is that if you solve higher moment equations where you make closure assumptions, you are likely to get a better mean (first-moment) field. There is no prove to this hypothesis, however.

Higher-order closure modeling is sometimes referred to as single-point closure modeling because the statistics it predicts are correlations at the same location, e.g., $\overline{u'(x_i)w'(x_i)}$.

All of the moments equations can be derived from the equations of fluctuations u', v', and w', Eq. (1-9). For example, equations for $\overline{u^2}$, $\overline{v^2}$ and $\overline{w^2}$ are:

$$\frac{\partial \overline{u^2}}{\partial t} = -\frac{\partial \overline{wu^2}}{\partial z} - 2\overline{uw}\frac{\partial U}{\partial z} - 2\overline{u\frac{\partial p}{\partial x}} - \epsilon_u, \tag{62}$$

$$\frac{\partial \overline{v^2}}{\partial t} = -\frac{\partial \overline{wv^2}}{\partial z} - 2\overline{vw}\frac{\partial V}{\partial z} - 2\overline{v\frac{\partial p}{\partial y}} - \epsilon_v, \tag{63}$$

$$\frac{\partial \overline{w^2}}{\partial t} = -\frac{\partial \overline{w^3}}{\partial z} + 2\frac{g}{\Theta_0}\overline{w\theta} - 2\overline{w\frac{\partial p}{\partial z}} - \epsilon_w, \tag{64}$$

where on the right-hand sides are turbulent transport, mean shear (or buoyancy) production, pressure effect, and molecular dissipation terms. Here we applied the *PBL assumption* so the x and y derivatives of all statistics are set to zero. The sum of these three equations yields the equation of the turbulent kinetic energy, $E \equiv (\overline{u^2} + \overline{v^2} + \overline{w^2})/2$. Similarly, we can derive all third moment equations, such as those for $\overline{u_i u_j u_k}$ or $\overline{wE}$.

Higher-moment equations are formally derived from the fluctuation equations without any assumptions; each terms in the budget have its physical meanings. This makes the

higher-order closure approach very attractive and popular in the 70s and early 80s. It was considered elegant and sophisticated.

However, through such derivations, the budget (right-hand side) of every higher-moment equation always consists of one or more higher moment terms. For example, in the second-moment equation for $\overline{u_i^2}$, a third-moment term $\overline{wu_i^2}$ appears on the right-hand side. Thus, to solve the second-moment equations, one has to (1) make closure assumptions that relate $\overline{wu_i^2}$ to lower moment (second or first) statistics, or (2) carry prognostic equations for $\overline{wu_i^2}$ and make closure assumptions on the 4th-moment terms. The first approach is called second-order closure modeling, and the second approach is 3rd-order closure modeling. For 3rd-order closure modeling, we can use a well-established turbulence theory, called quasi-normal (or called quasi-Gaussian) approximation, to relate fourth moments to second moments as $\overline{abcd} = \overline{ab}\ \overline{cd} + \overline{ac}\ \overline{bd} + \overline{ad}\ \overline{bc}$, which is more accurate than the downgradient assumption (described later) used in the second-order closure modeling. But a 3rd-order closure modeling requires solving many more prognostic equations. For a cloudy PBL, Moeng and Randall's (1984; JAS, 41, 1588–1600) 3rd-order closure model carries 31 more prognostic equations than a 2nd-order closure model.

If one stays with the second-order closure approach, as most PBL modelers do, then closure assumptions are needed for third-moment turbulent transport, pressure-related terms, and molecular dissipation terms, e.g., 1st, 3rd, and 4th terms on the right-hand sides of (62), (63), and (64).

The basis of making closure assumptions is well described in Donaldson (1973; *Workshop on Micrometeorology*, Ed. D.A. Haugen, AMS, 313–392). Each closure formula has to a) be invariant under both coordinate and Galilean transformations, b) have the right dimensional properties on both sides of the formula, and c) satisfy all the conservation relationships known to govern the variables in question. For example, a third moment term, $\overline{u_i u_j u_k}$, can be expressed as

$$\overline{u_i u_j u_k} \propto \frac{\partial}{\partial x_i}\overline{u_j u_k} + \frac{\partial}{\partial x_j}\overline{u_i u_k} + \frac{\partial}{\partial x_k}\overline{u_i u_j}, \tag{65}$$

in order to be invariant under coordinate transformation. To have the same dimensions on both sides of the formula, we must have

$$\overline{u_i u_j u_k} \propto -\lambda q[\frac{\partial}{\partial x_i}\overline{u_j u_k} + \frac{\partial}{\partial x_j}\overline{u_i u_k} + \frac{\partial}{\partial x_k}\overline{u_i u_j}], \tag{66}$$

where λ is a characteristic length scale and q is a characteristic velocity scale. The minus sign is added to insure that turbulent energy is diffused down the gradient. This is the well-known *downgradient diffusion assumption*. As we will see later, however, this assumption is inappropriate for buoyancy-driven turbulence.

Molecular dissipation terms are typically written as a decay form, for example,

$$-\epsilon_{u_i} = -\nu \overline{\frac{\partial u_i}{\partial x_i} \frac{\partial u_i}{\partial x_i}} \sim -\frac{\overline{u_i^2}}{\Lambda} \tag{67}$$

in the $\overline{u_i^2}$ equations, where Λ is a dissipation length scale.

Pressure fluctuations act to "return" the turbulent motion to an isotropic state, which can be understood from the following analysis: The pressure terms in (62)-(64) can be re-written as

$$-\overline{u_i \frac{\partial p}{\partial x_i}} = -\frac{\partial \overline{u_i p}}{\partial x_i} + \overline{p \frac{\partial u_i}{\partial x_i}}, \tag{68}$$

where the first term is a transport. The second term on the right-hand side of (68) drops out of the TKE equation, since $\overline{p \partial u_i / \partial x_i} = 0$ for incompressible fluid. But each individual component, $\overline{p \partial u / \partial x}$, $\overline{p \partial v / \partial y}$ or $\overline{p \partial w / \partial z}$ is not zero. So such pressure-related terms do not *generate* turbulent energy; they only *redistribute* energy among $\overline{u^2}$, $\overline{v^2}$, and $\overline{w^2}$ components. For example, in buoyancy-driven turbulence, buoyancy [2nd term in (64)] produces $\overline{w^2}$ and through the pressure effect $\overline{w^2}$ energy is redistributed to $\overline{u^2}$ and $\overline{v^2}$. In shear-driven turbulence, the along-shear energy is gained directly from the shear production [2nd term in (62) if U is the streamwise component], then pressure fluctuations redistribute it to $\overline{v^2}$ and $\overline{w^2}$. Hence, this term generates the *return-to-isotropy* effect first discussed by Rotta in 1951.

Thus, in general the pressure terms $-\overline{u_i \partial p / \partial x_j}$ are often expressed as

$$-\overline{u_i \frac{\partial p}{\partial x_j}} - \overline{u_j \frac{\partial p}{\partial x_i}} = -\frac{1}{\tau}(\overline{u_i u_j} - \frac{2}{3}\delta_{ij}\overline{E}), \tag{69}$$

where τ is the return-to-isotropic time scale. This pressure closure includes only the nonlinear turbulence-turbulence interaction, which is referred to as the "slow" part of pressure effect. To include the direct effects of mean shear and buoyancy, "rapid" parts should be added to the closure formula (69); for example, the "rapid" part of pressure closures due to mean shear takes the form of $\partial U_i / \partial x_j$ and $\partial U_j / \partial x_i$ (e.g., Launder, et al., 1975; J. Fluid Mech., 68, 537–566) and that due to buoyancy takes the form of $\frac{g}{\Theta_0}\overline{\theta c}$ in the budget of $\overline{wc}$ (Moeng and

114

Wyngaard 1986; JAS, 2499–2513). The contribution from the rapid part can be as large as that from the slow part.

Under the *PBL assumption*, the transport term, first term in (68), is zero in the $\overline{u^2}$ and $\overline{v^2}$ equations; the only pressure transport term shows up after summing up all three velocity-variance components is $-\frac{\partial \overline{wp}}{\partial z}$, as shown in the TKE equation (derived in Homework 1C, Section 1.3). This transport term is neglected under the closure assumption (69). But as we showed in Fig. 3.10 this pressure transport term can be large in the buoyancy-driven PBL.

6.1.2 The Mellor-Yamada model

In early 70s, Mellor and Yamada realized that it was too computationally costly in a GCM or mesoscale model to use a full set of second-order closure model. They developed a hierarchy of models for the PBL where they systematically reduced the set of equations using a non-dimensional measure of anisotropy, $a \equiv ||a_{ij}||$, where $\overline{u_i u_j} = (\delta_{ij}/3 + a_{ij})\overline{u_i^2}$ (Mellor and Yamada 1974; JAS, 31, 1791–1806). This hierarchy is summarized below.

Level 4   All second moment are solved with full equations

Let advection and turbulent transport=O(a) and neglect O(a^2) terms $\Rightarrow$

Level 3   Only TKE and $\overline{\theta^2}$ are solved with full equations

Let advection and turbulent transport=O(a^2) and neglect O(a^2) terms $\Rightarrow$

Level 2   All second moment equation are reduced to algebraic forms

Neglect all O(a) terms $\Rightarrow$

Level 1   All second moment equation are reduced to algebraic forms

The so-called Level 4 model is a full second-order closure model, which solves for the full set of prognostic equations of all second moments. Level 3 neglects all the time-rate-of-change and turbulent transport terms except those in the equations of TKE and temperature variance (θ^2). Level 2 further neglects the time-rate-of-change and turbulent transport terms in the TKE and the $\overline{\theta^2}$ equations. Hence in Level 2, all second-moment equations reduces

to a set of simplified diagnostic (algebraic) equations; one can analytically solve that set of algebraic equations, which leads to the following flux-gradient relationships:

$$\overline{uw} = -K_M \frac{\partial U}{\partial z}, \tag{70}$$

$$\overline{vw} = -K_M \frac{\partial V}{\partial z}, \tag{71}$$

and

$$\overline{w\theta} = -K_H \frac{\partial \Theta}{\partial z}, \tag{72}$$

where $K_M = \ell q S_M(R_i)$ and $K_H = \ell q S_H(R_i)$, where ℓ and q are length and velocity scales (to be defined later) and R_i is the Richardson number. Thus, Level 2 looks like a Richardson-number-dependent eddy diffusivity model (to be described next), except that their K_M and K_H are formally derived from a set of moment equations, rather than determined empirically. Level 1 has K_M and K_H similar to those in Level 2 but is seldom, if ever, used.

The most popular higher-order closure scheme used in GCMs or mesoscale models is Level 2.5, which is an intermediate version between Level 2 and Level 3; it makes a further simplification to the Level 3 model so that the only full prognostic equation retained is the TKE equation. The Mellor-Yamada Level 2.5 model, also called TKE model or known to the engineering community as a One-Equation Model, is described in Mellor and Yamada (1982; Rev. Geophys. Space Phys., 20, 851–875) and briefly summarized below.

$$\frac{\partial E}{\partial t} = \frac{\partial}{\partial z}[\frac{5}{3}q\lambda_1 \frac{\partial E}{\partial z}] - \overline{uw}\frac{\partial U}{\partial z} - \overline{vw}\frac{\partial V}{\partial z} + \frac{g}{\Theta_0}\overline{w\theta} - \epsilon, \tag{73}$$

where the first term on the right-hand-side comes from the downgradient assumption for the sum of the turbulence and pressure transport terms. The length scale is empirically set to $\lambda_1 \sim 0.23\ell$, where ℓ is a master length scale defined later. The fluxes $\overline{uw}$, $\overline{vw}$ and $\overline{w\theta}$ are calculated from their algebraic equations. The molecular dissipation term is parameterized as

$$\epsilon = q^3/\Lambda_1, \tag{74}$$

where the dissipation length scale is empirically set to $\Lambda_1 \sim 15\ell$.

The most difficult and uncertain part of the higher-order closure approach is in determining the characteristic scales of length and time (i.e., ℓ, and τ) that appear in the above closure

formulae. These scales are supposed to represent the net effect of *all* turbulent motions—large and small eddies— and thus depend strongly on the type of turbulent flow fields. [For comparison, the characteristic length scale in the subgrid-scale model in LES is supposed to represent the local-equilibrium inertial subrange eddies, and thus can be more reasonably and universally described by the effective grid size of LES.] In Mellor and Yamada's hierarchy models, all length scales (such as Λ_1 and λ_1) are assumed to be proportional to a master length scale, ℓ. The early version of Mellor-Yamada models used a length scale proposed by Blackadar (1962; J. Geophys. Res, 67, 3095–3102) as

$$\ell = \frac{\kappa z}{1 + \kappa z/\ell_0}, \tag{75}$$

where ℓ_0 is an asymptotic value given as

$$\ell_0 = \alpha \frac{\int_0^{z_i} qz\,dz}{\int_0^{z_i} q\,dz}, \tag{76}$$

where z_i is the PBL height, $q = \sqrt{2E}$, α is a proportionality constant to be determined (or calibrated) empirically. The newer version of Mellor-Yamada models uses an alternative method for the master length scale (Mellor and Yamada 1982; Rev. Geophys. Space Phys., 20, 851–875), in which a prognostic equation for $q^2\ell$ is solved; along with the equation for the TKE, the master length scale ℓ can be retrieved. All time scales are then related to the length and velocity scales as $\tau \propto \ell/q$.

In recent years, many turbulence researchers, particularly within the engineering community, have become critical to the second-order closure approach. They questioned the accuracy of the second-order closure modeling and argued that it is no longer needed for the development of second-order models because with the increase of computer power DNS and LES can explicitly calculate the turbulent motion, which represents turbulence more accurately. An interesting debate on this issue is given in Lumley (1990; *Whither Turbulence? Turbulence at the Crossroads*, Lecture Notes in Physics, vol. 37, Springer-Verlag). For the meteorology community, however, LES remains too costly to substitute for ensemble-mean closure model in representing the PBL in GCMs or mesoscale models.

6.1.3 Realizability issue

Solving moment equations with ad hoc closure assumptions for higher moment terms often leads to undesirable *realizability* problems, such as generating negative variances or quantities

not satisfying the Schwarz's inequality. These problems were first discussed in Schumann (1977, Phys. Fluids, 20, 721–725) and Lumley (1979, Adv. Appl. Mech., 18, 123-176). The crudest way to handle realizability problems is by imposing the *clipping approximation* as proposed by Andren et al (1976, JAS, 33, 476–481), where the predicted variances are set to zero if they become negative and the Schwarz' inequality is imposed for all predicted quantities. There were more sophisticated methods to handle the realizability issue (e.g., Galperin et al. 1988, JAS, 45, 55–62), but it remains one of the critiques of the higher-order closure modeling.

6.1.4 Applications to cloud-free PBLs

The Mellor-Yamada second-order closure models are well documented in the PBL literature, and perhaps the most popularly used PBL schemes. Among the series of papers published by Mellor and Yamada, Mellor (1973; JAS, 30, 1061–1069) showed that the second-order closure modeling, when applied to the surface layer, was able to reproduce Monin-Obuhkov similarity functions. Yamada and Mellor (1975; JAS, 32, 2309–2329) showed that this closure model can properly produce the diurnal cycle of mean fields of the Wangara data, as shown in Fig. 6.1. More applications are described in Mellor and Yamada (1982; Rev. Geophys. Space Phys., 20, 851–875).

Although Mellor-Yamada models can produce well some mean fields of the PBL, the TKE budget computed from their Level 4 model (top panel in Fig. 6.2) shows unrealistic features compared to observations and LESs (bottom panel in Fig. 6.2, from Moeng and Wyngaard; 1989, JAS, 46, 2311-2330). The modeled entrainment flux of potential temperature (i.e., $\overline{w\theta}$ at the PBL top) is nearly zero, instead of $\sim$–0.2 of its surface value. In fact, this model underestimates the entrainment fluxes of all variables. Also, the third-moment turbulent and pressure transport terms (labeled as "Diffusion" in Fig. 6.2) are greatly underestimated. In Section 6.1.6, we will examine the closure assumptions used by Mellor-Yamada, which will show why the TKE budget resulted from that model is unrealistic.

Because of its complexity, the second-order closure model developed by Lumley and his colleagues was rarely used in the PBL community except some earlier works by Wyngaard et al. (1974; Adv. Geophys. 18A, 193–212) and Zeman and Lumley (1976; JAS, 33, 1974-1988). Their closure schemes include more physics and hence are a lot more complicated
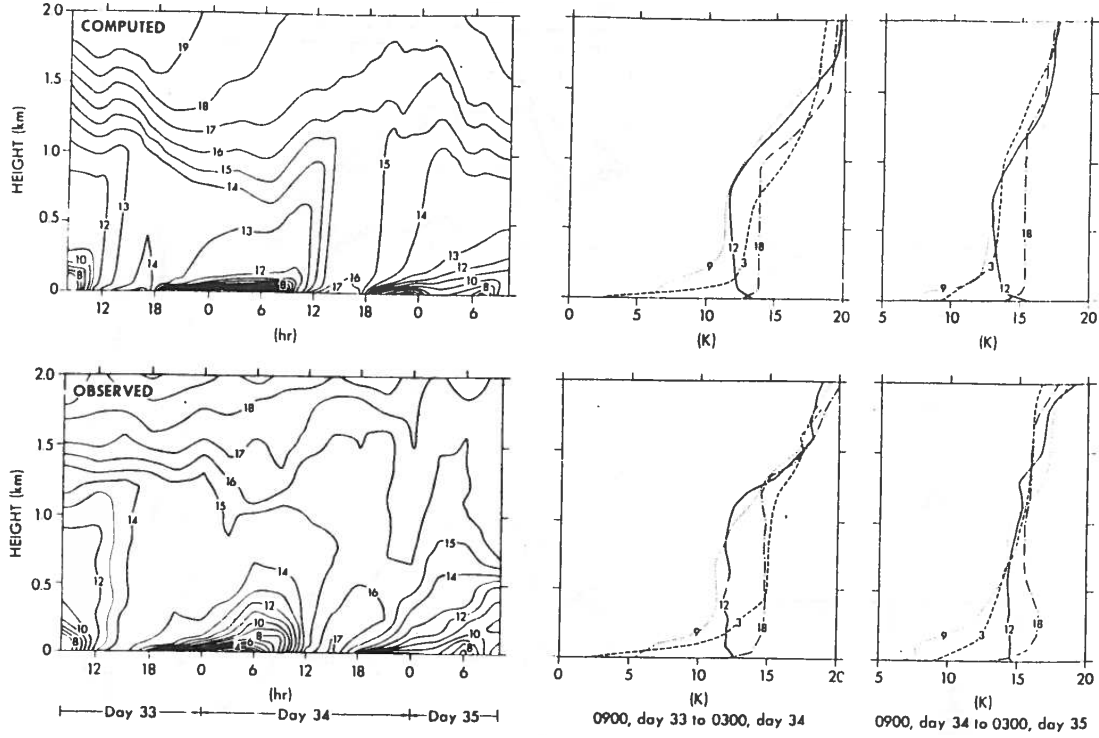
Figure 6.1 (SOURCE: Yamada and Mellor 1975)

and computationally expensive than the Mellor-Yamada's. This model, however, is shown to predict much reasonable entrainment fluxes, e.g., the entrainment flux of buoyancy as shown in Fig. 6.3; that success will be explained in Section 6.1.6. Note that Zeman-Lumley's model also predicts a reasonable vertical distribution of the TKE flux, $\overline{wE}$ (Fig. 6.4) for the buoyancy-driven PBL, and consequently a reasonable turbulent transport term (which is $-\partial \overline{wE}/\partial z$) in the TKE budget.

Second-order closure modeling has also been applied to the stably stratified PBL. In Wyngaard (1975; BLM, 9, 441–460), a full second-order closure model was used to model a stable PBL and the results agreed well with observations. Figure 6.5 compares the time evolution of the calculated and observed (a) friction velocity (i.e., r.m.s. of surface momentum fluxes), (b) surface heat flux, and (c) PBL height.

Brost and Wyngaard (1978; JAS, 35, 1427–1440) further simplified Wyngaard's full second-order closure model to a K-type model by neglecting the time-rate-of-change and turbulent transport terms. (For stable or neutral PBLs, we have learned that the turbulent transport terms are typically much smaller than the production and dissipation terms in the

119
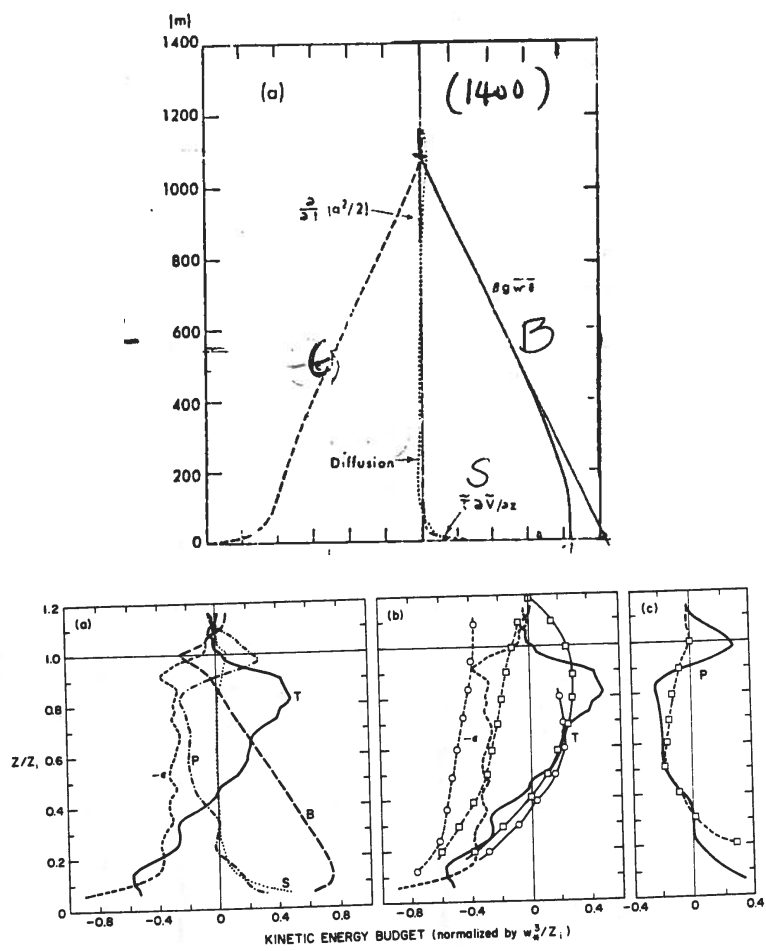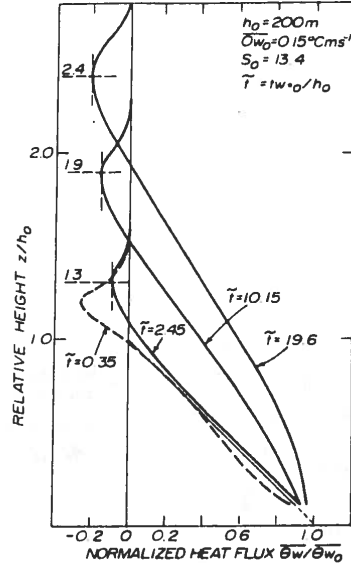
Figure 6.2

Figure 6.3 (SOURCE: Zeman and Lumley 1976)
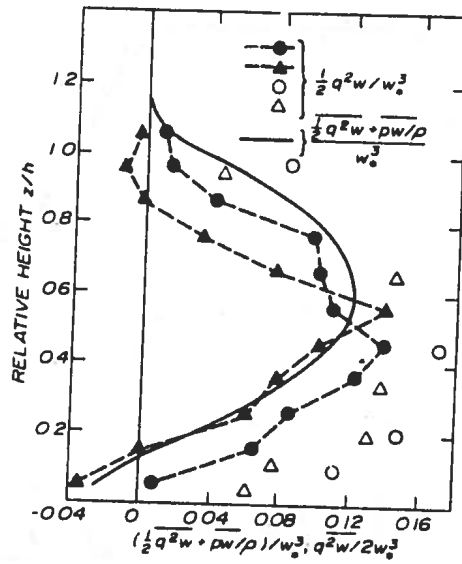
Figure 6.4 (SOURCE: Zeman and Lumley 1976)
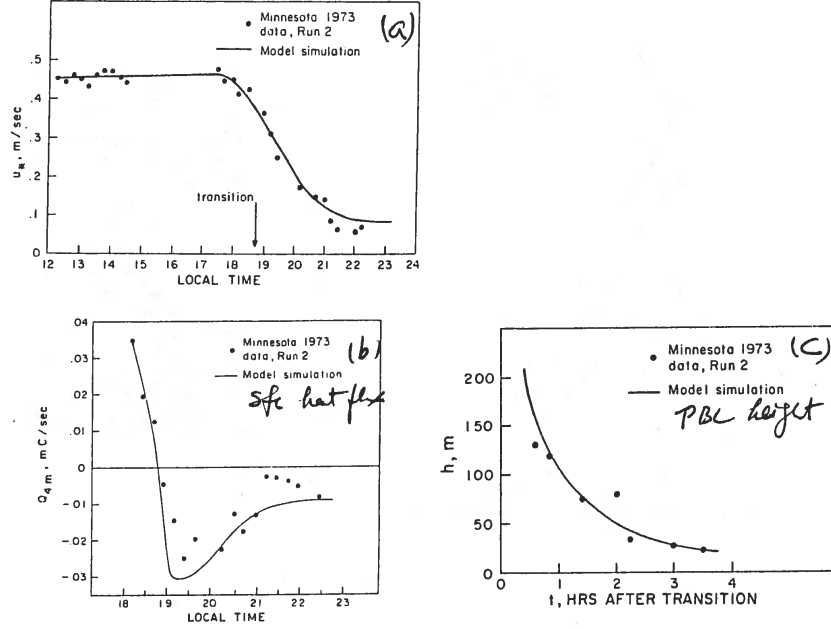
Figure 6.5 (SOURCE: Wyngaard 1975)

TKE budget.) Also, instead of solving a prognostic equation for the molecular-dissipation rate, they parameterized the length scale as

$$\ell = \frac{z}{1 + z/\ell_B}, \tag{77}$$

where ℓ_B is given as

$$\ell_B^2 = \frac{\overline{w^2}}{\frac{g}{T_0} \frac{\partial \Theta}{\partial z}}, \tag{78}$$

which came from the assumed balance between inertial forces $(\sim \overline{w^2}/\ell_B)$ and buoyancy forces $[\sim (g/T_0)(\partial \Theta/\partial z)\ell_B]$. Thus, $\ell \sim z$ near the surface, which is a well-known surface-layer property, and $\ell \sim \ell_B$ in the upper part of the stable PBL. This much simplified second-order closure scheme was shown to reproduce all turbulence results obtained in Wyngaard (1975). This is perhaps not surprising because we showed that eddies within the stably stratified PBL are small and turbulent mixing is more or less local. Thus, a simple K model with a proper length scale as given in (77) and (78) can model the stable PBL well.

6.1.5 Applications to stratocumulus-topped PBL

To apply the second-order closure approach to the stratocumulus-topped PBL, we need to make some modifications: Instead of using θ (or θ_v) and its related moment statistics as prognostic variables, we should use thermodynamic variables that are conserved under moist adiabatic processes, e.g., θ_e (or θ_l) and its related statistics. Only conserved quantities can become well mixed by turbulence. The buoyancy (or liquid water) statistics are then computed from the predicted statistics through thermodynamic relationships, e.g., $\overline{w\theta_v} = a\overline{w\theta_e} + b\overline{wq_T}$, where the coefficients a and b differ for unsaturated and saturated air. In partly cloudy region, which is often the case in a GCM grid, buoyancy statistics can no longer be easily related to the conserved thermodynamic statistics (see Randall 1987; JAS, 44, 850–858). This remains a research problem.

For modeling the cloud-top PBL, we also need to add the radiation effect into the mean equation of θ_e or θ_l, especially longwave radiation cooling at the cloud top because it provides the major source in driving/maintaining the turbulent motion, as discussed in Section 5.

For cloudy PBLs, in addition to the vertical fluxes of momentum, heat, moisture or other scalars, turbulence statistics, such as temperature and moisture variances and covariance ($\overline{\theta_e^2}$, $\overline{q_T^2}$, and $\overline{\theta_e q_T}$) may also be important. According to Sommeria-Deardorff's (Sommeria and Deardorff 1977; JAS, 34, 344–355) subgrid-scale condensation scheme, these statistics determine the cloud amount and cloud fraction within, say, a GCM grid. This becomes one of the advantages of using higher-order closure modeling because other PBL models do not attempt to model these thermodynamic statistics.

6.1.6 Examination of closure assumptions and constants

In the above-mentioned closure assumptions, many closure constants are left to be determined empirically. Traditionally, wind tunnel (i.e., pure shear-driven) turbulence data were used to calibrate those constants. However, shear-driven turbulence is quite different from buoyancy-driven turbulence, and hence any closure that was "tuned" to shear turbulence is unlikely to work well for convective turbulence. An alternative is to use large-eddy simulation flows as database to calibrate closure assumptions (or constants) for buoyancy-driven PBLs. I will show some examples below.

- Pressure-scalar covariance

A closure problem for the pressure-scalar covariance term, $\frac{1}{\rho_0}\overline{c\partial p/\partial z}$ appears in the scalar-flux equation:

$$\frac{\partial \overline{wc}}{\partial t} = -\frac{\partial \overline{w^2 c}}{\partial z} - \overline{w^2}\frac{\partial C}{\partial z} + \frac{g}{T_0}\overline{\theta c} - \frac{1}{\rho_0}\overline{c\frac{\partial p}{\partial z}}, \tag{79}$$

where c is a scalar. To examine such closure, Moeng and Wyngaard (1986; JAS, 43, 2499–2513) divided the pressure fluctuations into five components, p_T, p_S, p_B, p_C, and P_{SG}, according to the four physical processes that appear on the right-hand side of the pressure Poisson equation,

$$\frac{1}{\rho_0}\nabla^2 p = -\frac{\partial}{\partial x_i}(\vec{V}'' \cdot \nabla u_i'') - 2(\frac{\partial U}{\partial z}\frac{\partial w}{\partial x} + \frac{\partial V}{\partial z}\frac{\partial w}{\partial y}) + \frac{g}{T_0}\frac{\partial \theta}{\partial z} + f(\frac{\partial u}{\partial x} - \frac{\partial v}{\partial y}) + SGS, \tag{80}$$

plus the subgrid-scale contribution in LES. The five components are defined as:

$$\frac{1}{\rho_0}\nabla^2 p_T = -\frac{\partial}{\partial x_i}(\vec{V}'' \cdot \nabla u_i''), \tag{81}$$

$$\frac{1}{\rho_0}\nabla^2 p_S = -2(\frac{\partial U}{\partial z}\frac{\partial w}{\partial x} + \frac{\partial V}{\partial z}\frac{\partial w}{\partial y}), \tag{82}$$

$$\frac{1}{\rho_0}\nabla^2 p_B = \frac{g}{T_0}\frac{\partial \theta}{\partial z}, \tag{83}$$

$$\frac{1}{\rho_0}\nabla^2 p_C = f(\frac{\partial u}{\partial x} - \frac{\partial v}{\partial y}), \tag{84}$$

$$\frac{1}{\rho_0}\nabla^2 p_{SG} = -\frac{\partial^2 \tau_{ij}}{\partial x_i \partial x_j}, \tag{85}$$

where p_T comes from the nonlinear turbulence-turbulence interaction, p_S from mean shear, p_B from buoyancy, and p_C from Coriolis term.

Separating the total pressure fluctuations into five components makes it easier to formulate closure hypothesis for each component, as we can see in the following. For example, for the buoyancy effect, we Fourier-transform (83) to

$$-\frac{\kappa^2}{\rho_0}\tilde{p_B}(\kappa) = \frac{g}{T_0}(i\kappa_z)\tilde{\theta}(\kappa), \tag{86}$$

where $i = \sqrt{-1}$, and $\tilde{}$ represents quantities in Fourier space. Dividing both sides by κ^2, multiplying by $i\kappa_z$ and the complex conjugate of $\tilde{c}$, and then Fourier transforming the equation back to the physical space, we obtain

$$-\frac{1}{\rho_0}\overline{c\frac{\partial p_B}{\partial z}} = -\frac{g}{T_0}\int(\frac{\kappa_z^2}{\kappa^2})\tilde{\theta}(\kappa)\tilde{c}^*(\kappa)d\kappa, \tag{87}$$

which can then be written as

$$-\frac{1}{\rho_0}c\overline{\frac{\partial p_B}{\partial z}} = A\frac{g}{T_0}\overline{\theta c},$$ (88)

where A is a constant depending on κ_z/κ. If the turbulence is isotropic, $A = 1/3$. However, the convective PBL turbulence is hardly isotropic. Based on their LES results, Moeng and Wyngaard found that $A \sim 1/2$ for the highly convective PBL.

The LES results also indicated that in the highly convective PBL, only two components dominate: p_T and p_B. We just showed that the latter component can be parameterized as (88). The nonlinear interaction term, p_T-component, represents the slow part of the pressure effect, i.e., Rotta's return-to-isotropy, thus can be written as

$$-\frac{1}{\rho_0}c\overline{\frac{\partial p_T}{\partial z}} = -\frac{\overline{wc}}{\tau},$$ (89)

where τ is a return-to-isotropy time scale. Moeng and Wyngaard's LES included four scalar fields, and hence the time scale τ (normalized by w_*/z_i) can be calculated from these four scalar fields separately. As shown in Fig. 6.6, time scales calculated from three nearly-bottom-up scalars (c_y, c_b, and θ, which have a surface flux much larger than the entrainment flux) have about the same shape, but that calculated from a top-down scalar, c_r, has a different distribution. This reflects an asymmetric property between top-down and bottom-up statistics.

In summary, the pressure-scalar term in the scalar flux equation for the highly convective PBL can be parameterized as

$$-\frac{1}{\rho_0}c\overline{\frac{\partial p}{\partial z}} \sim -\frac{1}{\rho_0}c\overline{\frac{\partial p_T}{\partial z}} - \frac{1}{\rho_0}c\overline{\frac{\partial p_B}{\partial z}} \sim -\frac{\overline{wc}}{\tau} + \frac{1}{2}\frac{g}{T_0}\overline{\theta c}.$$ (90)

• Turbulent transport term

Next we will examine a commonly-used closure scheme for the turbulent transport term in the TKE equation, as demonstrated by Moeng and Wyngaard (1989; JAS, 2311–2330). The TKE equation is:

$$\frac{\partial E}{\partial t} = -[\overline{uw}\frac{\partial U}{\partial z} + \overline{vw}\frac{\partial V}{\partial z}] + \frac{g}{T_0}\overline{w\theta_v} - \frac{\partial \overline{wE}}{\partial z} - \frac{\partial \overline{wp}}{\partial z} + \epsilon.$$ (91)

The turbulent transport term $-\partial\overline{wE}/\partial z$ is commonly parameterized as downgradient diffusion,

$$\frac{\partial \overline{wE}}{\partial z} = -\frac{\partial}{\partial z}(L_1 q \frac{\partial E}{\partial z}),$$ (92)
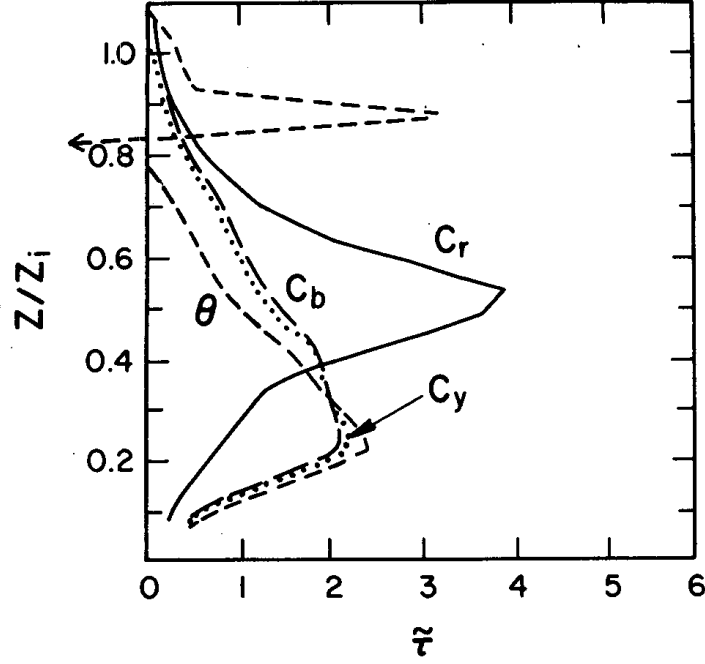
Figure 6.6 (SOURCE: Moeng and Wyngaard 1986)

where L_1 is a length scale. To see how good this closure assumption is, we analyzed the budget of $\overline{wE}$,

$$\frac{\partial \overline{wE}}{\partial t} = -(\overline{uw^2}\frac{\partial U}{\partial z} + \overline{vw^2}\frac{\partial V}{\partial z}) - (\overline{uw}\frac{\partial \overline{uw}}{\partial z} + \overline{vw}\frac{\partial \overline{vw}}{\partial z}) - \overline{w^2}\frac{\partial E}{\partial z} - \overline{w^2}\frac{\partial \overline{w^2}}{\partial z} - \frac{g}{T_0}(\overline{\theta E} + \overline{w^2\theta}) + P + M, \tag{93}$$

where P and M terms are the pressure-related and molecular terms, and are the major sink in this budget. They can be expressed as

$$P + M \sim -\frac{\overline{wE}}{\tau_1}, \tag{94}$$

where τ_1 is another time scale. The downgradient diffusion assumption given in (92) implies that the only term in (93) to balance the major sink of $P + M$ is the third term on the right-hand side of (93). In other words, if

$$\overline{w^2}\frac{\partial E}{\partial z} \sim -\frac{\overline{wE}}{\tau_1}, \tag{95}$$

then

$$\overline{wE} \sim -\overline{w^2}\tau_1\frac{\partial E}{\partial z}. \tag{96}$$

126
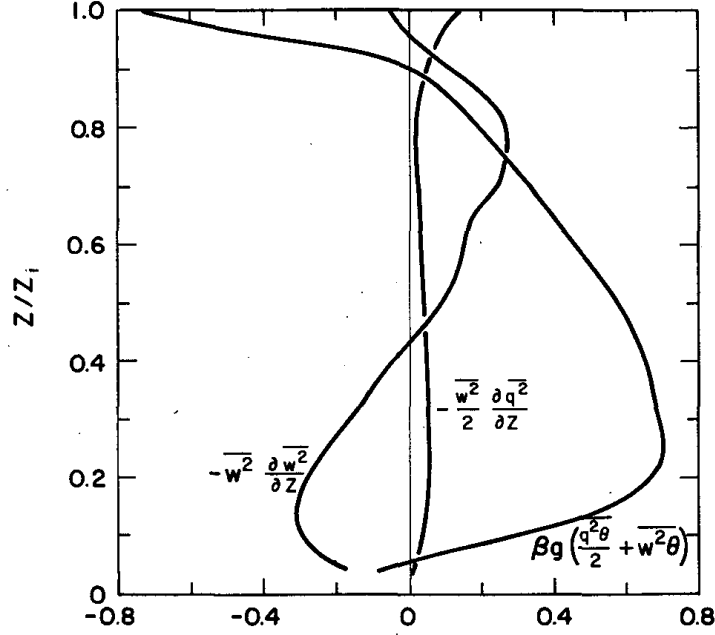
Figure 6.7 (SOURCE: Moeng and Wyngaard 1989)

We computed each term on the right-hand side of (93) based on the LES solution and plotted the dominant terms in Fig. 6.7. It is clear that the third term is not large; instead the buoyancy term provides the dominant source to $\overline{wE}$.

This explains why Mellor-Yamada's scheme greatly underestimated the turbulent transport term in the TKE budget for the CBL, as revealed in Fig. 6.2. Using the downgradient diffusion assumption for $\overline{wE}$ gives a negligibly small amount of $\overline{wE}$ everywhere in the PBL, hence a small turbulent transport term in the TKE budget (although they may argue that the 'diffusion' term they parameterize with the downgradient assumption is the sum of the turbulent and pressure transport terms, which is then much smaller than each transport term alone). In Zeman and Lumley's second-order closure scheme, the buoyancy effect in (93) was included in parameterizing the turbulent transport, and hence the model produced a more realistic $\overline{wE}$ distribution as shown in Fig. 6.4. A simple empirical modification to the down-gradient diffusion assumption for TKE model was proposed by Therry and Lacarrere (1983; BLM, 25, 63–88) based on the results from a 3rd-order closure model; their modification provides a better TKE budget in the CBL.

The same analysis and arguments apply to other third-moment flux terms, such as $\overline{w^2 c}$
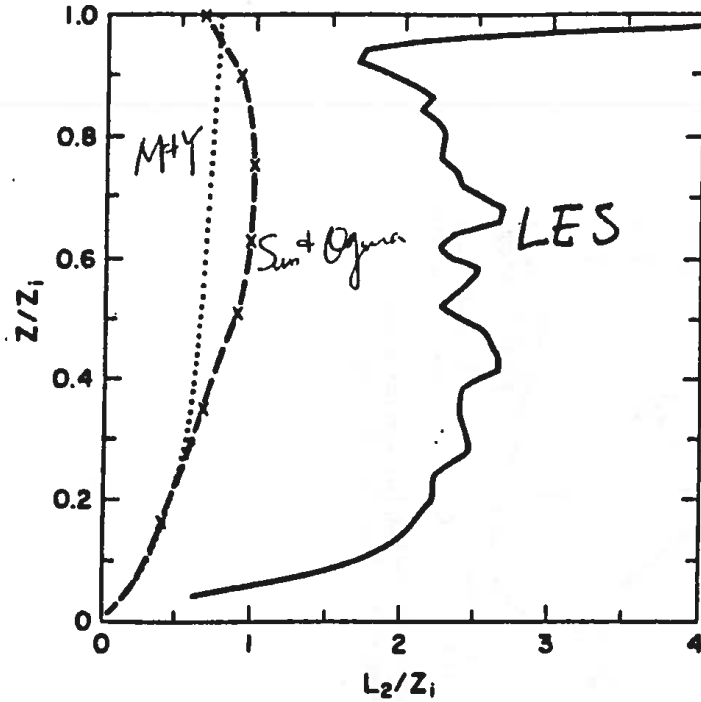
Figure 6.8 (SOURCE: Moeng and Wyngaard 1989)

and $\overline{wc^2}$.

• Molecular dissipation

Based on the inertial-range theory, the molecular dissipation rate depends on the amount of TKE cascades down from large eddies. Thus, the dissipation rate depends on large-eddy properties and is often expressed as

$$\epsilon = \frac{q^3}{L_2} = \frac{(2E)^{3/2}}{L_2}, \tag{97}$$

where q and L_2 are characteristic velocity and length scales of large eddies. The closure problem is determining the length scale L_2.

Using LES flows, Moeng and Wyngaard (1989) computed ϵ and E in (97) to determine L_2. The result is given in Fig. 6.8, and compared to those from Mellor-Yamada (1974) and Sun and Ogura (1980; JAS, 37, 1558–1572). Both second-order schemes use a length scale that is a factor of 2-3 smaller than that predicted by the LES.

So what is the consequence of using a smaller length scale in the dissipation rate formula (97)? By vertically integrating the TKE equation, we obtained a balance between the
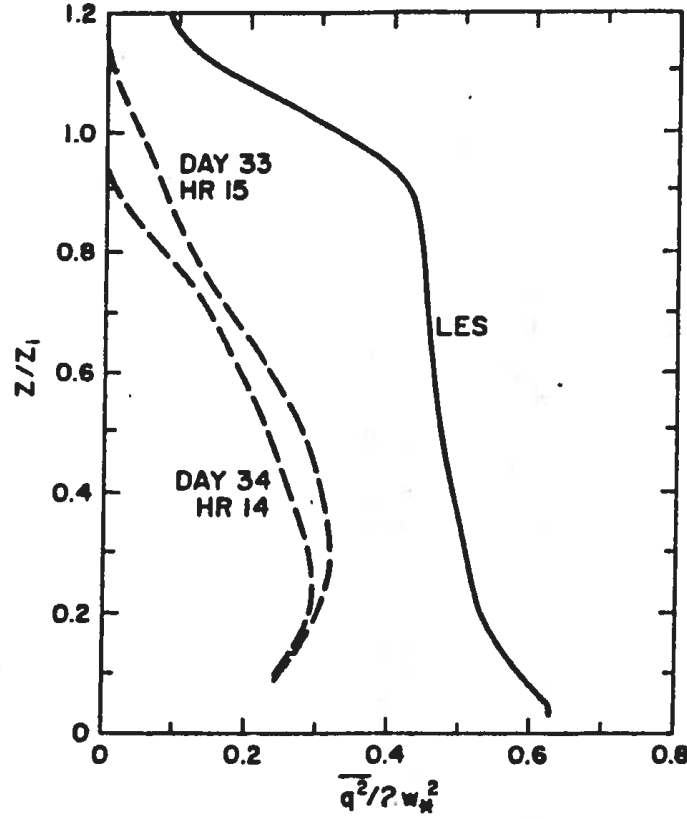
Figure 6.9 (SOURCE: Moeng and Wyngaard 1989)

vertically-integrated molecular dissipation and buoyancy production for the buoyancy-driven PBL when shear is negligibly small [Section 3.2]. Thus, the layer-averaged dissipation rate is fixed by the amount of buoyancy flux input from the surface. According to (97), if a closure model uses an L_2 that is too small by a factor of 3, it would produce an averaged TKE too small by a factor of 2, for a given surface buoyancy flux. That is what we observed in Fig. 6.9 when we compared the normalized TKEs calculated from LES and from the results of Yamada and Mellor (1975).

Homework 4:

Derive the formulae of eddy viscosity and eddy diffusivity in the Mellor-Yamada's Level 2 model.

129

6.2 Richardson-number-dependent K model

The K-model approach is sometimes called first-order closure modeling, in which the fluxes of momentum, heat, and other scalars are related to the vertical gradients of the mean fields with a prescribed eddy viscosity K_M and eddy diffusivity K_H:

$$\overline{uw} = -K_M \frac{\partial U}{\partial z}, \tag{98}$$

$$\overline{vw} = -K_M \frac{\partial V}{\partial z}, \tag{99}$$

$$\overline{w\theta} = -K_H \frac{\partial \Theta}{\partial z}. \tag{100}$$

The simplest K-model sets K_M and K_H to constant, assuming that turbulent motions transport or diffuse just like molecular motions. Of course this treatment of turbulence is naive and should not be used at all.

A K model, which describes K_M and K_H as functions of the Richardson number, was developed by Louis (1979; BLM, 17, 187–202) for the ECMWF medium-range forecast model. The scheme was based on an extension of surface-layer similarity, as described in the following. In Section 2 we learned that within the surface layer the mean wind speed and temperature at any height z can be expressed as

$$|\vec{V}(z)| = \frac{u_*}{\kappa}[\ln \frac{z}{z_0} - \Psi_1(\frac{z}{L})], \tag{101}$$

$$\Theta(z) - \Theta_0 = \frac{0.74\theta_*}{\kappa}[\ln \frac{z}{z_0} - \Psi_2(\frac{z}{L})], \tag{102}$$

for the unstable case, where Ψ_1 and Ψ_2 are stability functions, $|\vec{V}(z)| = \sqrt{U(z)^2 + V(z)^2}$, and

$$L \equiv \frac{\theta_0}{g} \frac{u_*^2}{\kappa \theta_*} \tag{103}$$

is the M-O length scale.

The stability (i.e., z/L) dependence in (101) and (102) can become Richardson-number dependence by first substituting (101) and (102) into (103), which leads to a relationship between z/L and R_{iB}:

$$R_{iB} = 0.74(\frac{z}{L}) \frac{[\ln(z/z_0) - \Psi_2(z/L)]}{[\ln(z/z_0) - \Psi_1(z/L)]^2}, \tag{104}$$

where the bulk Richardson number of the surface layer is defined as

$$R_{iB} \equiv \frac{g}{\theta_0} \frac{z(\Theta - \Theta_0)}{|\vec{V}|^2}. \tag{105}$$

Using this relationship, (101) and (102) can be rewritten as

$$\overline{uw}_0 \equiv -u_*^2 \cos\alpha_0 = \{C_{DN} F_m(\frac{z}{z_0}, R_{iB})\} \; |\vec{V}| U(z), \tag{106}$$

$$\overline{vw}_0 \equiv -u_*^2 \sin\alpha_0 = \{C_{DN} F_m(\frac{z}{z_0}, R_{iB})\} \; |\vec{V}| V(z), \tag{107}$$

$$\overline{w\theta}_0 \equiv -u_*\theta_* = \{\frac{C_{DN}}{0.74} F_h(\frac{z}{z_0}, R_{iB})\} \; |\vec{V}|(\Theta(z) - \Theta_0), \tag{108}$$

where $C_{DN}[\equiv \kappa^2/(\ln\frac{z}{z_0})^2]$ is the drag coefficient under neutral conditions, and the quantities inside the brackets are the surface drag coefficients C_D and C_H, which are now Richardson-number dependence. (α_0 is the angle between the surface wind and the x axis.)

Using Businger's empirical formulae for Ψ_1 and Ψ_2 and (101)–(108), Louis numerically computed $C_{DN}F_m$ and $(\frac{C_{DN}}{0.74})F_h$ in terms of R_{iB} for several z/z_0 as shown in Fig. 6.10 and proposed the following formulae to fit the curves:

$$F_{m,h} = 1 - \frac{bR_{iB}}{1 + c|R_{iB}|^{1/2}} \quad \text{for the unstable case,} \tag{109}$$

and

$$F_{m,h} = \frac{1}{(1 + b'R_{iB})^2} \quad \text{for the stable case,} \tag{110}$$

where $b = 2b' = 9.4$ and $c = C_* C_{DN} b(z/z_0)^{1/2}$ with $C_* = 7.4$ for momentum (for F_m) and $C_* = 5.3$ for scalar fluxes (for F_h). The above formulae are used *in the surface layer* to compute the surface fluxes.

Above the surface layer, the flux-gradient relationships (98)–(100) apply, and the K_M and K_H there are assumed to have the same Richardson-number-dependence as the surface-flux relationship, i.e.,

$$K_M = \ell^2 |\frac{\Delta\vec{V}}{\Delta z}| F_m(R_i), \tag{111}$$

$$K_H = \frac{1}{0.74} \ell^2 |\frac{\Delta\vec{V}}{\Delta z}| F_h(R_i). \tag{112}$$

131
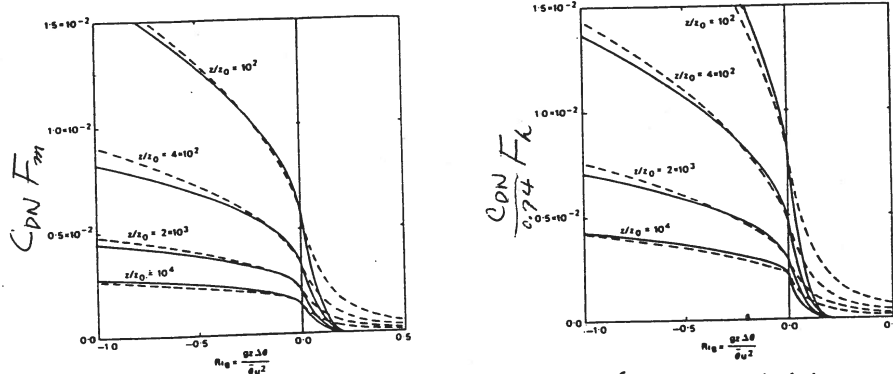
Figure 6.10 (SOURCE: Louis 1979)

Here $\ell^2|\Delta\vec{V}/\Delta z|$ is added to give the right units for K_M and K_H, and $|\Delta\vec{V}/\Delta z|$ is a discrete form of $|\partial\vec{V}/\partial z|$. Above the surface layer, the Richardson number is given as

$$R_i = \frac{g}{\Theta_0}\frac{\Delta z\Delta\Theta}{(\Delta\vec{V})^2}, \tag{113}$$

which is the gradient Richardson number in discrete form. The constant c in (109) now becomes

$$c = C^*\frac{\ell^2 b\{[(z+\Delta z)/z]^{1/3}-1\}^{3/2}}{z^{1/2}\Delta z^{3/2}}. \tag{114}$$

The length scale ℓ in (111), (112) and (114) is computed from the Blackadar formula,

$$\ell = \frac{\kappa z}{1+\frac{\kappa z}{\ell_0}}, \tag{115}$$

but here ℓ_0 is treated simply as an adjustable parameter. As it turns out, the Louis model are very sensitive to the specification of ℓ_0, especially near the PBL top. Louis proposed $\ell_0 = 100$ m in his 1979 paper, but later changed it to 150 m for momentum flux and 450 m for heat flux (Louis et al. 1981; ECMWF Workshop on Planetary Boundary Layer Parameterization, 25–27 November).

6.3   *K-profile model*

The *K-profile modeling* approach differs from the Richardson-number-dependent K approach in that the vertical distribution of K_M (or K_H) in the former is prescribed while in the latter is internally determined—by the local wind and temperature gradients—as shown in (111)-(113). The shape of K is often assumed to take the form of $z(1-z/z_i)^p$, which approaches

132

zero at the surface and at the PBL top z_i. This cubic shape of K profile was used by O'Brien (1970; JAS, 27, 1213–1215). A more advanced K-profile model was developed by Troen and Mahrt (1986; BLM, 37, 129–148), which was modified and implemented into the NCAR climate model CCM3 by Holtslag and Boville (1993; J. Climate, 6, 1825–1842). The eddy viscosity of Troen and Mahrt's model is expressed as

$$K_M = \kappa \; w_s \; z \; (1 - z/z_i)^2 \tag{116}$$

where κ is the von Karman constant. Even though the shape of eddy viscosity is fixed just like O'Brien's K model, its magnitude depends on a velocity scale w_s which depends on the sources of the turbulence.

For the stable PBL, eddy viscosity depends mainly on the surface wind stress, thus Troen and Mahrt wrote

$$w_s = u_*/\phi_m, \tag{117}$$

following Brost and Wyngaard (1978), where $\phi_m = 1 + 4.7z/L$ from Businger et al. (1971). This formula is consistent with surface-layer similarity because $K_M = u_* \kappa z/\phi_m$ for $z << z_i$.

For the unstable PBL, eddy viscosity depends on both wind stress and surface buoyancy flux, thus Troen and Mahrt proposed

$$w_s = (u_*^3 + c_1 w_*^3)^{1/3}, \tag{118}$$

where c_1 is set to 0.28 in Troen and Mahrt (1986) based on Businger's empirical formula of ϕ_m and w_* is the convective velocity scale, which is a measure of surface buoyancy forcing.

To use the K formula (116), we need to know the PBL height z_i. Troen and Mahrt proposed the following formula for the PBL height:

$$z_i = R_{ic} \frac{T_0}{g} \frac{|\vec{V}(z_i)|^2}{\Theta_v(z_i) - \Theta_s}, \tag{119}$$

where $\vec{V}(z_i)$ and $\Theta_v(z_i)$ are the mean wind and virtual potential temperature at the PBL top; the critical Richardson number R_{ic} is set to 0.5 in their study; and Θ_s is the virtual temperature near the surface, defined as

$$\Theta_s = \Theta_v(z_1) \qquad \text{for the stable PBL} \tag{120}$$
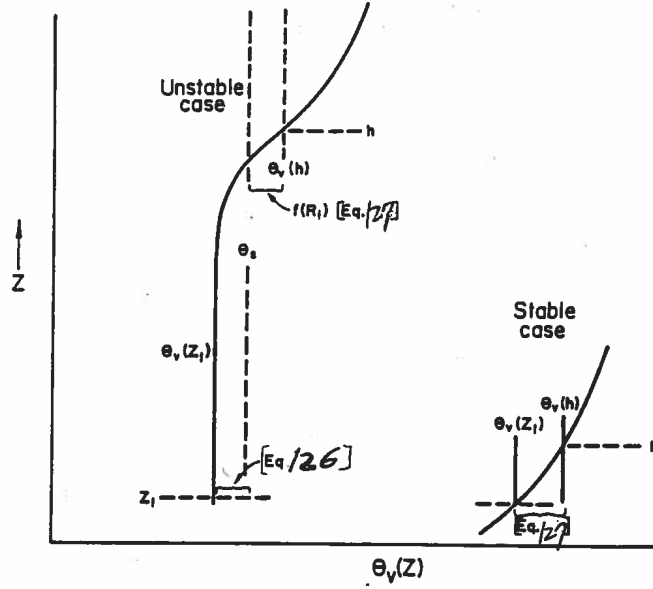
Figure 6.11 (SOURCE: Troen and Mahrt 1986)

and

$$\Theta_s = \Theta_v(z_1) + C\frac{\overline{w\theta}_0}{w_s} \qquad \text{for the unstable PBL.} \tag{121}$$

Here C is a constant, set to 6.5, w_s is given in (118), and $\Theta_v(z_1)$ is the virtual potential temperature at the first grid level z_1 (which has to be inside the surface layer).

To show the physical aspect of how z_i is defined, Troen and Mahrt rewrite (119) as

$$\Theta_v(z_i) = \Theta_s + R_{ic}\frac{T_0}{g}\frac{|\vec{V}(z_i)|^2}{z_i}. \tag{122}$$

This, along with Fig. 6.11, describes how the PBL top is obtained. For the unstable PBL, the surface virtual temperature Θ_s is computed from (121), thus depends on the surface heat flux $\overline{w\theta}_0$. The PBL top is then where the virtual potential temperature equals to Θ_s [first term in (122)], plus a modification due to the effect of wind at that height [second term in (122)]. For the stable PBL, $\Theta_s = \Theta_v(z_1)$, hence z_i is at the height where virtual potential temperature exceeds $\Theta_v(z_1)$ by $R_{ic}\frac{T_0}{g}\frac{|\vec{V}(z_i)|^2}{z_i}$ amount. In other words, the stable PBL top is where the bulk Richardson number $R_i \equiv \frac{g}{T_0}\frac{z_i(\Theta_v(z_i)-\Theta_v(z_1))}{|\vec{V}(z_i)|^2}$ reaches its critical value R_{ic}.

For scalar fluxes, Troen and Mahrt added a countergradient term to the K formula:

$$\overline{wc} = -K_H(\frac{\partial C}{\partial z} - \gamma), \tag{123}$$

134

where $\gamma = C\overline{wc}_0/(z_i w_s)$ and $C = 6.5$. Note that this countergradient term does not reduce to zero in neutral or stable conditions when the surface heating vanishes. Holtslag and Moeng (1991) modified this term to $\gamma \propto w_*\overline{wc}_0/(\overline{w^2}z_i)$ which reduces to zero when the surface heating vanishes.

To relate K_H to K_M, Troen and Mahrt proposed the following formula for the eddy Prandtl number

$$P_r \equiv \frac{K_M}{K_H} = \frac{\phi_h}{\phi_m} + \kappa\frac{z_r}{z_i}C,$$
(124)

which is obtained by matching the surface fluxes computed from a) their K formulae and from b) surface similarity theory at the top of the surface layer $z_r = 0.1\ z_i$.

Based on the above K-profile model, Large at al. (1994, Rev. Geophys., 32, 363-403) developed the KPP (K-Profile Parameterization) model for the ocean mixed layer, which is used in the NCAR's ocean GCM.

Homework 5:

Build a 1D PBL modeling code using the Louis' K model, and later using the K-profile model. The initial Θ profile is 300.+Γz, where the lapse rate Γ is assumed to be 3K/km and set the surface buoyancy flux to be 0.2 K m/s. Assume no mean wind.

6.4   *The mixed-layer (bulk) modeling*

A mixed-layer model is also called a bulk model. This modeling framework is drastically different from the multi-layer modeling approaches mentioned above. The PBL is treated as a single bulk layer in GCMs or mesoscale models. The formulae in the bulk model solve for the *layer-averaged* mean wind and mean potential temperature, U_m, V_m, Θ_m—averaged over the entire PBL (see below); a mixed-layer model provides *no* information on the vertical distributions of the mean fields.

The basis of mixed-layer modeling is the following. In a buoyancy-driven PBL (i.e., Convective Boundary Layer, CBL), the mean wind speed and conserved scalar quantities are often well mixed in height *above* the surface layer—as a result of strong turbulent mixing. The mixed-layer approach assumes that turbulent mixing is so rigorous that all conserved
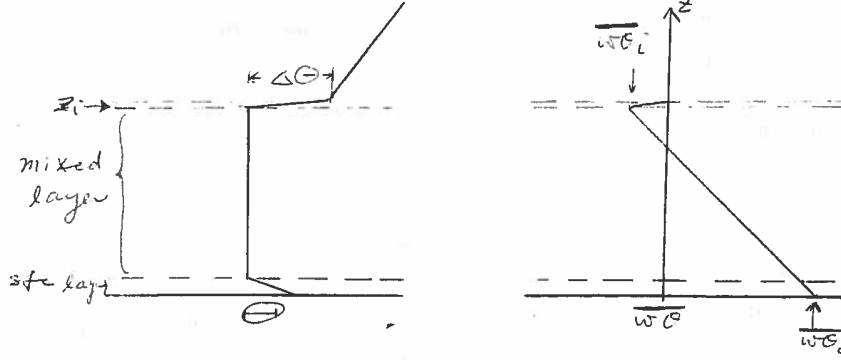
Figure 6.12

variables are always well mixed above the surface layer. This assumption is reasonable only for the CBL (with or without clouds), but not for shear-driven PBLs.

In the mixed-layer framework, the whole PBL consists of three layers: the surface layer, the well-mixed layer, and the entrainment zone, as sketched in Fig. 6.12. [Here we will assume the top of the surface layer matches the bottom of the mixed layer, although Santoso and Stull (1998, JAM, p545) showed some observational evidence that there exists a 'radix layer' in between.] For simplicity, we will use the clear-air CBL as an example to describe the framework of a mixed-layer model. For cloudy PBLs, radiation heating or cooling should be included as heat source or sink in the thermodynamic budget.

6.4.1 Model framework

Vertically integrating the equations of the mean U, V, and Θ from the surface to z_i yields the equations for the PBL-averaged mean fields:

$$\frac{\partial U_m}{\partial t} = \frac{1}{z_i}(\overline{uw}_0 - \overline{uw}_i) + f(V_m - V_{gm}), \tag{125}$$

$$\frac{\partial V_m}{\partial t} = \frac{1}{z_i}(\overline{vw}_0 - \overline{vw}_i) + f(U_{gm} - U_m), \tag{126}$$

$$\frac{\partial \Theta_m}{\partial t} = \frac{1}{z_i}(\overline{w\theta}_0 - \overline{w\theta}_i), \tag{127}$$

Here $\phi_m \equiv \frac{1}{z_i} \int_0^{z_i} \phi dz$ where $\phi = U$, V, or Θ; z_i is the PBL depth; U_{gm} and V_{gm} are vertically-averaged geostrophic winds; and fluxes with subscripts 0 and i are the surface fluxes and entrainment fluxes, respectively. Note there is no height dependence in these equations.

136

Since the surface layer is thin compared to the mixed layer, the mean value within the well-mixed layer can be approximated as ϕ_m. Equations (125)-(127) can be solved if the fluxes at the surface and at the top, as well as z_i, are known.

The surface fluxes are typically calculated based on surface-layer M-O similarity (again assuming the top of the surface layer matches the bottom of the mixed layer):

$$\overline{uw}_0 = -C_D|\vec{V}_m|U_m, \tag{128}$$

$$\overline{w\theta}_0 = -C_H|\vec{V}_m|(\Theta_m - \Theta_0), \tag{129}$$

where C_D and C_H can be computed from the stability functions, given in Section 2.

With a zero-order jump condition—where the entrainment zone is assumed to be infinitesimally thin—the fluxes at the PBL top can be expressed as

$$\overline{w\phi}_i \sim -w_e \Delta\phi, \tag{130}$$

where $\Delta\phi \equiv \phi^+ - \phi_m$ is the jump across the PBL top, ϕ^+ is the mean value just above the PBL top and w_e the entrainment rate. Eq. (130) is called the *zero-order jump condition* derived by vertically integrating the equation of ϕ over a infinitesimally thin layer across the PBL top, i.e., from the top of the mixed layer to a level just above z_i where turbulence fluxes vanish (e.g., Lilly 1968; QJRMS, 94, 292–309).

However, in the time or spatial average sense, the entrainment zone is not infinitesimally thin. The local interface, which is usually quite abrupt, undulates in time and space due to turbulent motions. If a time or spatial averaging is used to define the overbar in (128)-(130), the entrainment zone should also be a layer averaged in the same way. Then the entrainment zone is the thickness of undulations of the PBL tops. If the capping inversion is weak and turbulence is rigorous, the undulations can be large, and so is the entrainment zone. Re-deriving (130) with a finite thickness of the entrainment zone would give more terms in (130) (including the heat budgets inside the zone), which leads to 1st-order jump condition. For example, for a clear-air CBL, the time-rate-of-change of the mean potential temperature within the entrainment zone appears on the right-hand-side of (130). Based on their LESs of weak inversion case, Sullivan et al. (1998; JAS, 55, 3042–3064) showed that this term is as large as the $-w_e\Delta\Theta$ term. For the stratocumulus-topped PBL, radiation heating or cooling inside the entrainment zone should also be included in (130).

Niewstadt and Businger (1984, QJRMS, 110, 1073-1078) and Lilly (2002, JAS, 59, 3340–3361) argued that 'ensemble average' can be seen as an average along a height coordinate based on the deformed local mixed layer height, $z(x, y, t)/z_{\text{top}}(x, y, t)$. With this definition the entrainment zone remains as abrupt as the local interface, and the zero-order jump condition (130) can still apply. But it is difficult, if not impossible, to use this hypothetical coordinate in analyzing the field data or LES flow fields.

Entrainment is not the only mechanism that determines the time change of the PBL depth. The large-scale vertical motion (lifting or subsiding) can also result in deepening or shallowing of the PBL. Thus, the time-rate-of-change of the PBL height is governed by

$$\frac{dz_i}{dt} = w_e + W_{LS}(z_i) \tag{131}$$

where w_e is the entrainment rate and $W_{LS}(z_i)$ is the large-scale (synoptic or mesoscale) vertical motion at z_i. If deep convection occurs, the mass flux into the cloud should also be included in (131).

You may wonder why anyone would use a PBL model that assumes no vertical structure of the mean fields. There are actually many pros of this approach for climate modeling purposes. First, it can maintain a distinct PBL with a sharp jump across the PBL top. This sharp jump condition is an important feature of the stratocumulus-topped PBL and affects the interaction of cloud-top processes such as entrainment, IR cooling, and evaporative cooling. Second, the entrainment rate is explicitly calculated from a formula, not implicitly incorporated through eddy diffusivity or TKE prediction. Third, the cloud-top radiative cooling effect, which is confined to a very thin layer at the cloud top, can be included in a more precise way in the mixed-layer modeling framework. Fourth, it is computationally cheap for climate models because it requires only one GCM layer. This scheme has been used (and only used) in the UCLA GCM and its descending versions. It is a lot more complicated in the implementation of this scheme in a GCM with a multi-layer framework.

The set of Eqs. (125)–(131) can be solved if the entrainment rate w_e is known. Therefore, an important closure problem for the mixed-layer approach is the so-called *entrainment closure*. (For modeling the stratocumulus-topped PBL, there involves more closure problems, such as that for cloud fraction.) Over the years, various entrainment closure assumptions have been proposed, some based on the PBL-averaged turbulent-kinetic-energy (TKE) bud-
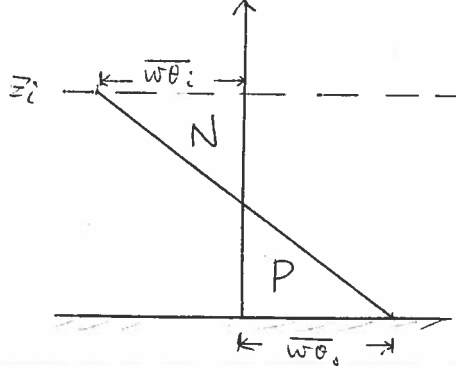
Figure 6.13

get, some based on the TKE budget in the entrainment zone, and some are purely empirical. Approaches based on the TKE budgets will be described in the next subsections.

6.4.2 Entrainment closure based on the TKE budget of the whole PBL

This type of entrainment closure approach was first proposed by Ball (1960; QJRMS, 86, 483–494) who hypothesized that the rate of TKE destruction by buoyancy forces associated with entrainment (N) balances the rate of TKE generated by surface heating (P) such that the vertically integrated buoyancy production term $(B = P - N)$ is zero, as illustrated in Fig. 6.13.

That is, $P = N$, where

$$P = \frac{g}{\Theta_0} \int_0^{z_i} \overline{w\theta}(\text{where } \overline{w\theta} > 0)dz, \tag{132}$$

and

$$N = -\frac{g}{\Theta_0} \int_0^{z_i} \overline{w\theta}(\text{where } \overline{w\theta} < 0)dz. \tag{133}$$

Thus, *if $P = N$ is assumed*, then

$$\overline{w\theta}_i = -\overline{w\theta}_0. \tag{134}$$

and

$$\frac{w_e}{w_*} = R_{i*}^{-1}, \tag{135}$$

where $R_{i*}(\equiv \frac{g}{\Theta_0}\frac{z_i\Delta\Theta}{w_*^2})$ is called an "overall buoyancy Richardson number (e.g., Deardorff 1980; BLM, 18, 495–527). Eqs. (134) and (135) are only true if $P = N$.

139

But we know that $P \neq N$ in the CBL. Lilly (1968) argued that the above assumption leads to the maximum entrainment rate because it neglects the TKE destruction due to molecular dissipation. If molecular dissipation is included, the TKE budget becomes $B - \epsilon = P - N - \epsilon = 0$. Assuming the molecular dissipation rate is proportional to the buoyancy production P as $\epsilon = (1 - A)P$ leads to $N = AP$, where the entrainment constant A is between 0 and 1, and the entrainment-rate formula becomes

$$\frac{w_e}{w_*} = AR_{i*}^{-1}. \tag{136}$$

The constant A is a parameter to be determined empirically. Observations of cloud-free, strongly convective PBLs have suggested that the entrainment buoyancy flux is about –0.2 of the surface buoyancy flux. Hence, $A \sim 0.2$ (Stull, 1976; JAS, 33, 1260–1267) and

$$\frac{w_e}{w_*} \sim 0.2 R_{i*}^{-1}. \tag{137}$$

It is important to note that the entrainment constant A is "tuned" to fit observations of the CBL regime, and hence the entrainment-rate formula (137) is expected to predict the growth of the cloud-free CBL height reasonably well. This formula has shown, not surprisingly, unsatisfactory when applied to other PBL regimes, such as the stratocumulus-topped PBL, e.g., Lilly (1968;QJRMS, 94, 292–309), Schubert (1976; JAS, 33, 436–446), Kraus and Schaller (1978; Tellus, 30, 84–88), and Randall (1984; JAS, 41, 402–413).

Another method in separating P and N was given by Stage and Businger (1981; JAS, 38, 2230–2242) based on physical processes. There, P is buoyancy production due to surface heating, which equals the surface buoyancy flux at the surface and linearly decreases to zero at the PBL top; while N represents buoyancy consumption due to entrainment, whose magnitude equals the entrainment buoyancy flux at z_i and decreases to zero at the surface. Randall (1984) compared the Stage-Businger's "Process Partitioning" to the "Eulerian Partitioning" given in (132) and (133), and showed that the two methods are the same for the clear-air CBL, but differ for the stratocumulus-topped PBL.

6.4.3 Entrainment closure based on the TKE budget in the entrainment zone

This type of entrainment closure is summarized in Tennekes and Driendonks (1981; BLM, 20, 515–531). The governing equation of the TKE in the entrainment zone, E_i, is

$$\frac{\partial E_i}{\partial t} = \frac{g}{\Theta_0}\overline{w\theta}_i - [\overline{uw}_i\frac{\Delta U}{d} + \overline{vw}_i\frac{\Delta V}{d}] - [\frac{\partial}{\partial z}(\overline{wE} + \frac{\overline{pw}}{\rho_0})_i] - \epsilon_i, \tag{138}$$

where d is an effective depth of the entrainment zone. The first term on the right hand side is buoyant production, second the shear production terms, followed by turbulent and pressure transport terms, and finally dissipation. In order to solve this equation, each term in (138) needs to be parameterized in terms of mixed layer parameters.

Although simpler parameterizations for the mixed layer height can be arrived at by setting the left hand side of (138) to zero, Zilitinkevich (1975) argued that when the mixed layer grows rapidly, this term cannot be neglected, and thus proposed

$$\frac{\partial E_i}{\partial t} = C_T\frac{w_t^2}{z_i}\frac{dz_i}{dt}, \tag{139}$$

where the turbulent velocity scale w_t is an interpolation between the friction velocity and the convective velocity,

$$w_t = (w_*^3 + 8.0u_*^3)^{1/3} \quad \text{for the unstable PBL}, \tag{140}$$

and

$$w_t = 2.0u_* \qquad \text{for the neutral PBL}, \tag{141}$$

after Zeman and Tennekes (1977; JAS, 34, 111–123).

Using (130) and a scaling argument that $\frac{\Delta U}{d} \propto \frac{\Delta U}{z_i}$, the shear production in (138) can be written as (assuming $W_{LS} = 0$),

$$-[\overline{uw}_i\frac{\Delta U}{d} + \overline{vw}_i\frac{\Delta V}{d}] = C_M\frac{(\Delta U)^2 + (\Delta V)^2}{z_i}\frac{dz_i}{dt}, \tag{142}$$

and after Tennekes (1973; JAS, 30, 558–567), the turbulent and pressure transport terms are parameterized as,

$$-\frac{\partial}{\partial z}(\overline{wE} + \frac{\overline{wp}}{\rho_0})_i = C_F\frac{w_t^3}{z_i}. \tag{143}$$

Although Tennekes and Driedonks (1981) point out that there is a substantial degree of arbitrariness in the choice of forms for the dissipation term, they choose,

$$\epsilon_i = C_D w_t^2 N, \tag{144}$$

where N is the bouyancy frequency of the air just above the PBL,

$$N^2 = \frac{g}{\Theta} \frac{\partial \Theta^+}{\partial z}. \tag{145}$$

Substituting (139), (142), (143), and (144) into (138) yields the following entrainment-rate formula,

$$\frac{dz_i}{dt} = \frac{\frac{g}{\Theta}\overline{w\theta}_i + C_F \frac{w_t^3}{z_i} - C_D w_t^2 N}{C_T \frac{w_t^2}{z_i} - C_M \frac{\Delta U^2 + \Delta V^2}{z_i}}, \tag{146}$$

where C_F, C_T, C_D and C_M are constants set to 0.6, 4.3, 0.03 and 0.7, respectively.

6.4.4 Entrainment closure for the stratocumulus-topped PBL

To apply the entrainment rate formulae (137) and (146) to the stratocumulus-topped PBL requires proper modifications to take into account the cloud-top radiative and evaporative cooling effects. For example, Deardorff (1980; BLM, 18, 495–527) modified (137), based on his LES, to include the cloud-top radiative cooling effect, as

$$\frac{w_e}{\sigma_w(z_i)} - 0.2\frac{(F_R)_2 - (F_R)_1}{\sigma_w(z_i)\Delta\Theta} = f(R_{i\sigma_w}), \tag{147}$$

where $(F_R)_2 - (F_R)_1$ is the jump of radiative flux across the PBL top, $\sigma_w(z_i)$ is the standard deviation of the vertical velocity at the z_i level, and $R_{i\sigma_w} = \frac{g}{\Theta_0}\frac{z_i\Delta\Theta}{\sigma_w(z_i)^2}$ is a modified Richardson number. Turton and Nicholls (1987, QJRMS, 113, 969–1009) considered the cloud-top evaporative cooling effect (i.e., buoyancy reversal effect) and suggested that the entrainment-rate formula (137) should also depend on $\Delta_m/\Delta\Theta_v$, a measure of the potential for evaporative cooling due to entrainment mixing at the interface, i.e.,

$$\frac{w_e}{w_*} = f(R_{i*}; \Delta_m/\Delta\Theta_v). \tag{148}$$

In addition to the above two entrainment-rate formulae, others have also been proposed (e.g., Lewellen and Lewellen, 1998, JAS, 55, 2645-2665; Lock, 1998, QJRMS, 124, 2729–2753;

Moeng, 2000, JAS, 57, 3627–3643), but the entrainment rate closure for the stratocumulus-topped PBL remains an unsolved problem (Stevens, et al. 2003, QJRMS, 129, 3469-3493).

Homework 6:

Re-derive the jump condition shown in (130) but without assuming that the entrainment zone is infinitesimally thin. Use Leibniz's rule.

6.5   *Transilient Turbulence Theory/Integral Closure Model*

Transilience theory was developed by Stull (1984; JAS, 41, 3351–3367), where transilience means "jump over" in Latin to represent the nonlocal mixing process of turbulent motion. Transilience theory is based on the fact that turbulent motion transports air mass through advection process, rather than diffusion process. The Reynolds stress term in the Reynolds equations (see derivation of the Reynolds equation in Section 1) is originated from the advection of fluctuative motions. This effect is evident in large-eddy simulations (more later) where air parcels are advected by large turbulent motions and this "advection" by large eddies accounts for most of the turbulent transport.

The framework of transilience theory is the following: The mean concentration of any scalar S at height i and time t can be modified by mixing with air parcels originating from any other levels within the PBL, j, which carry S_j amount of concentration. After mixing for a time period of Δt, S at level i becomes

$$S_i(t + \Delta t) = \Sigma_{j=1}^{j=N} c_{ij}(t, \Delta t) S_j(t), \tag{149}$$

where c_{ij} is called the transilience matrix. This nonlocal mixing process is illustrated in Fig. 6.14 using a five-vertical-grid configuration as an example. The transilience matrix c_{ij} represents the fraction of air mixing into the i grid from a source located at j grid. For example, the element c_{51} represents the fraction of air that is mixed into the $i = 5$th grid from the $j = 1$st level; this element thus represents a jump-over (nonlocal mixing) process. The element c_{21} represents mixing between the neighboring grid levels, i.e., from level 1 to level 2, and hence represents local mixing. Thus, for traditional local K models, only the tridiagonal elements in c_{ij} (where i and j are adjacent numbers) are non-zero. The diagonal
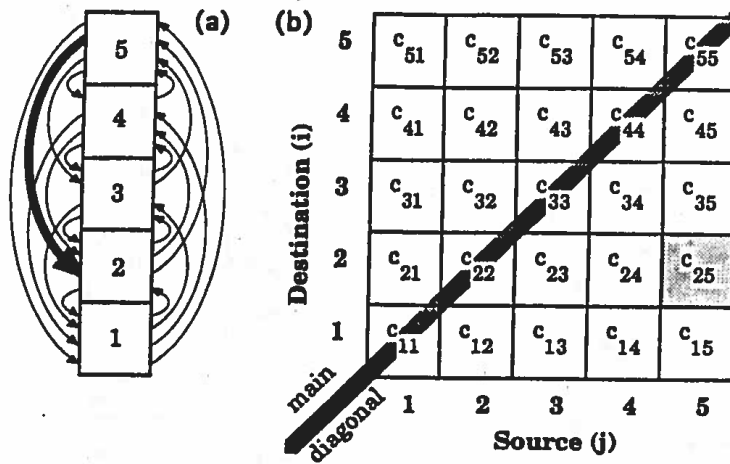
Figure 6.14 (SOURCE: Stull 1993)

elements of the matrix represent the fraction of air that is not from other levels. To satisfy conservation of air mass, each row and each column of c_{ij} must sum to 1, and each element lies between 0 and 1.

The most crucial closure problem of transilience theory is determining the transilience matrix c_{ij}. Stull and Driedonks (1987, BLM, 40, 209–239) proposed using the discretized form of the TKE budget to construct the matrix, while Ebert et al. (1989; JAS, 46, 2178–2207) used LES solutions to empirically determine the matrix. For the latter study, different tracers were released at all grid levels within a fully-developed turbulent LES flow (Fig. 6.15a), and after a finite time the amount of tracers exchanged between grid levels was measured to determine the transilience matrix, as described in Fig. 6.15b. For those who are interested in transilient turbulence theory, read Stull (1993; BLM, 62, 21–96), which provides a detailed review of the theory and the applications to weather forecast models and air pollution dispersion models.

The integral closure model developed by Fiedler (1984; JAS, 41, 674–680) and Fiedler and Moeng (1985; JAS, 42, 359–363), in its discrete form, is essentially the same as Stull's transilience theory.

The Blackadar scheme (Zhang and Anthes, 1982; JAM, 21, 1594–1609) used in the NCAR/Penn-State Mesoscale Model (MM5) is a simplified version of transilience theory. The Blackadar's model allows for any scalar originated from the surface to *directly* transport
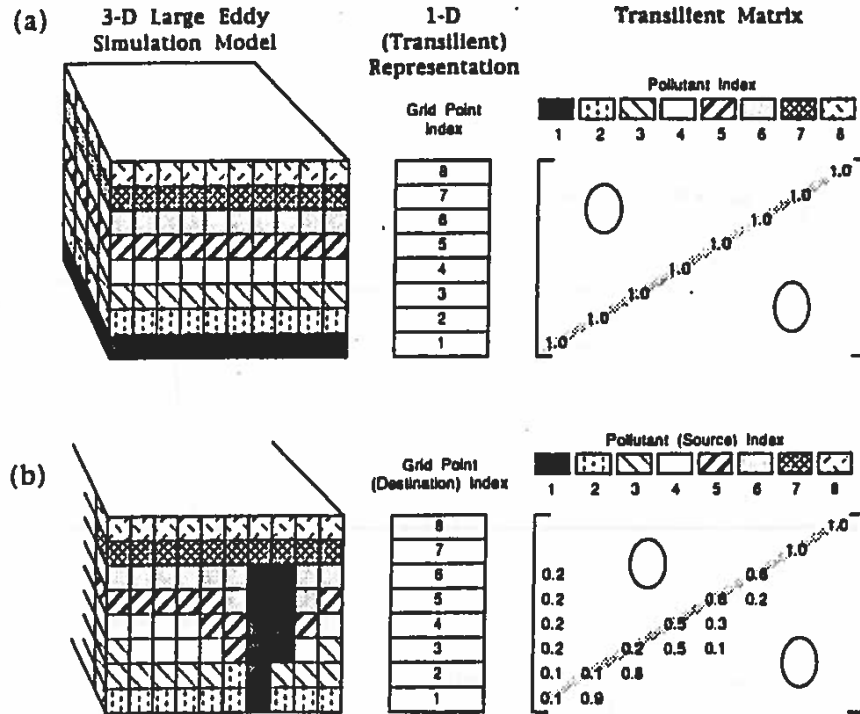
144

Figure 6.15 (SOURCE: Stull 1993)

to any levels above and scalar from the PBL top to directly transport to any levels below, as sketched in Fig. 6.16a. In terms of the transilience matrix, the Blackadar model has non-zero elements only for c_{i1} [where $j = 1$ stands for the surface layer and hence c_{i1} represents mixing from the surface up to each level i within the PBL] and c_{1j} [representing mixing from each level j down to the surface]. The model assumes that the upward mixing from the surface is symmetrical to the downward mixing from the PBL top.

This symmetrical mixing is not realized in the CBL, as we have learned about the top-down and bottom-up asymmetric diffusion. This deficiency was removed in the Asymmetrical Convective Model developed by Pleim and Chang (1992, Atmos. Environ., 26A, 965–981), which is probably used in the EPA air pollution model. This scheme assumes that downward mixing occurs only locally (i.e., from level i to level $i - 1$) while keeping upward mixing as nonlocal as the Blackadar model, as shown in Fig. 6.16b. It is a more physically based model.

The above schemes may be classified to a class of *multi-stream exchange models*; they
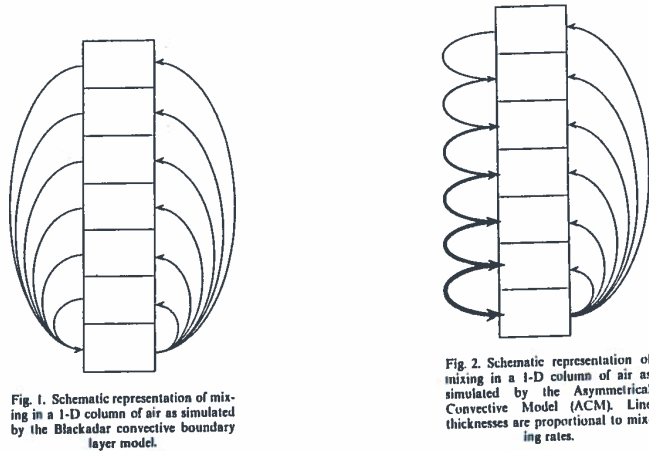
145

Fig. 1. Schematic representation of mixing in a 1-D column of air as simulated by the Blackadar convective boundary layer model.

Fig. 2. Schematic representation of mixing in a 1-D column of air as simulated by the Asymmetrical Convective Model (ACM). Line thicknesses are proportional to mixing rates.

Figure 6.16 (SOURCE: Pleim and Chang 1992)

allows for non-local mixing (or exchange) of species between any two grid levels.

6.6 *Mass flux model*

Convective mass flux modeling is based on the hypotheses that a) large eddies are responsible for most of the turbulent transport, and b) these large turbulent motions (e.g., thermals) can be represented by two branches of motion—updrafts and downdrafts. Under the mass flux representation, the total turbulent fluxes is related to the difference between the mean quantities of these two branches, as

$$\overline{wc} = \omega_c(C_U - C_D), \tag{150}$$

where $\omega_c = \sigma(1-\sigma)(w_U-w_D)$ is the mass flux, σ is the fractional area covered by updrafts, w_U and w_D are the mean vertical velocities averaged over updrafts and downdrafts, respectively, and C_U and C_D are the mean values of c averaged over updrafts and downdrafts. The mean concentration of c is

$$C = \sigma C_U + (1 - \sigma)C_D. \tag{151}$$

To use the mass-flux modeling require (1) determining the mass flux ω_c and (2) solving the budget equations of C_U and C_D separately.

Derivation of the budget equations for C_U and C_D and methods to solve these eqs. can be found in Wang and Albrecht (1990, JAS, 47, 126–138) or Siebesma and Holtslag (1996,

JAS, 53, 2354-2364). These eqs include lateral mixing (entrainment/detrainment) between the two branches, which is difficult to determine (Schumann and Moeng 1991, JAS, 48, 1758-1770).

On the other hand, Randall et al. (1992; JAS, 49, 1903–1923) analytically solved for the flux $\overline{wc}$ based on the variance budget (i.e., $\partial \overline{c^2}/\partial t$ eq.), which has a lower and a upper boundary conditions that match the fluxes at the surface and at the PBL top, respectively. This flux is then used to estimate C_U and C_D from (150) and (151).

For the vertical distribution of the mass flux ω_c, Wang and Albrecht (1990) assumed that the mass flux is related to the convective velocity scale w_* as $\omega_c = a\sigma w_*$, where σ (the area covered by updrafts) is assumed to be constant (between 0.15-0.45) with height and a is a proportionality constant (ranging from $0.3 \sim 2.0$). In their model, the profile of mass flux is uniform in height but the magnitude varies with the convective velocity scale w_*. Randall et al. (1992), on the other hand, determine the mass flux using the layer-averaged TKE, the entrainment mass flux, and the flux from the top of the surface layer as inputs.

Another way to determine the mass flux was proposed by Businger and Oncley (1990, JAOT, 7, 349–352), which assumes that the mass flux is proportional to the root-mean-square of vertical velocity, σ_w:

$$\omega_c = b\sigma_w, \tag{152}$$

which peaks at around $0.4z_i$ and decreases towards zero at the surface and the PBL top. The closure constant b is to be determined empirically. This $\omega_c - \sigma_w$ relationship was observed by Nicholls and LeMone's (1980) from the GATE data of PBLs underlying shallow cumulus clouds (see Section 5.2.2). Field measurements within the surface layer by Businger and Oncley, and the LES results from Wyngaard and Moeng (1992, BLM, 60, 1–13) and Moeng et al. (1992, JAS, 49, 2384–2401) suggested that the proportionality constant b in (152) is about 0.6 for almost all types of PBL, including clear convective PBL, stable PBL and stratocumulus-topped PBL.

Wyngaard and Moeng (1992) showed that the constant b in (152) can be analytically determined from the joint probability density of vertical velocity and scalar, $\beta(w,c)$. By definition,

$$\overline{wc} = \int_{-\infty}^{\infty} \int_{-\infty}^{\infty} wc\beta(w,c)dwdc, \tag{153}$$

$$\overline{w^2} = \int_{-\infty}^{\infty} \int_{-\infty}^{\infty} w^2 \beta(w,c) dw dc, \tag{154}$$

$$C_U = \frac{\int_0^{\infty} \int_0^{\infty} C\beta(w,C) dw dC}{\int_0^{\infty} \int_0^{\infty} \beta(w,C) dw dC}, \tag{155}$$

$$C_D = \frac{\int_0^{\infty} \int_{-\infty}^0 C\beta(w,C) dw dC}{\int_0^{\infty} \int_{-\infty}^0 \beta(w,C) dw dC}. \tag{156}$$

If the joint probability density is jointly Gaussian, we can show from (150), (152), (153), (154), (155) and (156) that

$$b = \frac{\sqrt{2\pi}}{4} = 0.627. \tag{157}$$

The mass-flux concept was invented for use in a cumulus parameterization by Arakawa in late 1960s, and is the basic framework for the Arakawa-Schubert scheme. The mass-flux modeling is also used to parameterize shallow cumulus in many GCMs (Tiedtke 1989, MRW, 117, 1779–1800). When the mass-flux framework is used as cumulus parameterization, the ω_c-σ_w relationship in (152) no longer applies, Typically, a mass conservation eq is used to solve for the convective mass flux.

6.7 *Hybrid modeling approach*

More and more modelers are combining two or three PBL modeling approaches into a hybrid model, hoping to use an unified framework for all PBL regimes. Recall that different PBL models function differently; for example, eddy-viscosity or higher-order closure models work better for shear-driven PBLs, mixed-layer models were designed specifically for the CBL and stratocumulus-topped PBLs, and mass-flux models seem to work well for shallow-cumulus-topped PBL. Thus, combining the best of each approaches may provide the best modeling framework.

Randall et al. (1992, JAS, 49, 1903–1923) combined the mass-flux and higher-order closure approaches into a bulk model framework in their Second-Order Bulk (SOB) model. Figure 6.17 summaries the framework and its relationship to cumulus parameterization. It is a rather complicated model. Students who like to challenge themselves are encouraged to read this paper.
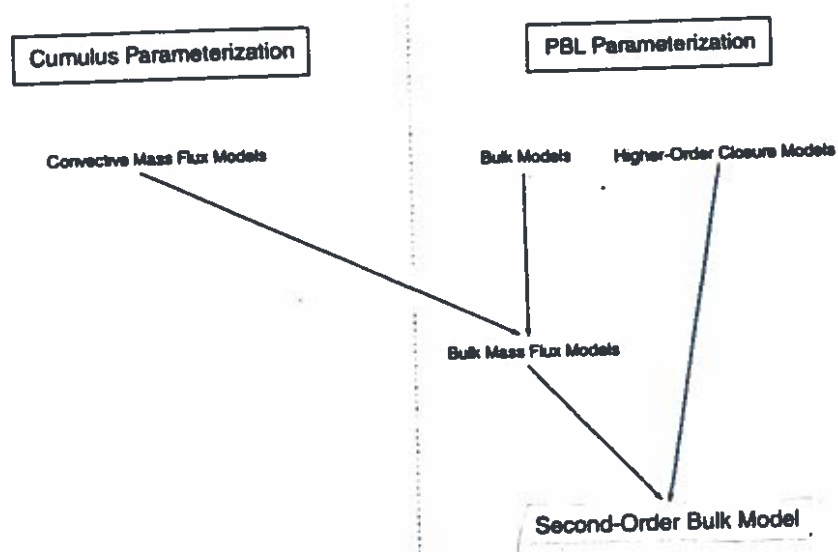
Figure 6.17 (SOURCE: Randall et al. 1992)

Recently, Siebesma et al (2007, JAS, 64, 1230-1248) combined the eddy diffusivity approach with the mass-flux approach for the CBL. The flux of a scalar is written as

$$\overline{wc} = -K\frac{\partial C}{\partial z} + M(C_U - C), \tag{158}$$

where M is the mass flux defined as $M \equiv \sigma(w_U - \overline{w}$, again σ is the fractional area covered by updrafts. This definition of M is the same as that defined in Section 6.6, i.e., $\omega_c = \sigma(1-\sigma)(w_U - w_D)$, because $\overline{w} = \sigma w_U + (1-\sigma)w_D$. Siebesma et al developed an updraft model to solve for w_U, Θ_U and Q_U.

APPENDIX: The Nature of Turbulence

Excerpt from pages 1-4 of H. Tennekes and J.L. Lumley: A First Course in Turbulence, 1972

"Everyone who, at one time or another, has observed the efflux from a smoke-stack has some idea about the nature of turbulent flow. However, it is very difficult to give a precise definition of turbulence. All one can do is list some of the characteristics of turbulent flows.

Irregularity *One characteristic is the irregularity, or randomness, of all turbulent flows. This makes a deterministic approach to turbulence problems impossible; instead, one relies on statistical methods.*

Diffusivity *The diffusivity of turbulence, which causes rapid mixing and increased rates of momentum, heat, and mass transfer, is another important feature of all turbulent flows. If a flow pattern looks random but does not exhibit spreading of velocity fluctuations through the surrounding fluid , it is surely not turbulent. The contrails of a jet aircraft are a case in point: excluding the turbulent region just behind the aircraft, the contrails have a very nearly constant diameter for several miles. Such a flow is not turbulent, even though it was turbulent when it was generated. The diffusivity of turbulence is the single most important feature as far as applications are concerned: it prevents boundary-layer separation on airfoils at large (but not too large) angles of attack, it increases heat transfer rates in machinery of all kinds, it is the source of the resistance of flow in pipelines, and it increases momentum transfer between winds and ocean currents.*

Large Reynolds numbers *Turbulent flows always occur at high Reynolds numbers. Turbulence often originates as an instability of laminar flows if the Reynolds number becomes too large. The instabilities are related to the interaction of viscous terms and nonlinear inertia terms in the equations of motion. This interaction is very complex: the mathematics of nonlinear partial differential equations has not been developed to a point where general solutions can be given. Randomness and nonlinearity combine to make the equations of turbulence nearly intractable; turbulence theory suffers from the absence of sufficiently powerful mathematical methods. This lack of tools makes all theoretical approaches to problems in*

turbulence trial-and-error affairs. Nonlinear concepts and mathematical tools have to be developed along the way; one cannot rely on the equations alone to obtain answers to problems. This situation makes turbulence research both frustrating and challenging: it is one of the principal unsolved problems in physics today.

Three-dimensional vorticity fluctuations *Turbulence is rotational and three dimensional. Turbulence is characterized by high levels of fluctuating vorticity. For this reason, vorticity dynamics plays an essential role in the description of turbulent flows. The random vorticity fluctuations that characterize turbulence could not maintain themselves if the velocity fluctuations were two dimensional, since an important vorticity-maintenance mechanism known as vortex stretching is absent in two-dimensional flow. Flows that are substantially two dimensional, such as the cyclones in the atmosphere which determine the weather, are not turbulence themselves, even though their characteristics may be influenced strongly by small-scale turbulence (generated somewhere by shear or buoyancy), which interacts with the large-scale flow. In summary, turbulent flows always exhibit high levels of fluctuating vorticity. For example, random waves on the surface of oceans are not in turbulent motion since they are essentially irrotational.*

Dissipation *Turbulent flows are always dissipative. Viscous shear stresses perform deformation work which increases the internal energy of the fluid at the expense of kinetic energy of the turbulence. Turbulence needs a continuous supply of energy to make up for these viscous losses. If no energy is supplied, turbulence decays rapidly. Random motions, such as gravity waves in planetary atmospheres and random sound waves (acoustic noise), have insignificant viscous losses and, therefore, are not turbulent. In other words, the major distinction between random waves and turbulence is that waves are essentially nondissipative (though they often are dispersive), while turbulence is essentially dissipative.*

Continuum *Turbulence is a continuum phenomenon, governed by the equations of fluid mechanics. Even the smallest scales occurring in a turbulent flow are ordinarily far larger than any molecular length scale. We return to this point in Section 1.5.*

Turbulent flows are flows *Turbulence is not a feature of fluids but of fluid flows. Most of the dynamics of turbulence is the same in all fluids, whether they are liquids or gases, if the Reynolds number of the turbulence is large enough; the major characteristics of turbu-*

lent flows are not controlled by the molecular properties of the fluid in which the turbulence occurs. Since the equations of motion are nonlinear, each individual flow pattern has certain unique characteristics that are associated with its initial and boundary conditions. No general solution to the Navier-Stokes equations is known; consequently, no general solutions to problems in turbulent flow are available. Since every flow is different, it follows that every turbulent flow is different, even though all turbulent flows have many characteristics in common. Students of turbulence, of course, disregard the uniqueness of any particular turbulent flow and concentrate on the discovery and formulation of laws that describe entire classes or families of turbulent flows.

The characteristics of turbulence depend on its environment. Because of this, turbulence theory does not attempt to deal with all kinds and types of flows in a general way. Instead, theoreticians concentrate on families of flows with fairly simple boundary conditions, like boundary layers, jets, and wakes."